Effects of Carbon Nanotube Type and Surface Functionalization on the Carbon Nanotube-Unsaturated Polyester Resin Composite Properties

by

Joyanta Goswami

A dissertation submitted to the Graduate Faculty of
Auburn University
in partial fulfillment of the
requirements for the Degree of
Doctor of Philosophy

Auburn, Alabama
December 10, 2016

Keywords: carbon nanotubes, rheology, microstructure, resin, curing

Approved by

Virginia A Davis, Chair, Professor of Chemical Engineering
Allan E David, Assistant Professor of Chemical Engineering
Xinyu Zhang, Associate Professor of Chemical Engineering
Hareesh Tippur, Professor of Mechanical Engineering

Abstract

The goal of this research was to understand the dispersion of carbon nanotubes (CNT) in unsaturated polyester resin (UPR), the relative strength of nanotube-resin interactions, and curing into nanocomposites. These are three of the most critical parameters for controlling nanocomposite properties. UPR was chosen for the matrix because even though it is one of the most widely used thermoset resins there has been relatively little research on CNT/UPR composites. The first aim of this research was to establish a framework for evaluating the effects of carbon nanotube purity and chirality on dispersion in resin matrices. A protocol for comparing percolation thresholds, fractal structure, and differences in the relative strength of nanotube-nanotube and nanotube-resin interactions using rheological characterization was established. The second aim of the research was to understand the effects of CNT type and surface chemistry on curing kinetics using a combination of rheology and differential scanning calorimetry (DSC).

In the first part of the research, the effects of SWNT chirality distribution and purity on dispersion microstructure and nanotube-resin interactions were investigated using four of Southwest Nanotechnologies' SWNT products: a low and high purity semiconducting grade (SG65 and SG65i) and a low and high purity metallic grade (CG200 and CG300). Analysis of the dispersions' viscoelastic properties revealed differences in dispersion microstructure and the relative strength of SWNT-resin interactions. While all four products had a similar percolation threshold, the concentration of non-SWNT carbon impurities had a greater effect than chirality on viscoelastic properties and the relative strength of resin−SWNT interactions. In the second part of the research, viscoelastic properties and curing kinetics near the onset of percolation were investigated for MWNT two pristine SWNT types, and two types of functionalized SWNT. The viscoelastic behavior showed differences in nanotube cluster morphology, nanotube-nanotube and nanotube-polymer interfacial interactions. The viscoelastic properties also showed that rheological percolation by nanotube clusters with a better polymer interface will have a higher elastic behavior. In contrast, nanotube clusters that are more aggregated and have less polymer interface will have a transition to solid-like behavior at shorter time scales. Among the CNT/UPR dispersions, the lower cost, lower purity Tuball SWNT displayed a better dispersion state, greatest enhancement of elastic and viscous moduli, higher gelation modulus and higher curing kinetic rate constant. The results of this research provide new insights into dispersion of CNT into UPR. In addition, they established a robust methodology for evaluating new nanomaterial-resin composite systems.

Acknowledgements

I would first like to express my gratitude to my advisor, Dr. Virginia A. Davis, for giving me the opportunity to be part of her research group and for her constant guidance throughout the research. I would like to thank my committee members: Dr. Allan E.David, Dr. Xinyu Zhang and Dr. Hareesh Tippur for their valuable suggestions and comments on my dissertation. Special gratitude goes to Dr. Hareesh Tippur for his guidance on mechanical test sample preparation. I am also grateful to Dr. Asha-Dee Celestine to be my university reader and taking her valuable time to go through my dissertation document.

I would like to thank Dr. Ramsis Farag for his assistance and suggestions on tensile testing and Dr. Edward Davis on valuable discussions on design of experiments and assistance with dynamical mechanical analysis. I am grateful to the department chair, Dr. Mario Eden, for his valuable support and department staffs Ms. Georgetta Dennis, Ms. Karen Cochran, Ms. Elaine Manning and Ms. Jennifer Harris for their help with academic and financial matters. The chemical engineering staff member who has been an integrated part of my research is Mr. Brian Schwieker and I am grateful to him for making different mold designs and assistance with fiber spinning instrumentation. I am also thankful to the funding sources NSF EPSCoR 1158862 and GAANN fellowship, and Dr. Robert Chambers for his assistance with GAANN fellowship.

Finally, I am grateful to my friends in Auburn for the wonderful times outside work. My parents and family back home in Bangladesh have been a great support during PhD.

The last two years had been the most difficult for me in terms of research and I am grateful to my wife, Sharna, for encouraging me to hang on, and some counselling from a special person in Montreal.

Table of Contents

List of Tables

List of Figures

List of Abbreviations and Symbols

Cobalt naphthenate	CoNAP
Dimethylformamide	DMF
Methyl ethyl ketone peroxide	MEKP
Multi-walled carbon nanotube	MWNT
Polystyrene	PS
Polystyrene-co-acrylonitrile	SAN
Single-walled carbon nanotube	SWNT
Unsaturated polyester resin	UPR

Angular frequency	ω
Complex modulus	G^*
Complex viscosity	η^*
Critical strain	γ_c
Crossover frequency	ω_c
Crossover modulus	G_c
Damping factor	$tan\delta$
Elastic modulus at the end curing	G'_{inf}
Elastic modulus at the start of curing	G'_{co}
Gelation conversion	β_{gel}
Gelation storage modulus	G'_{gel}
Gelation time	t_{gel}
Isothermal heat cumulative	Q_{iso}
Percolation concentration	ϕ_c
Plateau storage modulus	G'_o
Reduced viscosity	η_{red}
Shear stress	σ
Specific viscosity	η_{sp}
Storage modulus	G'
Viscosity	η
Viscous modulus	G''
Volume fraction	ϕ

CHAPTER 1 INTRODUCTION

The goal of this research was to understand three of the most important parameters for enhancing mechanical properties in carbon nanotube (CNT) resin composites: 1) dispersion microstructure, 2) the relative strength of nanotube-resin interactions, and 3) curing into nanocomposites. Specifically, this research focused on single-walled carbon nanotube (SWNT) - unsaturated polyester resin (UPR) composites, but the framework for using rheology to understand these parameters is applicable to other dispersions of cylindrical nanomaterials. SWNT were chosen for their outstanding mechanical and thermal properties. UPR chosen both because it has the largest market share of any thermoset resin and the fact that there have been relatively few studies of CNT/UPR composites.[1-4] Research on thermoset carbon nanotube composites has been dominated by epoxy-CNT composites due to current applications of epoxy in aerospace industry and better properties of epoxy than UPR. However, although UPR has relatively low thermal stability it has good mechanical strength, electrical resistance, chemical and fire resistance. The world market revenue for UPR was $6 billion in 2012 and it is expected to be $12 billion by 2020 with North America being the second largest consumer of UPR.[5,6] UPR is widely used in the building, construction, marine, and automobile industry as well as in decorative architectural components, electronic circuit boards and substituting metals in different applications. These applications include glass fiber reinforced composites. The lower price of UPR compared to epoxy, ease of fabrication and progressive UPR formulation research make it of interest for substituents of metallic parts and high performance applications such as aircraft components – composite nacelle components, fan blades, vanes etc. The continued development of new high performance UPR applications will require improved reinforced UPR composites. Nanomaterials such as carbon nanotubes, graphene, and nanocellulose are the next generation reinforcement materials for developing improved polymer composites. In particular, carbon nanotubes are of interest due to their low density, intrinsic mechanical, thermal and electrical properties, and benefits in terms of lightning strike protection and electromagnetic interference shielding.[7-12] There has been extensive research on incorporating carbon nanotubes at low concentrations in polymer matrices to improve mechanical properties. However, in order for carbon nanotubes to improve the properties of a resin matrix, they must be dispersed as individuals and/or small bundles to enable high surface to volume ratio and significant interfacial contact with polymer chains. Carbon nanotube dispersion is complicated by the strong van der Waals forces between their perfect cylindrical sp^2 hybridized carbon structures. For SWNT, this attractive interaction is ($40\ k_bT/nm$)[13] which equates to over $10^4\ k_bT$ for a typical SWNT. SWNT aggregates tend to be microns to millimeters in size and not only fail to enable the formation of a percolated reinforcing network but actually act as defects which can significantly deteriorate resin mechanical properties. There has been considerable research on processing and chemical functionalization methodologies for improving CNT dispersion in a variety of thermoset and thermoplastic polymer matrices.[3,14-18] However, there have been few studies of SWNT/UPR composites and no direct comparisons between commercial SWNT grades with different purities and chirality distribution. In addition, comparison of various approaches has been hindered by the lack of a framework for comparing dispersion state and relative nanomaterial-nanomaterial and nanomaterial-resin interactions.

To develop improved carbon nanotube composites, a strong understanding of colloidal dispersion structure-property relations is required to understand how to enhance final mechanical properties. In previous work, Urena-Benavides et al[19] examined the fractal microstructure of MWNT and polystyrene functionalized MWNT (PS-MWNT) in UPR using rheological methods. Prior to that, Kayatin and Davis[20] investigated SWNT-UPR dispersions. This research builds on the UPR dispersion methodology and properties investigated by Kayatin and Davis[20] and microstructural characterization performed by Urena-Benavides et al[19]. The current research focuses on comparisons between newly commercialized SWNT products with controlled chirality distributions and purity. The concept behind controlled purity and chirality has been largely driven by the desire for controlled electrical and optical properties. However, to the author's knowledge, the significance of chirality distribution and impurities on the dispersion state in polymer matrices had not previously been addressed. In order to deconvolute chirality distribution and purity effects, four SWNT products from Southwest Nanotechnologies Inc. were compared using rheological and morphological characterization. The four products were CG200, CG300, SG65 and SG65i two products with similar purity but different chiral content and their respective lower purity grades. The results of this research showed that the level of impurities had a more significant effect on dispersion and viscoelastic properties than the chirality distribution. The viscoelastic properties of nanotube dispersions originate from the dispersed microstructure of nanotubes and relative nanotube-nanotube and nanotube-polymer interactions. As a result, rigorous rheological characterization was able to elucidate not only changes viscoelasticity as a function of concentration but also, the onset of rheological percolation, the nature of the fractal microstructure, and the relative strengths nanotube-nanotube and nanotube-resin attraction.

The onset of rheological percolation, the formation of network of nanotubes across the bulk matrix, is important parameter for understanding colloidal and nanomaterial dispersions and the potential for changes in the properties of the final solidified composites. Percolation is associated with drastic changes in viscoelastic properties, as well as increased thermal stability, and mechanical properties in the final composite. In addition, electrical percolation which is critical to enhancing conductivity typically occurs at a similar concentration to rheological percolation. Further increases in concentration above percolation result in both increased composite and the potential for increased aggregation due to decreased distances between nanomaterials. The critical concentration at which percolation occurs is a commonly reported parameter for CNT dispersions, however, differences in viscoelastic properties near the onset of percolation at similar CNT concentrations for different CNT types and surface modifications have been rarely reported in the literature. Understanding the detailed microstructure responsible for network formation is important for understanding nanotube-nanotube and nanotube-polymer interactions as well as viscoelastic and relaxation dynamics. In addition to the comparisons between chirality controlled SWNT products, this research compared the viscoelastic properties of a MWNT product, two different SWNT types (CG200 and Tuball) and two types of SWNT surface modification (covalent attachment of polystyrene (PS) and non-covalent adsorption of polystyrene-co-acryloinitrile (SAN)) near the onset of rheological percolation. This portion of the research elucidated the effects of CNT type on differences in viscoelastic behavior and relaxation dynamics. In addition, the CNT-UPR curing kinetics were investigated using both rheology and differential scanning calorimetry (DSC) for the first time. The results indicated that Tuball SWNT had a better dispersion state, greater enhancement of dispersion elasticity and faster curing rate compared to the other CNT dispersions. Since the Tuball SWNT are a lower cost, lower purity product these results show that the expensive high purity products may not always be the best material choice.

The results of this investigation have established a framework for comparing and optimizing CNT/UPR dispersions and understanding the potential for mechanical property enhancement. This framework can be readily applied to new carbon nanotube grades, different polymers and other cylindrical nanomaterial dispersions. The organization of this dissertation is as follows. Chapter 2 provides a review of background information relevant to this research. Chapter 3 describes the experimental methods used. Chapter 4 provides results and discussion of the comparison of the four commercial SWNT grades and Chapter 5 provides a discussion of the effects of CNT type and functionalization on both viscoelasticity near the percolation threshold and curing kinetics. Chapter 6 summarizes the conclusions about the research.

CHAPTER 2 BACKGROUND

Iijima's synthesis of multiwall carbon nanotube (MWNT) in 1991[21] and the synthesis of single-walled carbon nanotube (SWNT) by Iijima and Bethune groups after two years[22,23] were the beginning of significant research into the properties and potential applications of carbon nanotubes. Carbon nanotubes (CNT) are a class of materials that can have a range of properties depending on the specific chemistry. In general, they have outstanding specific strength, high thermal conductivity, electromagnetic shielding capabilities, and electrical properties that range from semi-conducting to ballistic conductors depending on their exact form. In 2006, it was discovered that although carbon nanotubes were thought to be a new material they existed in seventeenth century Damascus swords and were most likely the reason for these legendary swords' supreme sharpness and strength.[24] Initial CNT research focused on exploring properties of carbon nanotubes, developing process of synthesis of the nanotubes and engineering them for broad range of applications. Modern carbon nanotube research has focused on their use in high strength polymer nanocomposites, actuators, field emission devices, actuators for robotics, biological molecule sensors, drug delivery agents, cancer treatment, miniaturized transistors, and high performance electrodes for rechargeable lithium batteries and solar cells.[25-31] Improvements in better controlled, large scale, carbon nanotube production schemes have accelerated both fundamental and applications research as well as the development of commercial products. Current commercial applications include composite bicycle frames used in the Tour de France, antifouling CNT paint for boat hulls, printed CNT transistors, and an electrostatic discharge shield on Juno spacecraft.[32] Moreover, with increased in mass scale production of carbon nanotubes and ongoing improvements product specificity and purity, potential applications are becoming more probable for commercialization.[33]

In parallel with advancements in carbon nanotube research, thermoplastic and thermoset polymer composites technology has continued to mature with composites finding new applications in airplanes, automotive, and many other applications. The sp^2 carbon-carbon bond are the strongest in nature and the one dimensional structure and low density of carbon nanotubes make them promising for producing high performance polymer composites. In addition to carbon nanotubes' outstanding mechanical properties, their optical, electrical, and thermal properties make them useful for conductive polymers, static charge dissipation, electromagnetic shielding and photo-active polymers. However, all these applications requiring overcoming the challenges of dispersing carbon nanotubes as individuals or small bundles and achieving a thermodynamically favorable interface with the polymer matrix.[34-36]

Uniform dispersion of carbon nanotubes and other nanomaterials results in a large interfacial volume between nanomaterial and polymer. This interphase region has different properties than the bulk matrix as a result of chain stabilization in the vicinity of the nanomaterial. In an ideal nanocomposite, a percolated network forms such that all of the matrix is in this interphase region. Rheology is a powerful tool for understanding nanocomposite microstructure, shear response, the relative strength of nanomaterial-nanomaterial and nanomaterial-polymer interaction, and the potential for mechanical reinforcement through network formation.

2.1 Single-Walled Carbon Nanotube Morphology

SWNT are essentially a single graphene sheet (single layer of graphite) rolled up to form a hollow cylindrical tube. If multiple concentric layers are present carbon nanotubes (CNT) are denoted as double-walled (DWNT), few-walled (FWNT), or multi-walled (MWNT) depending on the number of layers as shown in Figure 2.1. The direction of rolling controlled the orientation of the hexagonal rings, known as chirality, and results in different properties. As produced, the ends of all SWNT are fullerene hemispheres which contain six pentagons and additional hexagons needed to match the SWNT diameter. However, these endcaps are more strained than the tube sidewalls and are typically removed as a result of purification or functionalization schemes. The structure of carbon nanotubes can be primarily divided into two classes based on symmetry: achiral (symmorphic) and chiral (asymmorphic). Achiral nanotubes are those structures which have superposable mirror images while chiral nanotube structure possess a spiral symmetry and mirror images cannot be superimposed. The achiral carbon nanotubes can be further divided into two groups: zigzag and armchair.[37] The general shape of these nanotubes are shown in Figure 2.2. As shown in Figure 2.3, the directional unit vectors for the graphene sheet are $\mathbf{a_1}$ and $\mathbf{a_2}$. The wrapping of the graphene sheet takes place along the vector the **C**. The extent of vector **C** is represented by $\boldsymbol{C} = n\boldsymbol{a}_1 + m\boldsymbol{a}_2$, where n and m represent the scalar magnitudes in direction $\mathbf{a_1}$ and $\mathbf{a_2}$ respectively. The enclosed cylinder is produced when origin (0, 0) meets the end of arrow of vector $\boldsymbol{C}$, determined by indices n and m, which in this case is (11,7). The bold dotted lines lying perpendicular to vector **C** represent the tube axis direction labeled as **T**. The rolling of the achiral structures, zigzag and armchair, are shown as light dotted lines. The bold arrow line **H,** perpendicular to armchair direction, represent neighboring rows of hexagons. All other chiral structures are formed by wrapping of vector **C** at angles θ from zigzag direction or angles ϕ from armchair direction, where $\phi = 30^o - \theta$. The angle θ is known as the chiral angle and it spans from 0^o (zigzag) to 30^o (armchair).[38] The diameter of the SWNT, d_t, and chiral angle, θ, can be calculated from the equations[37]:

$$d_t = a\sqrt{n^2 + m^2 + nm}/\pi \text{ , where a = 0.249 nm} \tag{2.1}$$

$$\cos\theta = \frac{2n+m}{2\sqrt{n^2+m^2+nm}} \tag{2.2}$$

SWNTs can be further categorized based on their electronic states. For n = m or (n-m)/3 = integer, the nanotubes are classified as metallic, else for (n – m)/3 = non-integer the tubes are denoted as semiconductors.[38] In Figure 2.4, different semiconducting and metallic nanotubes are shown with their rolling direction on a graphene sheet.

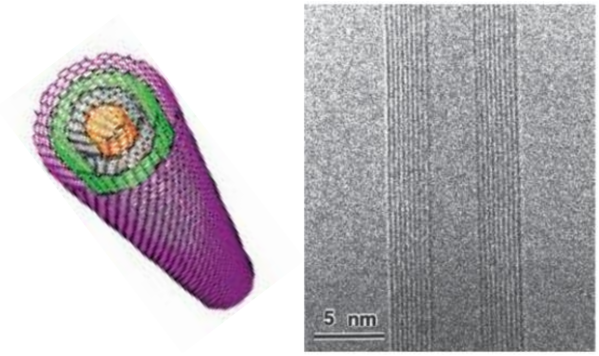

Figure 2.1 Images of carbon nanotube with multiple walls[35,39]

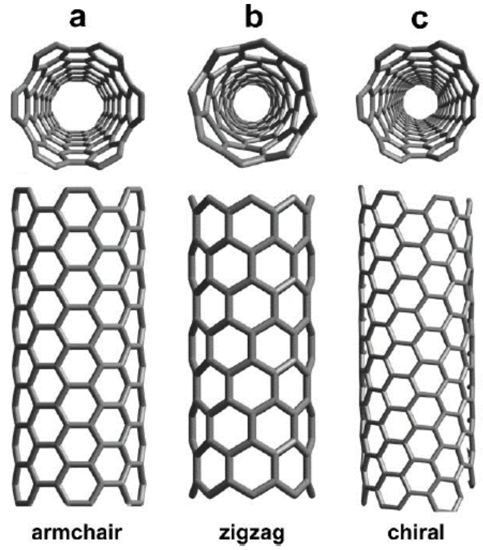

Figure 2.2 Schematic illustrations of different chiralities of SWNT. (a) armchair, (b) zigzag and (c) chiral adapted from Terrones M. Annual Review of Materials Research 2003.[40]

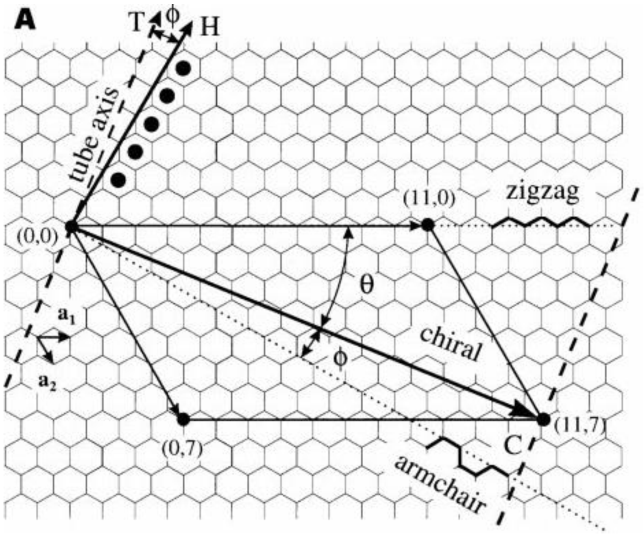

Figure 2.3 Vector representations for construction of carbon nanotube from a graphene layer[38]

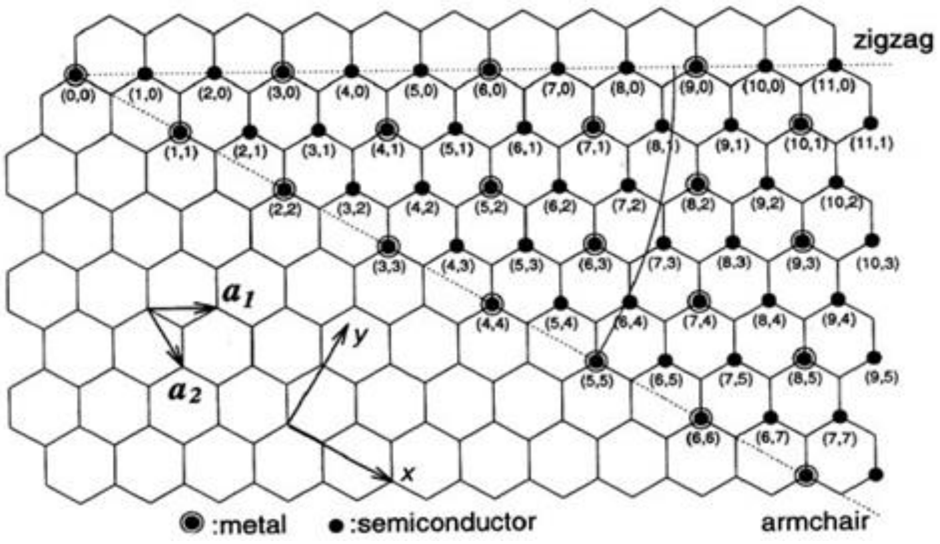

Figure 2.4 Graphene sheet showing (n,m) integers[40]

The reason for the chirality dependence of SWNT's electronic character can be more understood from its parent structure, graphene. The hexagonal first Brillouin zone (space enclosed in a single hexagon) in graphene have multiple valence and conduction energy levels (band degeneracy) about the six corners of hexagons, K-points (Figure 1.5). The Fermi energy passes through these K points. Equienergy contours are observed near the K points and near the center marked Γ (Figure 1.6). Away from point K, in the direction K-Γ and K-M the electronic energy counters distort and it is known as trigonal warping effect. This "trigonal warping effect" creates quantum confinements (density of states) within the valence and conduction bands. The highest or extremal points of the density of states are known as van Hoves singularities. The quantum confinement regions are positioned perpendicular to the tube axis (in circumferential direction) and run parallel to the axis. The separation between the confinements are given by $2/d_t$, where d_t is the tube diameter. So, electronic density of states is chirality dependent. A SWNT is metallic when a density of state line passes through the K point or Fermi energy, else it is semiconducting. Thus by knowing the *n,m* indices, the SWNT structure, diameter and electronic properties can be determined.[41-43]

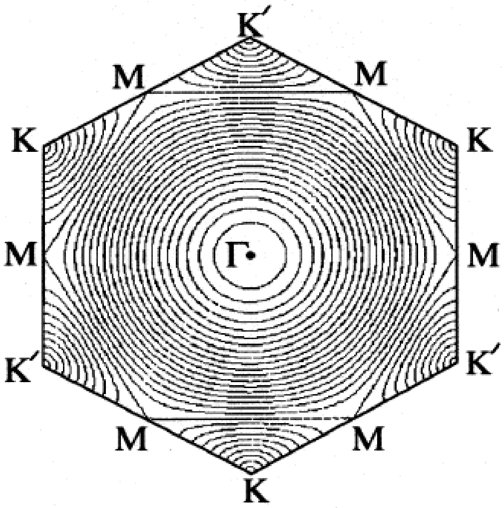

Figure 2.5 Hexagonal first Brillouin zone in graphene showing energy counters[43]

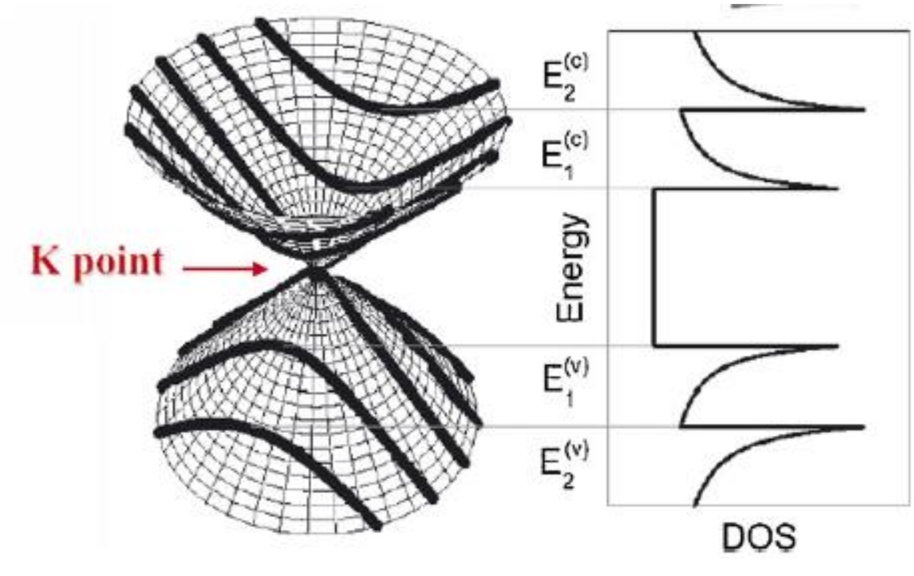

Figure 2.6 K point at a corner of Brillouin zone and dark lines representing quantum energy confinements (density of states) for SWNT [42]

2.2 Mechanical, Electrical and Thermal Properties of Carbon Nanotubes

As previously mentioned, the superior properties of CNT have been a significant part of driving force for research and development. The strength of carbon fiber has been known to increase with graphitization along the axis and carbon nanotubes with seamless defect-free tubular graphitic structure show high mechanical strength.[44,45] The mechanical properties of carbon nanotubes have been investigated both experimentally and through simulation. Experimental measurements have included measuring thermal vibrations, mechanical pinning, and tensile pulling by an AFM tip.[9,44,46,47] Reported measured Young's modulus values ranged from 1.8 to 0.81 TPa for MWNTs[9,46] and 1.25 TPa for SWNTs[44], which were similar to theoretical predictions of ~1.2 TPa for MWNTs[48] and ~1.05 TPa for SWNT[49]. MWNT tensile strengths were found to be 11-60 GPa experimentally[47] and ~500GPa theoretically[48], while for SWNT reported values were~22 GPa experimentally[45] and ~450 GPa theoretically[48]. The maximum electrical conductivity of SWNT was determined to be 10 A/cm^2 [50]. The predicted thermal conductivity by molecular simulation for (10, 10) SWNT was ~ 6600 W/mK,[7] whereas experimentally calculated thermal conductivities of aligned SWNT ropes were ~200 W/mK[51].

2.3 Synthesis of Carbon Nanotubes

Progressing SWNT from a laboratory curiosity to commercial products requires the large scale production of high purity nanotubes with controlled length and chirality distributions. Several routes for carbon nanotube production have been investigated and commercialized. The most prominent methods can be categorized as electric-arc discharge, laser ablation, chemical vapor deposition (CVD) and high pressure carbon monoxide synthesis. Other methods that have been researched are plasma enhanced CVD and flame synthesis. In general, production of carbon nanotubes requires a source of carbon, catalyst, substrate and a source of energy.

Electric-Arc Discharge

Electric-Arc discharge was the very first method used to produce carbon nanotubes (multiwall and single-walled) by Ijima and Bethune et al.[21-23] In this method two graphite electrodes are set as anode and cathode in an inert gas environment, usually helium or argon. High current (50-120 amps) is passed under low-voltage (12-25V) to the electrodes and the two electrodes are initially contacted to raise temperature and start vaporization of the anode. The plasma created in the inter-electrode region contains vapors of catalyst metals and carbon species. The carbon species are deposited on the water cooled cathode.[52-54] Growing SWNTs requires incorporation of metal catalysts in the anode as was shown in works of Iijima and Ichihashi and Bethune et al by use of iron-graphite mixture (methan-argon inert gas mixture) and cobalt-graphite mixture (helium-argon inert gas mixture) in the anode.[22,23] Effective operation requires maintaining strength of plasma through constant voltage, current and gap between the electrodes along with pressure (100 – 1000 torr) and cooling of cathode.[52,55] It has also been shown that tailoring gas composition influenced diameter of the carbon nanotubes produced.[52] In addition, the catalyst type affects the SWNT yield. For example, using yttrium-nickel catalyst mixture at conditions 660 mbar, 100A, and 30V was found to yield 70-90% SWNT.[56]

Laser Ablation

The laser ablation technique can be best described by the work of Gou and co-workers. In this method, a Nd:Yag laser is focused on a graphite or graphite/metal catalyst target axially orientated in a high temperature (~1200^{o}C) furnace. Argon flow is maintained in the furnace to drive vaporized carbon particles toward a water-cooled copper collecting rod located in the downstream of the furnace. Deposition of carbon nanotube and other carbonaceous material results on the copper rod. Gou et al. found a yield of SWNT was obtained for bimetal catalysts (Co-Ni and Co-Pt) and at temperature of 1200^{o}C.[57] A year later, Thess et al. published the use of a graphite/Co-Ni target at 1200^{o}C to obtain a yield of 70%-90% of SWNT with predominantly (10,10) metallic SWNT; the high yield was attributed to using from use two different laser pulses.[58]

Chemical Vapor Deposition

Growing carbon materials from a gaseous hydrocarbon source by deposition on a substrate is a well-developed and widely used technique. Chemical vapor deposition (CVD) has higher yields and product quality than many of the other CNT synthesis methods. In short, the method involves flowing a hydrocarbon gas through a hot tubular furnace (500^{o}C – 1200^{o}C) over a substrate impregnated with fine metal catalytic particles (Fe, Ni, Co or alloy of the metals).[53,54] Endo et al. first reported MWNTs growth by CVD by thermal decomposition of benzene. Carbon monoxide was reported as source of SWNT growth by nucleation on molybdenum catalyst by CVD method.[59] Large arrays, or forests, of vertically erected aligned carbon nanotubes from a mesoporous iron/silica and nickel/glass substrates have been produced by CVD.[60,61]

High pressure carbon monoxide synthesis (HiPco) is a variation of CVD process, was the first high production rate process for producing SWNT. In this method, iron pentacarbonyl ($FeCO_5$) catalyst and CO are fed in a furnace reactor at pressures 1 – 10 atm and temperatures 800 to 1200^{o}C.[62] Iron catalysts are formed in situ and SWNTs are produced by disproportionation of carbon monoxide and are collected as deposits on the quartz reactor wall. Lowest diameter of SWNTs obtained by the process was 0.7 nm.[62] By 2001, optimization of the HiPco process with respect to temperature, pressure and catalyst concentration was shown to produce 97 mol% SWNT and 450 mg/h.[63] Subsequent optimization further improved production rates and control over SWNT length.

Another version of CVD is the plasma-enhanced chemical vapor deposition (PECVD). CVD reactor is modified with a rectangular waveguide, powered by DC source or microwave, coupled with furnace. With the plasma generator turned on, gas (hydrocarbon as carbon source) is flown from the plasma producing end and carbon nanotubes are deposited in the downstream end on substrate (Si or SiO_2) etched with metal catalyst (e.g cobalt). Bower and co-workers used acetylene as carbon source and Si substrate deposited with cobalt catalyst. They demonstrated aligned uniformly spaced perpendicular growth of carbon nanotubes on cobalt at different angular arrangement of substrate and they proved that straightness in perpendicular growth was initiated by the plasma effect not van der Waals force.[64] The PECVD technique provides option for CNT growth on low temperature substrates like glass as it can be operated at lower temperature.[53,54,64]

Other Techniques

Flame synthesis method shown by Vander Wal et al, used a mixture of acetylene and nitrogen with additive gases hydrogen, air or methane entrained with metallocene (ferrocene or cobaltacene). The mixture was ignited to flame and deposits of carbon nanotubes were produced on cold surface facing the flame.[65]

Currently, one the most industrially significant SWNT production processes is the CoMoCAT process developed by Resasco et al. The process employs a fluidized bed of Co-Mo catalyst to catalyze disproportionation of carbon monoxide gas to produce SWNT.[66] This process enables better chirality control than previous processes and was commercialized by Southwest Nanotechnologies (now CHASM). in producing purified SWNTs with higher selectivity and narrow range of chiralities. While ongoing improvements have resulted in faster production rates, more tightly controlled chirality distributions, and lower catalyst residues, commercial grades still contain a significant fraction of non-SWNT carbon which is typically in the form of MWNT or vapor grown carbon fiber (VGCF).

2.4 Dispersion and Functionalization of Carbon Nanotubes

With the exception of vertically aligned forests, carbon nanotube synthesis results in bundles or aggregates containing nanotubes of different lengths, diameters and chiralities. In order for carbon nanotubes' intrinsic individual properties to be manifested in bulk materials, they must be disaggregated and uniformly dispersed uniformly in a fluid, remain as individuals or small bundles, and bear functional molecules desired for the particular application. Moreover, monodisperse SWNTs (with respect to chirality, diameter, length and electronic character) are considered to be the ideal scenario for nanotubes to achieve superior performance in all applications.[39,67]

Dispersion is a key challenge in SWNT research and applications development. SWNTs' high aspect ratio, strong intertube van der Waals attraction (0.5eV/nm), and high stiffness and make them exist in entangled bundles which are extremely difficulty to disentangle into individual tubes.[68,69] The difficult in dispersing carbon nanotubes (SWNTs and MWNTs) has typically been tackled by mechanical methods, dispersing agents and functionalization schemes. Superacids, particularly chlorosulfonic acid are extremely effective at individualizing SWNT through protonation,[70,71] but the use of superacids can be incompatible with dispersion in polymers and some processing equipment.

The mechanical methods use brute force in debundling the carbon nanotubes and disperse them homogenously. The commonly used mechanical methods are ultrasonication, ball milling, high speed stirring, extrusion and calendaring. Ultrasonication uses implosion of cavitation bubbles to break aggregates of nanotubes while the other methods predominantly apply high shear forces to debundle and distribute nanotubes throughout the fluid phase. Ball milling debundles by collision mechanism and is a dry mixing technique prior any fluid processing e.g. melt extrusion.[72,73] Dispersing agents and functionalization schemes improve stability and dispersibility in fluid along with providing functionality for application and improving interaction with medium of dispersion e.g. polymer matrix.

Dispersing agents and functionalization are basically techniques to modify carbon nanotube surfaces. Surface modifications can be primarily divided into two classes: non-covalent functionalization and covalent functionalization. Non-covalent approaches include surfactant encapsulation, biomacromolecules based/aromatic molecule based adsorption, and polymer wrapping of SWNT. Covalent approaches fall under sidewall, defect site and open end chemistries.[39,67] In non-covalent approaches, the interaction between the dispersing/functionalizing agent and carbon nanotube is by π-π overlapping of the conjugate system of the nanotubes and the functional groups of the agent. Surfactants such as sodium dodecyl sulfate (SDS) forms micelle around SWNT with its hydrophobic hydrocarbon tail facing hydrophobic sidewall of SWNT. At low concentrations, typically less than 25 mg/L, spectral based characterization has shown that surfactants can keep SWNTs as individuals after their debundling by ultrasonication.[74] Generally, all surfactants stabilize SWNTs in this manner, and comparisons among surfactants to individually stabilize SWNT have shown that sodium dodecyl benzene sulfonate achieves better stabilization than many other surfactants.[75] Adsorption of biomacromolecules (DNA, proteins), aromatic based molecules (pyrene based molecules) and polymers by conjugate systems onto SWNTs have achieved dispersion and stabilization of carbon nanotubes.[76-79] Wrapping has been suggested to be thermodynamically favorable for DNA and polymers such as polyvinyl pyrrolidone, polystyrene sulfonate.[77,78] Among different proteins histamine has been shown to achieve the best dispersion of SWNT followed by lysozyme.[76]

In the case of covalent reactions, the reaction pathways that are involved can be divided into two categories: direct attachment of functional groups onto carbon nanotubes and attachment of functional moieties via carboxylic acid.[80] The reactivity of single-walled carbon nanotubes is driven by π-orbital misalignment in the sidewalls and curvature-induced pyramidalization. These two conditions induce local strain in the carbon-carbon bonds which is relieved on reaction and conversion to sp^3 hybridization. Sidewalls are less reactive than the fullerene caps and their reactivity increases with decreasing tube diameter.[81,82] Typically carbon nanotubes have defects which promote their reaction. Defects include pentagon-heptagon couples (Stone-Wales defects), sp^3 hybridized carbon, vacancies created upon carbon atoms reacting to other groups and open end of SWNTs bearing carboxylic acid groups. For reaction schemes that start with carboxylic acid functionalized SWNT, SWNTs are treated with strong oxidizing agents (HNO_3/H_2SO_4,

H_2O_2/ H_2SO_4, $KMnO_4$/H_2SO_4) to produce SWNT-COOH and subsequently the –COOH sites can be modified to esters, amides, carbonyl chlorides, zwitterions, metal complexes and other functional moieties.[81,83] On the other hand, some examples of addition of direct functional groups are fluorination, alkyl/aryl group addition by Billups reaction and aryl group addition by diazonium method.[84-86]

In addition to the importance of functionalization for dispersing carbon nanotubes, some functionalization schemes can be used to functionalize or separate specific chiralities. Functionalization can also improve interaction in polymer matrices in composites or impart additional properties needed for drug delivery, antibacterial or sensing applications.

2.5 Rheology of Polymer Nanocomposites

The properties of polymer nanocomposite originate from the intrinsic material property nanofiller, how well the nanofiller is dispersed, microstructure of the fillers in dispersion, filler-filler and filler-polymer interactions. These factors are in turn dependent on the choice of nanofillers, aspect ratio, nanofiller-polymer dispersion processing and nanofiller surface chemistry. Probing the nanomaterial-polymer dispersion state is essential to understand how above mentioned factors contribute to understanding dispersion and relating dispersion properties to the final composite properties.

Nanomaterial-polymer dispersions are class of complex fluids which have much in common with colloidal-dispersions. A colloidal dispersion is typically defined as one where the dispersed phase/materials' dimensions are less than one micron in all three dimensions. A nanomaterial has at least one dimension less than 100 nm, so there is overlap between nanotechnology and colloid science. Both nanomaterial and colloidal dispersions are types of soft matter that exhibit viscoelasticity (a combination of solid and liquid like behavior) due to their internal structure. Rheology is a powerful analytical tool for understanding the microstructure and viscoelastic properties of soft matter including colloidal dispersions, emulsions, gels, polymer melts and liquid crystals. The rheological behavior that that is generally investigated incudes constant shear stress or shear rate response, flow behavior under variable shear rate, deformation with increasing oscillatory strain, deformation attributes under variable oscillatory frequency at fixed strain, and recovery after shear.

Historically, characterization of rheological behavior in the linear viscoelastic regime has been one of the most widely used methods to understand polymer nanocomposite viscoelasticity and microstructure. The linear viscoelastic region is defined as the strain threshold of intrinsic structural integrity; it is experimentally determined by measuring the critical strain below which the elastic and viscous moduli of a sample are constant at fixed oscillatory frequency. The viscoelastic nature of polymer-nanocomposites arises from the ability to store and dissipate induced stress. Storage shear modulus (*G'*) is the measure of elastic behavior (stress energy storing ability) while loss shear modulus (*G''*) is the measure of visocous behavior (stress energy dissipation) under oscillatory shear. Mathematically the moduli are defined as $G' = (\tau_o/\gamma_o\ )cos\delta$ and $G" = (\tau_o/\gamma_o\ )sin\delta$, where τ_o is the amplitude of oscillatory shear stress, $\tau^* = \tau_o e^{i(\omega t+\delta)}$, γ_o is the oscillatory amplitude of shear strain, $\gamma^* = \gamma_o e^{i(\omega t)}$, and δ is the phase lag between stress and strain. The combined effect of *G'* and *G''* is represented by complex shear modulus, *G**; *G** can be defined mathematically as $G^* = \tau^*/\gamma^* = (\tau_o/\gamma_o)\, e^{i\delta} = (\tau_o/\gamma_o)(cos\delta + isin\delta) = G' + iG"$. The mechanical damping factor (*tanδ*) which represents the dominance of viscous versus elastic characteristic for viscoelastic system is given by $tan\delta = G"/G'$ ($tan\delta > 1$ represents dominant viscous (liquid like) behavior whereas $tan\delta < 1$ represents dominant elastic (solid like) nature of composite system).[87] Prior to probing properties in the linear viscoelastic region, the linear viscoelastic regime is determined experimentally from the deviation of steady *G'* value under the increasing strain at constant oscillatory frequency.

The viscoelastic properties (*G'*, *G"*, *tanδ*, η*) under oscillatory sweep have been used to discern various features of dispersion state. For example, the degree of dispersion as a function of processing time has been characterized by measuring changes in *tanδ* and *G'* and when these values become constant.[88-90] On application of deformation colloidal structure exhibit temporal disintegration or structural change and more elastic colloidal structure growth after deformation have been observed by the evolution of *G'*.[91-93] The effect of nanofiller incorporation in polymer matrix is conventionally examined by enhancement of moduli, slope changes of *G'*and *G"* and crossover of moduli. A general observation for nanofiller dispersions is enhancement of moduli with filler concentration. With increase in concentration, the interfiller spacing decreases and interfiller interaction increases. At a critical volume fraction ϕ_c, the nanofillers will form a network spanning the bulk of polymer matrix or dispersion media; this concentration is known the rheological percolation threshold. At increasing concentrations approaching percolation, the slopes of *G'* and *G"* initially show less low frequency dependence, this is followed by near frequency independent behavior at low frequency, and eventually frequency independence throughout entire experimental range. For rigid rods, $\phi_c \approx R/L$. Both Rahatekar et al. and Fan and Advani showed that higher aspect ratio carbon nanotubes reached percolation and increased *G'* and *G"* at lower concentrations.[94,95] There are several techniques for identifying ϕ_c and typically the results of multiple methods are compared. These methods include an order of magnitude increase in G', G'' and complex viscosity, near plateau behavior of G' and $\tan\delta$ at low frequency, divergence of η^* versus G^* , significant slope change in Cole-Cole plot (G' vs G''), and deviation of phase angle in van Gurp-Palmen plot (δ vs G^*).[14,19,96-98] For polymeric systems, changes in moduli slope as a function of frequency and the crossover frequency where $G' = G''$ are the result of relaxation dynamics which are intimately associated with polymer molecular weight and microstructure. Short time scale relaxations are associated with Rouse dynamics and segmental orientation while relaxations at long times take place by movement along the length of polymer chain – reptation.[99-102] Similarly, in nanocomposites the relaxation dynamics result from nanofiller microstructure and the nanofiller's influence on polymer. The inclusion of nanofillers has been shown to restrict polymer long range motion at low frequency strain response but ineffective in hindering short range polymer relaxation at high frequency.[14,16] Therefore, the viscoelastic properties at low frequency (long time scales) predominantly provides information about the nanomaterial dispersion while viscoelastic properties at high frequency short times provide information about the polymer including possible molecular weight reduction during processing. The effects of functionalization on viscoelastic properties are complex. Some investigations on functionalization have shown better dispersion and an increase in elasticity while others have argued that functionalization reduces filler clustering and decreases elastic behavior.[16,19,97,103] In summary, the origin of viscoelastic and relaxation behavior in a polymer nanocomposite is a combination of nanofiller-polymer interaction through bridging and confinement, and a purely nanofiller cluster stress bearing mechanism; the latter is more significant for higher filler loadings, greater filler-filler interaction, and at low frequencies.[104]

Several investigation of colloid-polymer systems illustrated scaling behavior of plateau elastic modulus (G'_o) for concentrations above percolation – $G'_o \sim (\phi - \phi_c)^{\nu}$, where ϕ_c is the percolation concentration and ν is the percolation scaling exponent.[14,19,20,105-107]. The value obtained of exponent ν signifies the type of interaction prevailing in the colloid-polymer system and stress bearing attribute of percolated network.[108,109] Higher values are indicative of superior filler-filler interaction and higher reinforcement with elasticity with addition of fillers, while lower values indicate better filler-polymer interaction.[105,107,108] Exponent values, $\nu \sim 2.1$, signifies percolated physical bonds which can rotate but are resistant to stretching, while $\nu \sim 3.75$ indicates bond resistant to both stretching and rotation. For polymer bridged percolated bonds which form a weaker stress bearing network $\nu \sim 1.8$.[110] The scaling relation of G' above percolation directly relates elastic behavior to the network structure and represents a self-similar superstructure particular type of microstructure known as fractals. Khalkhal and Carreau showed how scaling relation of G' and critical strain (γ_c) with concentration, evaluated from consideration of floc size and interfloc and intrafloc elastic constants, can be applied to assess fractal properties.[106]

$$G' \sim \phi^{B/_{d-d_f}} \quad , \quad \gamma_c \sim \phi^{d-B-1/_{d-d_f}} \tag{2.3}$$

where ϕ is concentration, $B = (d-2) + (x+2)(1-\alpha)$, d is Euclidean dimension (d=3), d_f is the fractal dimension defining aggregation mechanism, x is the backbone dimension ($1 < x < d_f$). Fractal dimensions falling in the range 1.7 – 1.8 define fast aggregating colloids (clusters forming collision) while values in the range 2.0 – 2.2 indicate slow aggregating colloids.[100] Shih et al in their study of colloidal gels defined strong-link and weak-link regime for colloid floc or clusters. In strong-link regime interfloc elastic constant or strength is higher than strength within floc, while in the weak-link regime intrafloc strength dominates over interfloc strength. The α value, which ranges between 0 and 1, categorizes dominance of strong link regime (α approaching 1) and weak link regime (α approaching 0) for the fractals.[111] Simulation studies by Potanin investigated rigidity ($m = 1/B$) of fractal aggregates. Fractal aggregates are considered rigid ($m_{rigid} = 1/B \sim 0.23$ to 0.29) when interaction of particles in aggregates are non-central (angular interaction exists between neighbors). For the soft aggregates ($m_{soft} = 1/B \sim 0.40$ to 0.50), the particles forming aggregates interact centrally (interaction depends on the distance between particle centers). Under deformation secondary aggregates originating from soft aggregates do not maintain relative position of particles; secondary rigid aggregates respond to further deformation without change in particle relative positions within aggregates. [112]

2.6 Unsaturated Polyester Resin and Curing Kinetics

Unsaturated polyester resins (UPR) fall into the category of thermoset polymers – polymers synthesized from fluid phase monomer as giant covalently crosslinked macromolecule that has an irreversible final state. Among thermoset polymers (polyurethane, polyimide, epoxy, polyester, amino and phenol formaldehyde resins), UPR dominates the thermoset market with diverse applications in marine, gel coats, electrical, automotive, building and construction industries.

Unsaturated polyester (UP) polymers are prepared by condensation polymerization between difunctional acids or anhydrides and difunctional alcohols or polyols; usually the difunctional acid or anhydride, contain olefinic unsaturation that are retained after condensation and the resulting esters are thus called unsaturated.[113] The general chemical reaction for formation of unsaturated polyester can be represented by scheme:

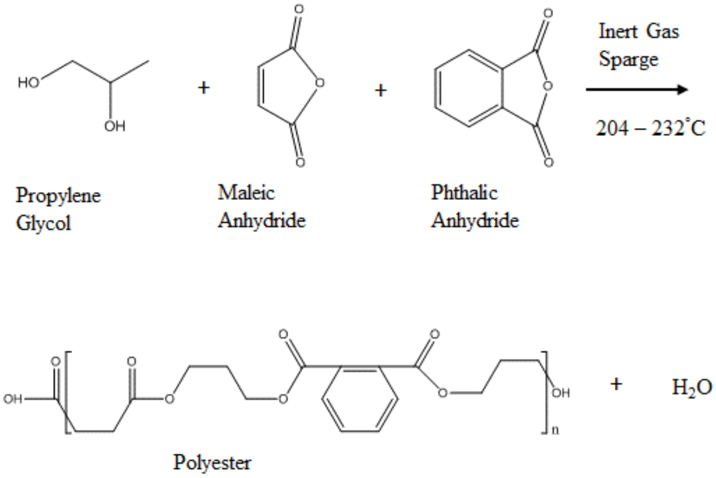

Figure 2.7 Reaction scheme for unsaturated polyester resin. (Reproduced from Zaske, O. C. and Goodman, S., Unsaturated Polyester and Vinyl Ester Resins. *Handbook of Thermoset Plastics*, 1998)[113]

The UP obtained by polycondensation is highly viscous. The average molecular weights of orthophthalic acid derived resins lie between 800 – 1000 g/mol and for the isophthalic the range is 1500 – 2000 g/mol. For future processability and final crosslinked state, the UP is solubilized in styrene and this solution is known as UPR. UP-styrene ratio controls viscosity and influences crosslinking degree in the final cured state. The percentage of styrene in the UPR resin can vary from 30 – 50 weight percent. [114,115]

UPR properties are controlled by the polyester building blocks – size and functionalities of diacids/dianhydrids and polyols. Commonly used acid and alcohol building blocks are maleic anhydride, fumaric acid, orthophthalic anhydride, isophthalic acid, polypropylene glycol, dipropylene glycol and hydrogenated bisphenol-A. Phthalic acid (PA) to maleic acid (MA) molar ratio effects tensile elongation, heat deflection, cured hardness and reactivity. Higher content MA increases reactivity, cured hardness and heat deflection due presence of higher linear unsaturation, whereas PA promotes higher refractive index and decreased reactivity.[113] Similarly presence of cycloalkenes and higher unsaturations in acids/anhydrides lead higher mechanical impact strength and crosslinking density. To obtain higher tensile elongation, flexibility and toughness in UPR, preferred raw materials would be longer aliphatic chain containing polyols such as dipropylene glycol and long aliphatic acids such as adipic, sebacic acid in place of phthalic acid.[113,115] On the other hand, flame resistance is increased by the introduction of halogenated acids or anhydrides, and chemical resistance is increased by the addition of aromatic or cyclicaliphatic alcohols.[113] A summary of different building blocks is given in the Table 2.1. The average molecular weights of orthophthalic acid derived resins lie between 800 – 1000 g/mol and for the isophthalic the range is 1500 – 2000 g/mol. The polyester resins are commercially sold in solutions of styrene monomer.

The curing of UPR resin is a range of free radical polymerization involving predominantly of the styrene vinyl monomer with UP unsaturation sites and styrene-styrene homopolymerization. UP homopolymerization is also relevant at certain curing conditions.[115] In general, an organic peroxide is used as the initiator for the polymerization and a cobalt salt or aromatic amine is used as the accelerator for room temperature curing.[115] This polymerization leads to formation of a chemically crosslinked network which transforms the physical state of resin from liquid to gel and finally to a solidified material. The curing process has been described to proceed by microgel-based mechanism. According to this mechanism, free radical reactions form polymer chains which consecutively produce intramolecular (reaction between unsaturation sites themselves or by styrene within a polymer chain) and intermolecular linkages (between unsaturation sites themselves or by styrene between two polymer chains) leading to formation of domains referred as microgels.[115,117] With curing time the microgel concentration increases and microgels form intermolecular linkages spanning bulk of the material and this state is referred as gel.[115,118] The microgel morphology and phase behavior during curing depends largely on styrene concentration which effects microgel compactness, crosslinking density and relative concentration of polystyrene and polyester phase.[117,119] The reactions on curing lead to a UPR-rich phase (crosslinked phase) and a styrene-rich phase (polystyrene) and results phase separation due immiscibility of the resin phase. Styrene concentration plays a determinant role in microstructure and phase behavior for the networking resin. With increase in styrene concentration, the crosslinking bridge dominantly involves polystyrene (longer molecular segments) which reduces crosslinking density and increases swelling of network. The stiffer polystyrene chains increase glass transition temperature of the UPR. With higher amount polystyrene produced during curing, the UPR miscibility decreases in the curing mixture.[119]

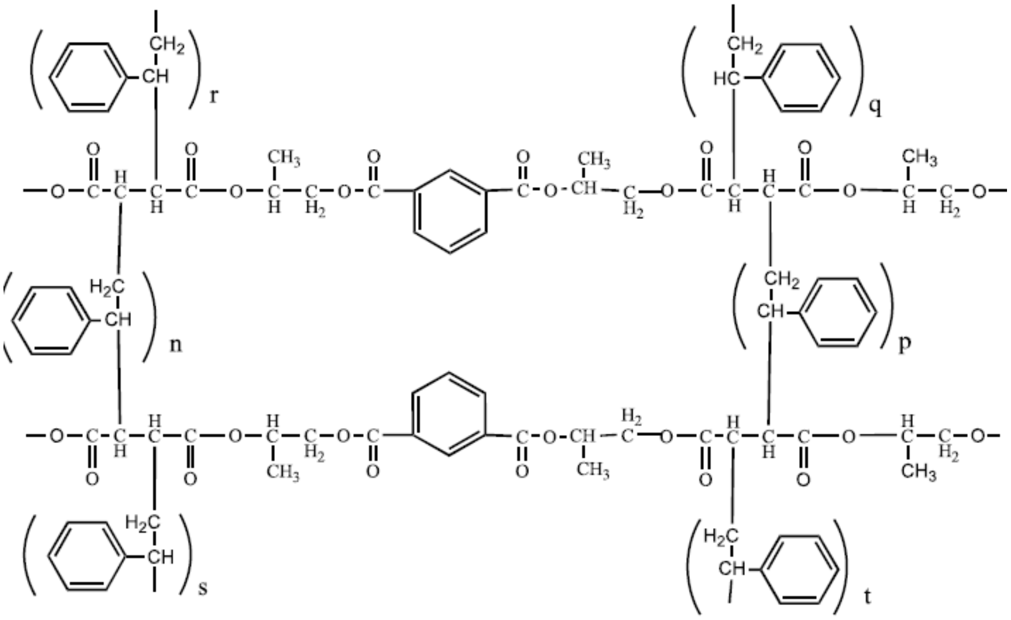

Figure 2.8 Structure of cured UPR showing the cross linking between unsaturated part of polyester chain and vinyl group of styrene. Adapted from Bureau. E et al 2001.[119]

The processing of thermosets requires understanding of physical property changes, flow behavior, degree of conversion, time to cure, effect of fillers and effect of processing conditions such as temperature and pressure during curing. Understanding of curing process is achieved by kinetic studies of curing and is used to optimize thermoset processing. Curing kinetics can be studied by dynamic scanning calorimetry (DSC), Fourier transform infrared spectroscopy (FTIR), dielectric measurements and rheology measurements.

Table 2.1 Effect of different raw materials on properties of polyesters. (Reproduced from Forsdyke K.L. and Starr, T. F., Thermoset Resins, 2002)[116]

Building block	Raw Material	Characteristics
Unsaturated anhydrides and dibasic acids	Maleic anhydride	Low cost, and provides a resin with a moderately high heat deflection temperature (HDT)
	Fumaric acid	Imparts the highest reactivity (molecular crosslinking), a higher HDT, and more rigidity, but is a slower forming polyester
Saturated anhydrides and dibasic acids	Phthalic (orthophthalic) anhydride	Lowest cost, moderately high HDT; provides stiffness, high flexibility and tensile strength
	Isophthalic acid	Provides high tensile and flexural strength, better chemical and weather resistance and high HDT
	Adipic, azelaic and sebacic acid	Imparts flexibility (i.e., toughness, resilience and impact strength). Adipic acid is the lowest in cost of the flexibilising acids
	Chlorendic anhydride	Employed where flame retardance is demanded of the polyester resin
	Terephthalic anhydride	High heat deflection and high strength
	Tetrachlorophthalic anhydride	Confers flame retardancy to the polyester resin
Glycols	Polypropylene glycol	A low cost glycol, provides a resin with good water resistance and flexibility, plus compatibility with styrene
	Dipropylene glycol	Used where flexibility and toughness are required
	Diethylene glycol	Imparts greater toughness, impact strength and flexibility
	Hydrogenated bisphenol-A	Provides a resin with better corrosion resistance, a high HDT, high flexibility and tensile strength
	Tetrabromobisphenol-A	For flame resistance

The most commonly used of these methods is DSC; the change of heat flow during the curing reaction is assumed to be proportional to the degree of conversion:

$$dH/_{dt} = d\alpha/_{dt} \tag{2.4}$$

$$\alpha = {}^{H_t}/_{H_{Tot}} = {}^{1}/_{H_{Tot}} \int_0^t {}^{dH}/_{dt}\, dt \tag{2.5}$$

Here α is the degree of conversion, H_t is the cumulative heat flow for time t and H_{Tot} is the total heat evolution for the curing process assuming complete reaction. The curing process is generally investigated through isothermal runs at different temperatures and dynamic non-isothermal scans at varying scanning rates. The fundamental kinetic equation for curing is defined as ${}^{d\alpha}/_{dt} = kf(\alpha) = Ae^{-Ea/_{RT}}f(\alpha)$, where t is the time, α is the degree of conversion, k is the rate constant defined by as function of absolute temperature, T, by Arrhenius relation, E_a is the activation energy, R is the gas constant and $f(\alpha)$ is the reaction model.

The simplest reaction model is the n-th order model which accounts maximum curing rate without accounting for autocatalytic effects.

$$d\alpha/_{dt} = k(1-\alpha)^n \tag{2.6}$$

More widely used models include autocatalytic model and modified autocatalytic model with initial rate zero (k_1=0) and predicts a maximum curing rate between 10 – 40 % conversion.[120] These models have been used for different thermosets and filler based thermosets.[121-123]

$$d\alpha/_{dt} = (k_1 + k_2)\alpha^m(1-\alpha)^n \tag{2.7}$$

$$d\alpha/_{dt} = k\alpha^m(1-\alpha)^n \tag{2.8}$$

When approaching terminal curing stage the curing reaction becomes diffusion limited under high viscosity and to account for near zero reaction rate at latter stages of curing another modification of autocatalytic model has been adopted which includes a maximum conversion term.[124,125]

$$d\alpha/_{dt} = k\alpha^m(\alpha_{max}-\alpha)^n \tag{2.9}$$

Fitting isothermal models one can obtain rate constants at particular temperature and reaction orders, m and n, where m and n defines reaction order at initiation and propagation stages of curing respectively.[120] Further the rate constants obtained at different temperature can be used calculate activation energy by Arrhenius plot.[120,125] A drawback in isothermal curing is lack of representation of complex reaction processes or the presence of multiple reactions since some reactions are difficult deconvolute at certain temperatures. Moreover, lower temperature isothermal reactions suffer from incomplete reaction and assessment of proper baseline total energy calculations.[126] Nevertheless, isothermal curing studies are widely used to understand curing kinetics. Non-isothermal scans at different temperature ramping have shown the presence of different peaks which become more prominent at different scanning rate.[125] Non-isothermal scans have been shown to be mechanistic models accounting for different possible reactions with weighed individual rate equations.[120,126]

In the case of curing rheology or chemorheology, the development of macromolecular structure effects mobility and changes viscoelastic behavior which can be directly related to the extent of curing process. The notable features observed during the course of curing is the near constant behavior of $tan\delta$ and slow increase in η^*, G' and G'' in the induction phase followed by a sharp drop in $tan\delta$, moderate rise in G'' and sharp rise in η^* and G' due to network formation. In the rest of the curing process, G', G'' and η^* increases with varying slopes before plateauing in the termination stage of curing while $tan\delta$ increases passing through a minimum in the gelation stage. An important parameter of curing kinetics is the time to gelation or gel point. The gel point has been identified by crossover of G' and G'' for dynamic frequency runs and from the intersection of $tan\delta$ curves for different constant frequency scans for curing of stoichiometrically balanced systems.[127,128] Other methods that have been employed for gel point detection include an initial maxima in $tan\delta$, time when $tan\delta$ hits minimum value, intersection of tangents drawn at the maximum rate of increase of G' and plateau G' near the end of curing, and intersection of initial slope and maximum slope of η^*curve.[125,129-131] In this work, the time corresponding to the minimum in $tan\delta$ is taken as the gel time.

2.7 Functionalization of SWNT by Lithiation Chemistry: Billups Reaction

The Billups reaction in Figure 2.9 was first reported by Liang et al to chemically functionalize SWNT and make them dispersible in organic or aqueous solvents.[84] The reaction is a reductive alkylation and arylation route using lithium or sodium in liquid ammonia for debundling and sidewall functionalization of carbon nanotubes; this reaction is one of a few schemes that functionalizes the sidewalls of individual SWNT and not just the outside walls of a SWNT bundle. In this reaction process, ammonia is condensed over dry SWNTs. On addition of lithium, solvated electrons are produced in the liquid ammonia which are rapidly transferred to the SWNT make them negatively charged. The negatively charged nanotubes are simultaneously intercalated by lithium cations solvated in ammonia and debundle by electrostatic repulsion.[84]

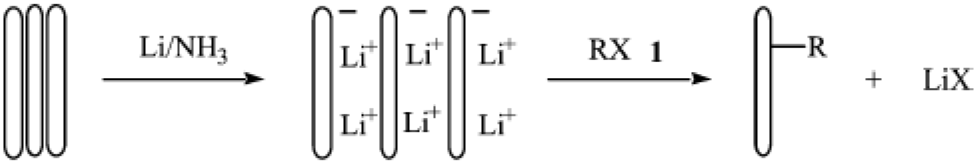

Figure 2.9 Scheme for Billups reaction showing intercalation of positive lithium ion between CNTs followed by addition of hydrocarbon molecule[84]

The addition of alkali metals such as sodium, lithium and potassium in liquid ammonia gives rise to a distinctive blue color which results from the presence of solvated electrons (free electron released from alkali metal) as they have wide absorption in the infra-red region.[132,133] The dissociation of lithium in ammonia was given by Overberger (1953) by the following equation:

$$Li + NH_3 \rightarrow Li^+(NH_3) + e^-(NH_3)$$

The next step involves formation of carboanion complexes by the transfer of solvated electrons onto carbon (SWNT). In the successive step of alkylation and arylation, the carboanion (negatively charged SWNT) reacts with alkyl or aryl radical dissociated from their respective halides. Along with the above equation as the initial step, the reaction mechanism leading to functionalization of SWNT has been shown by Borondics et al.[134]

$$e^-(NH_3)_n + C \rightarrow nNH_3 + C^-$$

$$C^- + RX \rightarrow CR + X^-$$

where RX is alkyl or aryl halide, R being the alkyl or aryl group and X the halogen.

MWNTs have also been functionalized by the Billups procedure with different alklyl and aryl groups by addition of different alkyl and aryl reagents by Stephenson et al.[135] In all cases functionalization is typically characterized by the Raman D/G ratio to investigate the increase in sp^3 carbons, thermal gravimetric analysis to determine the mass of functional groups added and the approximate number of carbons functionalized, and solubility studies.[135]

Functionalization with Styrene

Stabilizing or functionalization agents added to carbon nanotubes covalently or non-covalently have to be compatible and develop good interaction with the solvent or polymer matrix in which carbon nanotube is intended to be incorporated. The type of interaction between the functionalizing agent and solvent or polymer matrix are important toward the final carbon nanotube integrated system. The type of interaction depends on the functional group on the CNT and the solvent or polymer system. For CNT in unsaturated polyester resin the possible interactions are basically hydrogen bonding, non-specific interaction between like groups and chemical bond formation during curing. Figure 2.10 shows the different interaction associated with different functional groups.

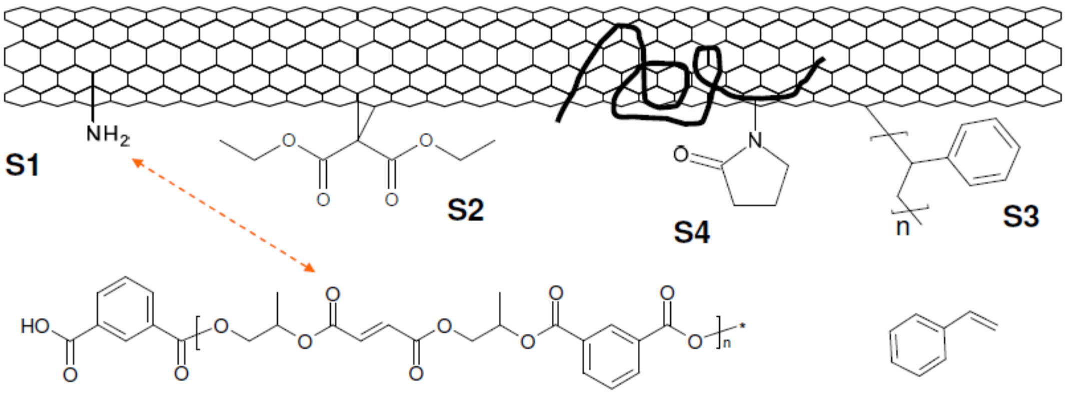

Figure 2.10 Different possible modifications of SWNT surface for compatibilization with UPR (S1) represents hydrogen bonding between covalently bonded amine group and oxygen in carbonyl group of UPR, (S2) represents an ester group covalently attached to CNT having like-like interaction with polyester oligomers, (S3) shows non-specific interaction between polystyrene and monomer styrene in UPR, and (S4) shows non-covalent adsorbed polyvinyl pyrollidone onto CNT having non-specific interaction between cyclic group and polyester oligomer. Reproduced from Kayatin M. J. PhD thesis 2012.[136]

In this work, the Billups reaction was used to add styrene to the SWNT sidewalls. The choice of styrene as a functional group was made on the following premises: (i) stability of styrene in Li/NH_3 (ii) polymerization of the styrene through the vinyl group and lack of unwanted byproducts (iii) polystyrene dissolves in styrene and styrene dissolved UPR so polystyrene functionalized SWNT (SWNT-PS) would be soluble in styrene-UPR. To make the SWNT-PS, lithium and styrene monomer were both used in excess. The styrene was added in multiple additions instead of single addition in order to increase the extent of functionalization.[137,138] The solvated electrons debundling SWNT and creating SWNT surface charge are transferred to some extent to the vinyl bond of styrene monomer. This transfer of electrons reduces SWNT surface charge and increase the chances of rebundling of SWNT. The excess lithium used intercalates between the SWNTs and acts as the supplier of solvated electrons to maintain surface charge on the SWNT and mitigate SWNT bundling. The transfer of solvated electrons to styrene monomer forms radical ion which serves as the initiation step of styrene polymerization as shown in Figure 2.11. The formation of styrene radical ion ($M^{\cdot-}$) is expected considering Birch reduction mechanism and further supported by the investigation of Buick et al on styrene in Na/ liquid NH_3 environment.[139,140] The formation of $M^{\cdot-}$ serves as the initiation step of polymerization to polystyrene. The polymerization of styrene takes place by a radical propagation method well defined as atom transfer radical propagation (ATRP) with single electron transfer (SET) as the initial step.[141,142] Starting with $M^{\cdot-}$, the polymerization can take place by anionic propagation in one direction, unidirectional propagation from the radical site, and radical-radical coupling followed by propagation from the anionic site. The coupling of polystyrene onto SWNT has been referred as a “grafted to” method and the final state of polymerization of styrene that can allow this grafting to take place was concluded to be radical propagation in one direction.[143] The radical grafting was the preferred scheme since other reaction mechanisms such as anionic propagation ($^{-\cdot}MM^{\cdot-}$) can be neglected as the final anionic polymeric radical of PS cannot be terminated onto negatively charged SWNT due to repulsion.[136,143]

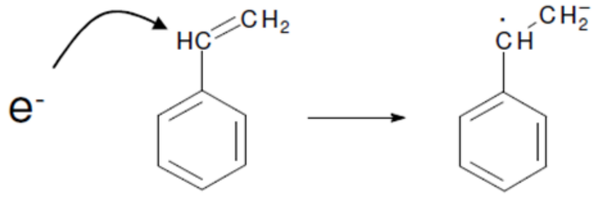

Figure 2.11 Initiation step of polymerization of styrene – formation of monomeric styrene radical anion

CHAPTER 3 EXPERIMENTAL ANALYSIS

This chapter described the experimental methods used in this research including the raw materials, chemical functionalization, and characterization protocols. Procedures that are only relevant to a specific portion of that work are included in the corresponding results chapter.

3.1 Raw Materials

Reichhold Polylite 31830-00 UPR (70.5 wt % isophthalic polyester/29.5 wt % styrene) was purchased from Plasticare, LLC (Englewood, CO) and provided by Reichhold (Durham, NC). This Newtonian resin had a viscosity of 3.1 Pa s at 10 ºC. SWNT products SG65 (Lot # 35), CG200 (Lot # 14), SG65i (Lot #48) and CG300 (Lot # 32) were obtained from SouthWest Nanotechnologies Inc. (Norman, OK) and used as received. CG200 (Lot# MKBP5227V) and MWNT (Lot# MKBD4154) were purchased from Sigma-Aldrich (St. Louis, MO). The other SWNT product Tuball (Lot# 106-09092015) was purchased OCSiAl (Columbus, OH). Styrene for covalent functionalization of CG200 was produced by Alfa Aesar (99.5% stabilized, Lot# 10189080) and Acros Organics (99%, stabilized, Lot# B0531088) and purchased from VWR (Wayne, PA). Polystyrene-co-acrylonitrile (average M_w ~ 185,000, powder, Lot# MKBT0842V) for non-covalent functionalization was purchased from Sigma-Aldrich (St. Louis, MO). Lithium granules (Alfa Aesar, Lot# Y14A066) used for Billups functionalization was purchased from VWR (Wayne, PA). Cobalt naphthenate (Lot# MKBL6851V) was purchased from Sigma-Aldrich (St. Louis, MO).

3.2 SWNT Characterization

The SWNT purity and thermal stability were measured in air using a TA Instruments (New Castle, DE) Q50 TGA. The temperature was ramped from room temperature to 120°C at 10°C/ min and then held for 20 minutes to remove moisture and then ramped at the same rate to 800°C followed by a 45 min hold. The weight loss was analyzed using the published Sigma-Aldrich method to determine the percentage of actual SWNT, non-SWNT carbon and catalyst.[144] A Pacific Nanotechnology, Inc (Santa Clara, CA) Nano-R™ AFM was used to characterize length and diameter distributions for C12 functionalized SWNT.[145,146] Raman spectra were obtained using both 514 nm and 785 nm lasers on a Renishaw inVia Raman microscope (Hoffman Estates, IL) linked with a Leica 50X (0.75 NA) objective. The spectra were an accumulation of 10 runs with exposure time of 10 s for each run. SWNT surface chemistry was characterized by X-ray photoelectron spectroscopy (XPS) using a Kratos Analytical XSAM 800.

3.3 Dispersion Preparation

All calculations were based on densities of 1.14 g/cm^3 for UPR, 1.55 g/cm^3 for CG200 and CG300 (actual SWNT) and 1.59 g/cm^3 for SG65and SG65i (actual SWNT) in a total volume of 28 ml. The dispersions were mixed in accordance with our previously published protocols.[20,147] Dispersions used in the investigation in Chapter 5 had were25 ml in volume. In short, the required amount of SWNT was weighed into a 50 ml round bottomed flask and then the appropriate amount of resin was added. The dispersions were mixed in an Ace Glass (Vineland, NJ) Trubore four-neck flask head with Teflon stirring shaft attached to a flexible shaft. Before starting the shear mixing, the flask was purged by argon and all joints and opening were sealed with Parafilm. Mixing was conducted at approximately 1000 rpm for 3 days while the flask was kept partially submerged in a cold bath to minimize styrene evaporation. Dispersions were stored in sealed vials after removal from the mixer. The mixtures were prepared with the goal achieving equivalent amounts of actual SWNT in the CG200, CG300, SG65 and SG65i dispersions; the sample masses were different due to differences in purity and chirality (density) distribution. All samples were within ± 0.03 vol % of the target concentration. For CG200, the actual concentrations were 0.010, 0.020, 0.050, 0.090, 0.13, 0.17 and 0.22 vol %. For SG65 the actual concentrations were 0.010, 0.020, 0.050, 0.100, 0.14, 0.19 and 0.25 vol %. The dispersions prepared with CG300 the concentrations were 0.050, 0.100, 0.14, 0.17 and 0.20 vol % and with SG65i were 0.05, 0.10, 0.14, 0.17 and 0.21 vol %. For the comparison study of CNT type and CNT surface modification in Chapter 5, the actual nanotube concentrations (not total concentration including impurities) were 0.1 vol %, 0.15 vol % and 0.2 vol % CG200, 0.1 vol %, 0.15 vol % and 0.2 vol % MWNT, 0.2 vol % covalent CG200-polystyrene (CG200PS), 0.2 vol % non-covalent CG200-Polystyrene-co-acrylonitrile (CG200SAN) and 0.2 vol % Tuball.

3.4 Dispersion Characterization

Dispersions were characterized ~ 24 hours after removal from the mixer. Microscopy was performed using a Nikon Eclipse 80i optical microscope (Melville, NY) using LU Plan Fluor 20X / 0.45 NA Nikon objective, NIS Elements software, and a Prior scanning stage to enable image stitching. Rheology was performed using an Antor Paar (GmbH) Physica MCR 301 rheometer (Ashland, VA) at a temperature of 10 ^{o}C. The temperature was controlled by Peltier temperature control device. A cone and plate measuring geometry with diameter 50 mm and cone angle 2.018^0 was used with a gap setting of 0.052 mm between the center of upper and lower plates. In addition to three sample loadings in cone and plate geometry for all concentrations, a 50 mm parallel plate geometry was also used for some SWNT concentrations to ensure the rheology data was independent of fixture related artifacts. For each dispersion sample at least two rheometer loadings were characterized. The first consisted of an amplitude sweep to the onset of nonlinear viscoelasticity γ_c followed by a frequency sweep at $\gamma < \gamma_c$; this sequence was repeated and followed by a steady shear transient tests to determine the time to steady state. The second load repeated the amplitude and frequency sweep sequence, but was followed by a steady shear flow curve from 0.01 to 100 s^{-1}. Based on the transient tests, the sampling time for all samples was logarithmically decreased with shear rate from 1500 s per measurement at 0.01 s^{-1} to 50 s at 100 s^{-1}. Error bars for all measurements were a maximum of 12 % even for measurements made using different test sequences or repeated amplitude sweep testing over 5 hours.

3.5 Curing Kinetics Study

The curing mixtures were prepared by maintaining a mass percent of cobalt naphthenate (CoNAP), methyl ethyl ketone peroxide (MEKP) and UPR at 0.2 %, 1.5 % and 98.3 % respectively. CNT-UPR dispersion was weighed to maintain 98.3% polyester resin in the curing mixture. The curing mixture was made by first adding CoNAP, followed CNT-UPR and MEKP and total amount of curing mixture was 1.9 – 2.1 g. The curing mixture was hand stirred for 2 min and vacuumed for 2 min before loading the mixture for rheology. Curing rheology was performed using an Antor Paar GmbH Physica MCR 301 (Ashland, VA) rheometer with disposable 25 mm parallel plate geometry as the top fixture and 50 mm disposable plate as the bottom fixture. The isothermal curing rheology was performed at a temperature of 25°C and constant frequency and strain of 1Hz and 0.02% respectively for a period of 5 hours.

Differential scanning calorimetry (DSC) based curing kinetics analysis used similar curing mixture preparation method with smaller curing mixture content ~ 1200 – 1400 mg. DSC experiments were conducted using Q100 DSC, TA instruments (Newark, DE). The DSC protocol for isothermal runs included taking the DSC standby temperature to the desired isothermal temperature before loading the sample pan (sample size ~ 10 – 14 mg). The run procedure included isothermal hold for 300 min followed by 10°C/min ramp to 200°C and hold for 10 min.

3.6 Billups Reaction of SWNT with Styrene

A very important requirement for the reaction is anhydrous and air free environment, as presence of moisture or air can cause re-oxidation. To maintain anhydrous environment, weighed amount of carbon nanotubes, 3-neck reaction flask, dry ice condenser, stir bars and glass lids were vacuum dried at 180°C overnight and cooled in the oven before using for the experiment. The apparatus setup consisted of a 3-neck round bottomed flask where the middle neck was used for the cold finger insertion of the condenser flask, one side neck for injection of dry argon and other side neck as outlet vent to oil bubbler or vacuum pump. Before installation of the components to respective ports, a PTFE or glass encased stir bar is placed in the neck flask. The side neck inserts were fitted with Teflon sleeves, except for the middle insert of the condenser, to seal off any air passage. Cold finger insert in the middle neck was wrapped with PTFE tape. After completion of respective port installation, one side neck outlet was connected to vacuum pump and the glassware was flame dried.

Flame drying was repeated for three times under vacuum with intermediate cooling to ensure complete removal of moisture. Then vacuum pump line was replaced by the vent line to mineral oil bubbler and the glassware was purge with argon for 15 minutes. By turning off the argon flow weighed amount of SWNT were inserted from a dry vial using weighing paper funnel through the venting neck by unplugging the bubbler line. Argon flow was resumed at a slower rate to prevent scattering of the carbon nanotube powder and bubbler line reconnected. The argon purging was continued for 45 minutes. Next dry ice and acetone slush was added inside the condenser and argon flow was slowly turned off and simultaneously ammonia flow around the condenser wall was started and a bowl was placed under the 3-necked flask with dry ice/acetone slush to speed up the liquefying process. When condensed ammonia started wetting the carbon nanotubes, the flow rate of ammonia was adjusted to restrict mineral oil from rising through the vent line. The ammonia flow was continued until desired level of liquid ammonia was collected in the flask. When desired volume of ammonia (70 - 100 ml) was collected, the ammonia flow rate was slowly reduced and simultaneously argon flow was started. Argon flow was then increased and ammonia flow was completely stopped. While continuing the argon flow, the purge line to the oil bubbler was closed briefly and the condenser was dismantled from the 3-necked flask and replaced by a loosely fitted glass stopper wrapped with Teflon sleeve. Stoichiometric amount of weighed lithium was added through the center port in presence of argon flow and magnetic stirring of the ammonia/carbon nanotube mixture. After 30 minutes of stirring of lithium/ammonia (allowing saturated reduction of carbon nanotubes), measured volume of styrene monomer was added in six separate additions with an interval of 10 minutes between each addition. During the additions of styrene, the argon flow rate was maintained to float the glass lid on the center port. After the final addition of styrene, the argon flow was continued for 15 minutes. Then the argon flow was turned off, the dry ice/acetone slush bowl underneath the 3-necked flask was removed and bubbler line was kept opened. The mixture was stirred overnight in boiling ammonia until the ammonia completely evaporated. On the following day, all of the ports of 3-necked flask were opened. Ethanol (~ 70 ml) followed by water (~ 70 ml) were slowly added to the level where it submerged the dry residues and the mixture was stirred for 5 – 10 minutes, followed by addition of 10 ml of 10 vol % HCl. The mixture was transferred to a separating funnel and where an equal volume of distilled water and toluene (~ 50 ml each) was added. The funnel content was vigorously shaken to extract the functionalized nanotube in the toluene phase and the bottom layer of aqueous phase was discarded. Water was added and aqueous phase was discarded repeatedly till the pH of the drained liquid was neutral. During shaking the pressure developed in the funnel was released by opening the lid. Then the remaining toluene layer containing the functionalized SWNT was filtered using a 0.2 μm PTFE coated polypropylene membrane filter. The polystyrene functionalized SWNT (CG200PS) was collected on filter paper washed with toluene and ethanol. The CG200PS was scraped off from the filter paper and redispersed in ethanol in a beaker for 5 minutes by bath sonication. The redispersed CG200-PS was poured in the extraction funnel and 1:1 volume of ethanol to water (60 ml:60 ml) was added followed by 50 ml of toluene. The mixture was shaken three times with draining of aqueous phase after each. Then the mixture was washed, shaken and aqueous phase separated with 3 additions of distilled water. The procedure of extraction with toluene, washing with ethanol and water, filtering of CG200PS and redispersing was carried out three times. After the last filtration, instead of redispersing CG200PS, the nanotubes were washed with toluene, ethanol and acetone and dried on a weighing boat after scraping from the filter paper. Dried CG200PS was transferred into a vial and was dried in ambient air over night.

For the SWNT functionalization the mole ratio of carbon (SWNT) to lithium was 1: 16 and the mole ratio of carbon (SWNT) to styrene was 1:6. 50 mg of SWNT was functionalized for each reaction batch and condensed ammonia volume was kept between 70 – 100ml. Typical mass of lithium used was 500 mg and the typical volume of styrene used was 3 ml. The CG200PS accumulated from the different reaction runs were grounded using mortar and pestel before preparing the dispersion in UPR.

3.7 SWNT Functionalization by Polystyrene-co-Acrylonitrile (SAN)

The non-covalent functionalization of SWNT by SAN was carried out by sonication. 100 ml of dimethylformamide (DMF) was poured in a round-bottomed 3-neck flask. An argon supply was connected to one side port and other side port was connected to an oil bubbler. The center port was used to insert the tapered sonication tip which was submerged midway into DMF. 100 mg of SWNT (CG200) was weighed into a 10 ml vial and added by removing the oil bubbler port and switching off the argon flow. The 3-neck flask containing SWNT-DMF mixture was submerged in an ice-water bath during the process of sonication with Argon flow over the sonicating mixture. The sonication setting used was 25 % amplitude with pulse setting 5 seconds on and 3 seconds off. Continuous sonication was carried out for 10 minute cycle with 6 cycles making the total sonication time 60 minutes. After 30 minutes of total sonication, 400 mg of SAN was added and last 30 minutes of sonication was carried out on a mixture of SWNT, SAN and DMF. After sonication, the mixture was stirred overnight using magnetic stir bar over a magnetic stir plate. The work up on the following day involved coagulating the dispersed SWNT by adding water around 50 ml and vacuum filtering the mixture using a 1.0 μm polycarbonate filter paper. The collected sample on the filter paper was redispersed in ethanol/acetone mixture and filtered through 0.47 μm PTFE membrane filter. The contents of the filter were initially dried under ambient air overnight (most of the flammable organics evaporated) followed by drying it over hot plate on watch glass at 50°C. The non-covalent SWNTSAN (CG200SAN) dried sample was grounded using a mortar and pestle before preparing dispersion in UPR.

CHAPTER 4 VISCOELASTIC BEHAVIOR OF SWNT IN UPR: EFFECT OF CHIRALITY AND PURITY

In this research, dispersions of four commercial SWNT products in unsaturated polyester resin (UPR) were compared to gain a detailed understanding of the effects of purity and chirality on viscoelasticity. UPR was chosen as the resin based on our previous research,[20,147] its continued dominance of the global thermoset market, and the fact that there has still be limited research on improving UPR properties via the incorporation of SWNT. Four SWNT products were obtained from SouthWest Nanotechnologies: CG200, CG300, SG65 and SG65i. The chirality distribution of CG200 consists primarily of metallic SWNT; CG300, a more recently commercialized analog, has a narrower distribution and a lower fraction of non-SWNT carbon impurities. In contrast, SG65 has a relatively high fraction of non-SWNT carbon but contains approximately 40% semiconducting SWNT chiralities, particularly *(6,5)* SWNT. SG65i has a similar chirality distribution as SG65 but the purity of CG300. At least five dispersions of each product in UPR were prepared at comparable volume fractions of SWNT.

4.1 SWNT Properties

Table 4.1 summarizes key properties of CG200, CG300, SG65 and SG65i. XPS showed no significant differences in SWNT surface chemistry. Both CG200 and SG65 had ~8 wt % catalyst residue while CG300 and SG65i had ~ 3 wt % catalyst residue; these values are comparable to previous work on other types of purified SWNT. However, the SG65 had a much higher percentage of non-SWNT carbon (MWNT, graphite, carbon fibers)[148] and a higher D/G ratio than the other products. The TGA plots and Raman spectra are displayed in Figures 3.1 and 3.2. The second derivative peak for SG65 in the TGA plot and higher intensity D peak in the Raman spectra are evidences of the higher impurities in SG65 SWNT product. The samples also had similar size distributions. The large carbon impurities in SG65, were a significant hindrance to meaningful AFM imaging of C12-SWNT. Measurements on aqueous dsDNA stabilized SG65 supernatants yielded clearer images. Since dsDNA dispersion requires tip sonication which shortens SWNT, the length of the SG65 was estimated based on the ratio of the measured C12-SWNT length to dsDNA-SWNT length for the other samples. The radius/length (R/L) ratio for each type of SWNT provides an approximation of the theoretical volume fraction required for rheological percolation.

Table 4.1 Summary of SWNT Properties

SWNT grade	SWNT (wt%)	Non-SWNT Carbon (wt%)	Catalyst (wt%)	Raman D/G 785, 514 nm	Avg. Diameter (nm)	Avg. Length (nm)	R/L
CG200 Lot.14	85	8	7	0.07, 0.06	1.00	470	0.0011
CG300 Lot.32	95	2	2	0.05, 0.04	0.96	427	0.0011
SG65 Lot.35	69	23	8	0.14, 0.07	0.95	496*	0.0010
SG65i Lot.48	94	3	3	0.11, 0.03	0.82	498	0.0008

(* Length estimated by scaling the average length from SWNT-dsDNA supernatants by the average C12-SWNT:dsDNA-SWNT length ratio for CG200 and SG65i)

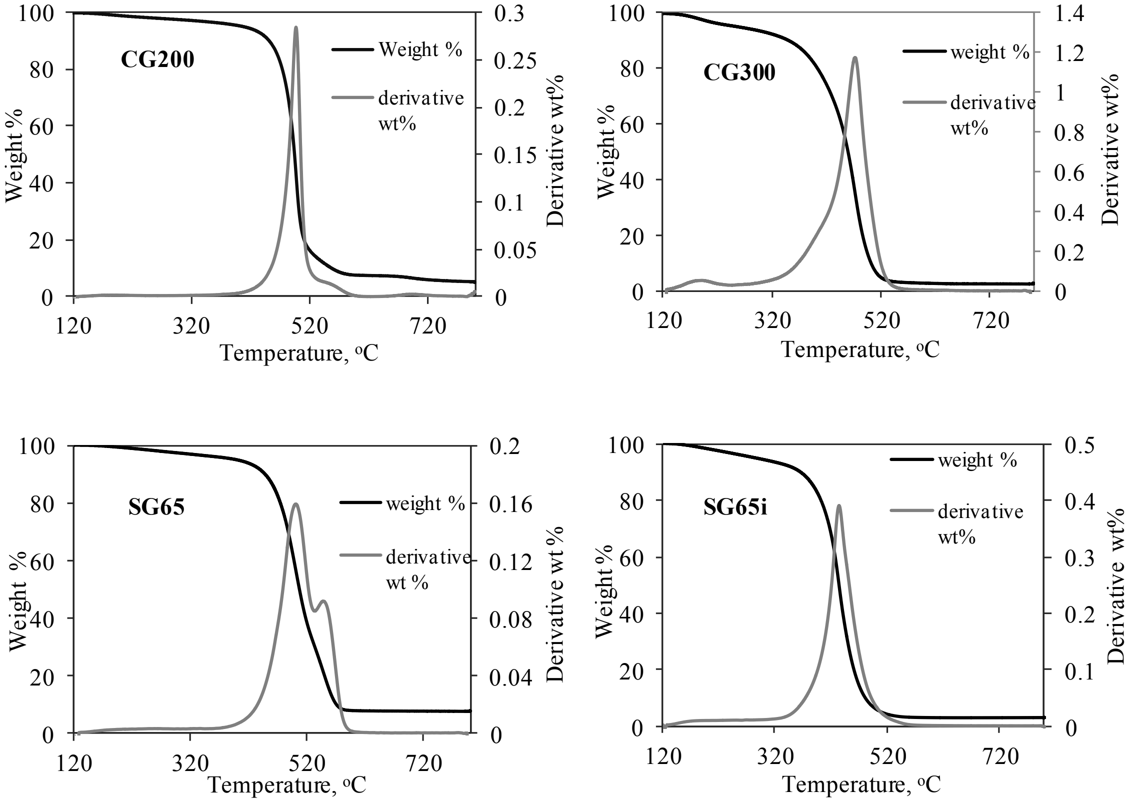

Figure 4.1 TGA runs of CG200, CG300, SG65 and SG65i in air. TGA plots were used to calculate mass fractions of pure SWNT, non-SWNT carbon, and catalyst.

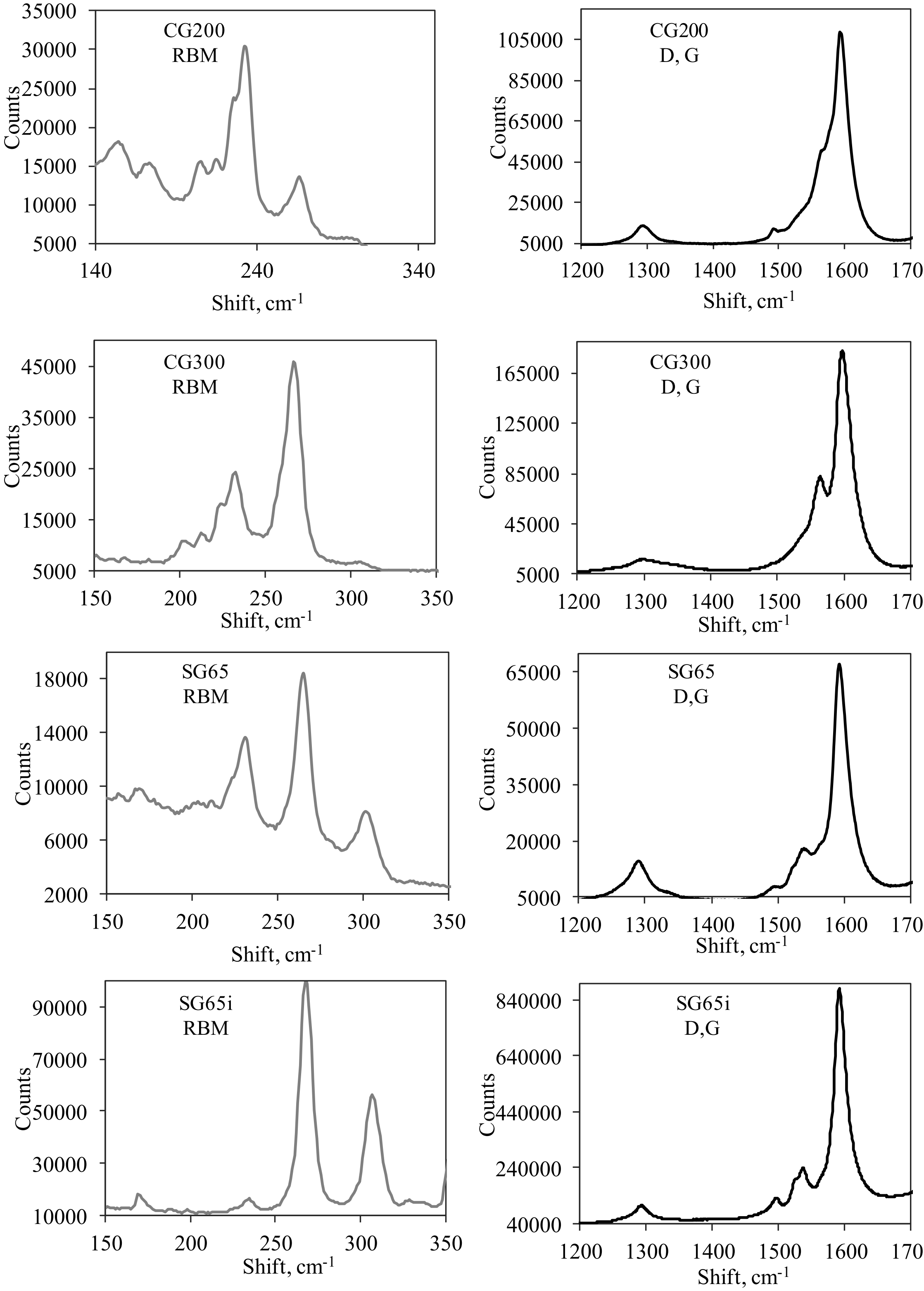

Figure 4.2 Raman characterization of CG200, CG300, SG65 and SG65i by 785 nm laser showing RBM modes, D and G bands

4.2 Dispersion Characterization: Optical Microscopy

Optical microscopy of the dispersions did not reveal any obvious differences (Figure 3.3) between the SWNT dispersion states at a given concentration. At low concentration, grey SWNT-rich regions were interspersed with lighter resin-rich regions; a few dense black aggregates were present. With increasing concentration, the SWNT-rich phase became more dominant, more aggregates were observed, and the SWNT network completely filled the image at a concentration of $\phi = 0.23 \pm 0.02$ vol %.

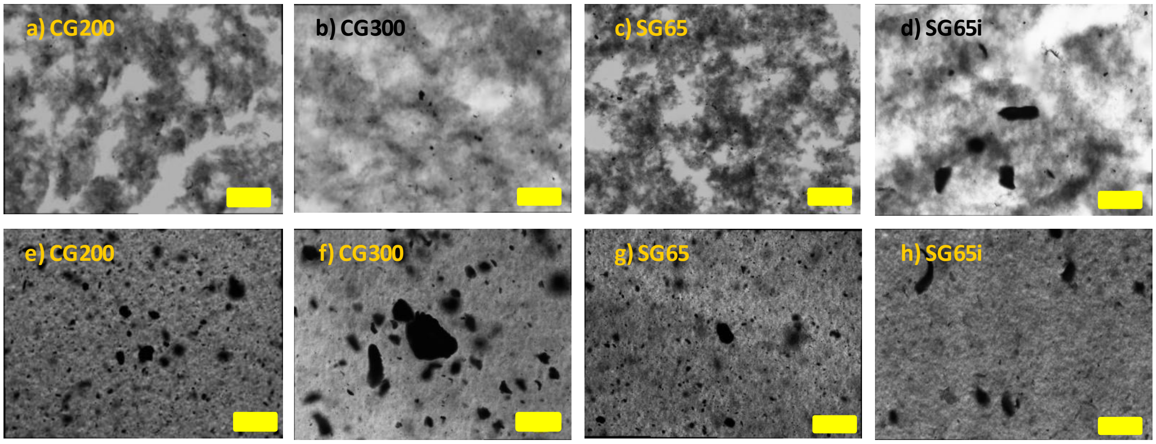

Figure 4.3 Optical microscopy images of SWNT-UPR dispersions (40X magnifications stitched over an area of 0.97 x 0.73 mm). Top row (a, b, c, d) 0.05 vol %; Bottom row (e, f, g, h) 0.23 (± 0.02 vol %). Scale bar 100 μm.

4.3 Dispersion Characterization: Rheology

Steady Shear Rheology

While optical microscopy is useful for probing dramatic differences between dispersions, rheology is a much more sensitive, quantitative method. Generally, in the absence of lyotropic phase behavior, higher viscosity η is indicative of better dispersion. In addition, steady shear viscosity has practical implications for transporting and processing dispersions. Figure 4.4 shows that steady shear viscosity measurements enable more distinctions between samples than optical microscopy. All the dispersions exhibited both a low shear viscosity that was significantly higher than the 3.1 Pa s Newtonian viscosity of the UPR and shear thinning behavior. CG200 displayed lower steady shear viscosities than the other SWNT types at all concentrations except 0.05 vol % where it was higher than SG65. Another notable difference between the dispersions was that the two highest CG200 concentrations exhibited some evidence of a low shear Newtonian plateau. For a given concentration, steady shear viscosities for the CG300 and SG65i dispersions were always greater than those for their lower purity versions (CG200 and SG65). Although it was less pronounced for CG200, all samples showed a significant viscosity increase from 0.05 to 0.10 vol %. At the higher concentrations, CG300 had a markedly higher viscosity than even SG65i. For example, at 0.22 ± 0.02 vol %, the low shear viscosities (0.01 s^{-1}) for CG200, CG300, SG65 and SG65i were 1460, 5390, 2600 and 4450 Pa s respectively. The higher viscosities for the CG300 and SG65i relative to their lower purity versions (CG200 and SG65), is attributed to the higher purity grades having fewer lower aspect ratio impurities. It is interesting that the viscosity of CG300 is greater than that for SG65i while the viscosity of CG200 is less than that of SG65. This may simply be due to the large fraction of non-SWNT carbon in SG65 resulting in a much larger total carbon mass in the SG65 than in the CG200. At high shear, flow alignment results in the viscosity approaching that of the Newtonian UPR resulting in curvature of the data. This curvature can be removed by plotting the specific viscosity $\eta_{sp} = (\eta - \eta_s)/\eta_s$ (Figure 4.5); reduced viscosity ($\eta_r = \eta_{sp}/\phi$) plots are also shown in the Figure 4.6. The lines in Figure 3.4 represent the Sisko model fit $\eta = \eta_\infty + k\dot{\gamma}^{(n-1)}$. The Sisko model simply adds the infinite shear viscosity η_∞ to the standard power law model where and k and n are the consistency and power law indices, respectively. This model worked best for intermediate concentrations, and chosen over the more commonly used Cross or Carreau-Yasuda models due to the lack of a well-defined plateau in all data. All model parameters are given in Tables 4.2 – 4.5.

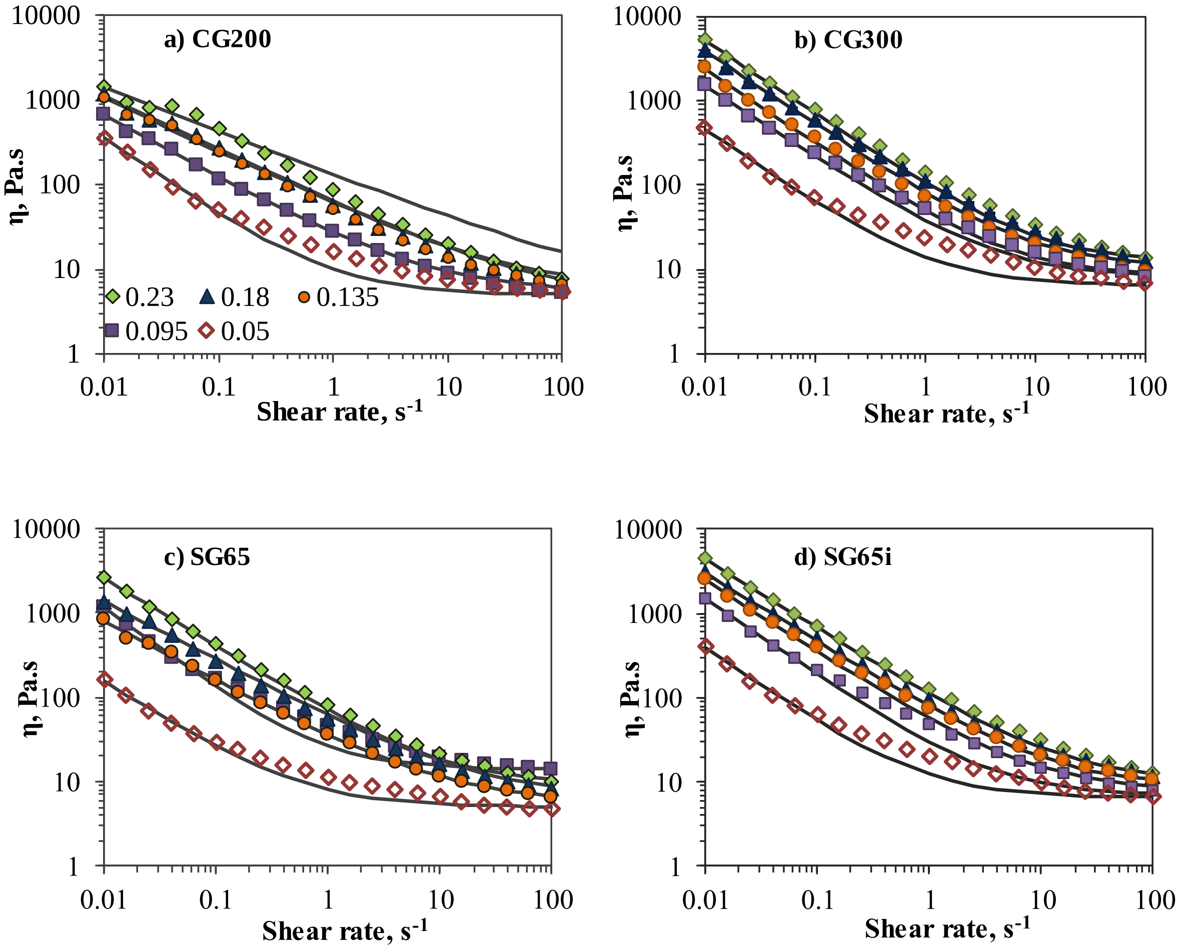

Figure 4.4 Steady shear rheology curves of viscosity as function of shear rate for SWNT-UPR dispersions at different SWNT concentrations; viscosity vs shear rate with Sisko model fit (a, b, c, and d). Symbol key: (◇) 0.05, (■) 0.095 (±0.005), (●) 0.14 (± 0.005), (▲) 0.18 (± 0.01) and (♦) 0.23 (± 0.02) vol %. Error bars: < 9 %

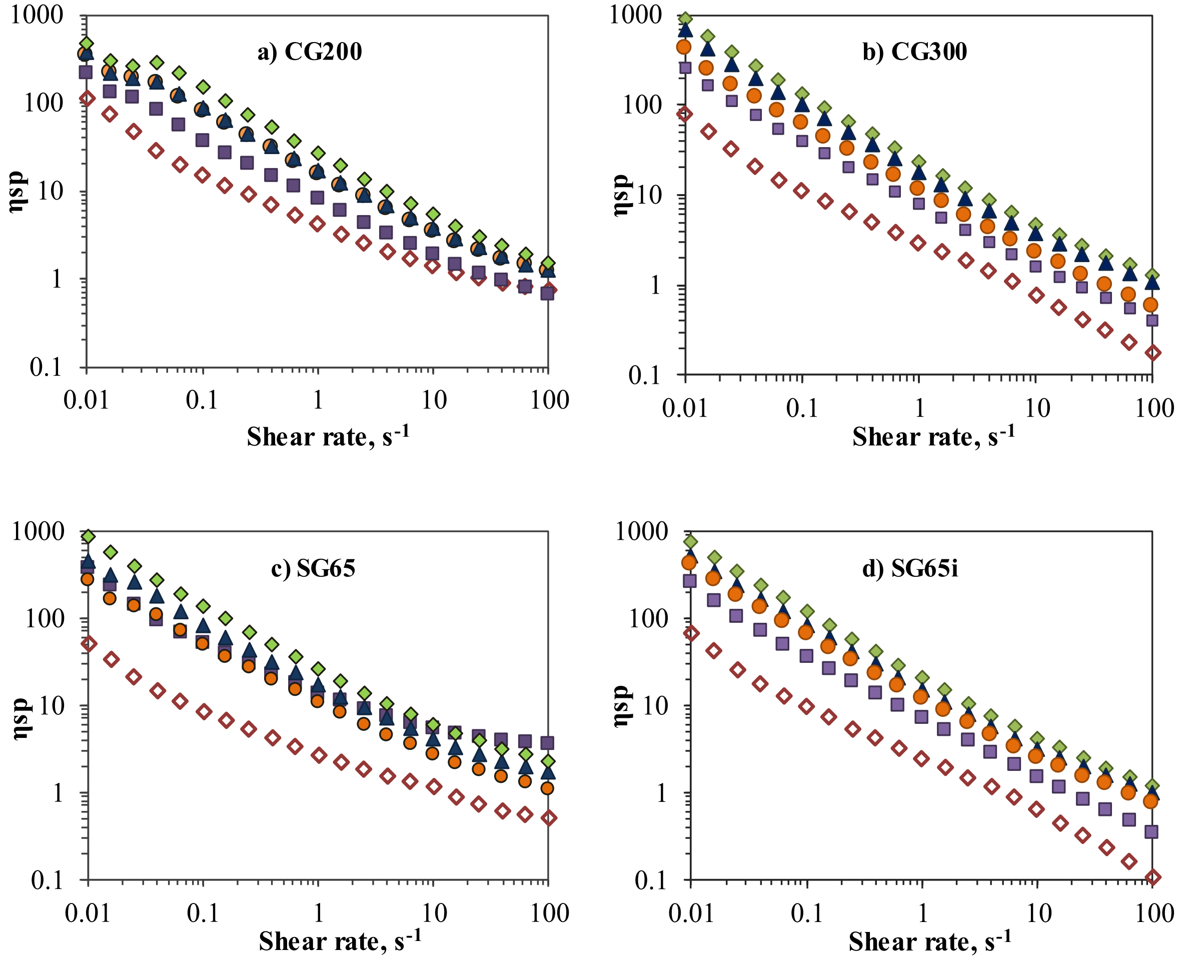

Figure 4.5 Specific viscosity plots of SWNT-UPR. UPR viscosity used for CG300 and SG65i was 5.96 Pa s. (a) CG200, (b) CG300, (c) SG65, (d) SG65i. Symbol key: (◊) 0.05 (±0.005), (■) 0.09 (±0.005), (●) 0.14 (± 0.005), (▲) 0.18 (±0.01) and (♦) 0.23 (±0.02) vol %.

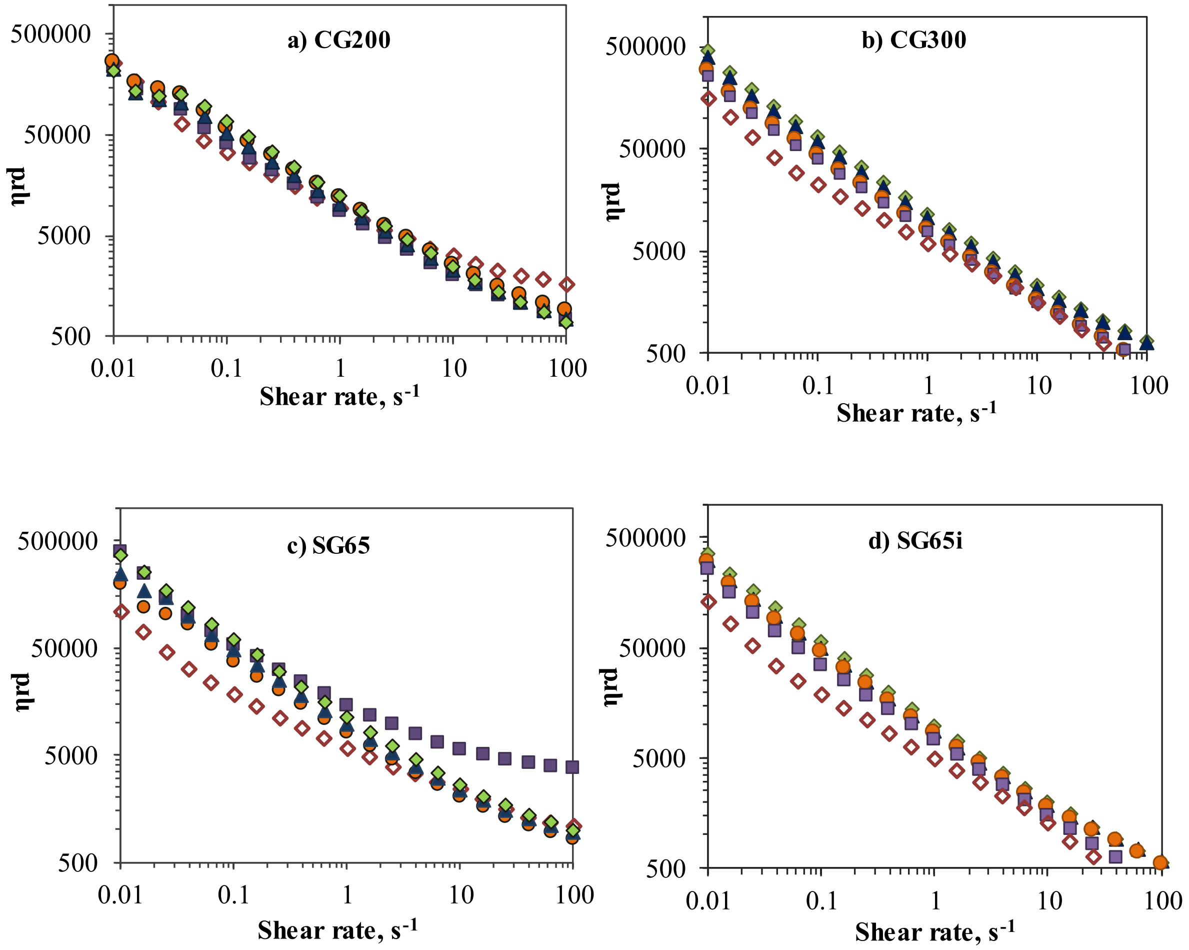

Figure 4.6 Reduced viscosity plots of SWNT-UPR. UPR viscosity used for CG300 and SG65i was 5.96 Pa.s. (a) CG200, (b) CG300, (c) SG65, (d) SG65i. Symbol key: (◊) 0.05 (±0.005), (■) 0.09 (±0.005), (●) 0.14 (± 0.005), (▲) 0.18 (±0.01) and (♦) 0.23 (±0.02) vol %.

Table 4.2 Fitting parameters for rheological model fits for flow curve of CG200-UPR

Sisko model: $\eta = \eta_{\infty} + k\dot{\gamma}^{n-1}$

	Sisko model fitting parameters			Goodness of fit		
vol %	n	k	η_∞	R^2	adjusted R^2	SSE
0.05	0.08	4.98	5.0	0.9968	0.9966	5.26
0.09	0.27	22.1	5.3	0.9929	0.9921	15.6
0.13	0.37	56.4	5.5	0.9869	0.9854	35.2
0.18	0.37	60.2	4.1	0.9832	0.9813	41.9
0.22	0.50	138	3.1	0.9676	0.9641	77.8

Table 4.3 Fitting parameters for rheological model fits for flow curve of CG300-UPR

Sisko model: $\eta = \eta_{\infty} + k\dot{\gamma}^{n-1}$

	Sisko model fitting parameters			Goodness of fit		
vol%	n	k	η_∞	R^2	adjusted R^2	SSE
0.05	0.11	7.67	6.5	0.9956	0.9954	1240
0.10	0.16	30.9	8.0	0.9978	0.9976	6750
0.14	0.12	41.9	8.5	0.9961	0.9957	30400
0.17	0.13	72.4	11	0.9977	0.9974	49500
0.20	0.13	96.6	12	0.9979	0.9977	79000

Table 4.4 Fitting parameters for rheological model fits for flow curve of SG65-UPR

Sisko model: $\eta = \eta_{\infty} + k\dot{\gamma}^{n-1}$

	Sisko model fitting parameters			Goodness of fit		
vol%	n	k	η_∞	R^2	adjusted R^2	SSE
0.05	0.15	3.09	5.0	0.9935	0.9942	172
0.10	0.026	12.9	14	0.9953	0.9948	7960
0.14	0.29	30.6	5.6	0.9899	0.9887	9450
0.19	0.30	55.8	6.5	0.9963	0.9959	10500
0.25	0.19	61.8	9.0	0.9996	0.9995	3900

Table 4.5 Fitting parameters for rheological model fits for flow curve of SG65i-UPR

Sisko model: $\eta = \eta_\infty + k\dot{\gamma}^{n-1}$

	Sisko model fitting parameters			**Goodness of fit**		
vol%	n	k	η_∞	R^2	adjusted R^2	SSE
0.05	0.0975	6.00	6.5	0.9947	0.9941	1030
0.10	0.0929	22.9	7.0	0.9968	0.9965	9390
0.14	0.1561	50.2	8.0	0.9981	0.9979	15700
0.17	0.1836	70.7	9.0	0.999	0.9989	12400
0.20	0.183	102	10	0.9992	0.9992	20300

Oscillatory Shear Rheology

Comparing viscoelastic behavior measured by oscillatory shear rheology has proven to be a powerful tool for understanding SWNT dispersion behavior.[147,149-153] In addition, viscoelasticity provides a qualitative indication of the mechanical properties of the final composites. Viscoelasticity measurements can determine the rheological percolation threshold, the concentration of nanotubes at which the nanotubes form a polymer spanning network that can provide mechanical property enhancement. However, additional details about the dispersion microstructure and relative strength of nanotube-nanotube and nanotube-polymer interactions can also be discerned through analysis of viscoelastic properties. For example, Kayatin and Davis as well as Chatterjee and Krishnamoorti showed superposition of viscoelastic moduli due to the similar nature of CNT structure growth with concentration.[20,149] Viscoelastic property relations were used to calculate fractal structure features of nanotube dispersions by Khalkhal et al and Urena-Benavides et al.[147,152] Filiponne and Luna extended these, and similar superposition approaches to propose a universal approach for understanding viscoelasticity in polymer composites.[108]

In this research, the linear viscoelastic region for each dispersion was determined by probing increasing amplitude at a constant frequency of 10 rad/s; a 2 % decrease in *G'* was used to define the critical strain γ_c. Table 4.6 displays the linear viscoelastic behavior for the SWNT-UPR dispersions. Elastic behavior increased with SWNT concentration and the strain limit for the linear regime decreased. At similar concentrations, *G'* values of CG200 were typically ~ 20% lower than CG300 and SG65i, but appreciably higher than those for SG65. Critical strains for CG200 were generally lower than CG300 and SG65i. CG300 and SG65i had similar *G'* and γ_c. At all concentrations, SG65 exhibited lower *G'* and higher γ_c than the other SWNT types; this is attributed to the much higher quantity of non-SWNT carbon. The *tanδ* values provide further evidence of SG65 having more fluid behavior than the other materials; for SG65 dominant solid behavior was observed at 0.14 vol % and for all other SWNT types it started at 0.10 vol %.

Table 4.6 Comparison of linear viscoelastic regimes in UPR.

CG200				**CG300**			
Vol %	γ_c, %	G', Pa	tan δ	Vol %	γ_c, %	G', Pa	tan δ
0.045	1.66	55.0	1.90	0.05	2.25	67.0	1.90
0.092	1.16	177	0.93	0.10	0.99	283	0.81
0.13	0.68	400	0.63	0.14	0.81	475	0.66
0.17	0.66	475	0.59	0.17	0.61	868	0.56
0.22	0.44	1020	0.44	0.20	0.50	1280	0.48

SG65				**SG65i**			
Vol %	γ_c, %	G', Pa	tan δ	Vol %	γ_c, %	G', Pa	tan δ
0.05	3.11	24.0	3.00	0.05	2.30	57.0	2.00
0.10	1.38	168	1.70	0.10	0.92	271	0.82
0.14	1.11	220	0.85	0.14	0.63	488	0.66
0.19	1.00	373	0.72	0.17	0.62	724	0.59
0.25	0.71	577	0.62	0.21	0.45	1150	0.47

Frequency sweep tests at amplitudes below ω_c further clarified differences in the viscoelasticity of the SWNT dispersions. Plots of *G'* and *G"* delineate the solid-like contribution of the SWNT network and viscous nature of polymer matrix respectively, in accordance with the two phase contribution to viscoelasticity described by Filippone et al.[108] Figure 4.7 shows changes in *G'* as a function of frequency ω and concentration ω for the four SWNT-UPR systems; *G"* behavior is displayed in Figure 4.8. Even at this relatively low concentration (0.05 vol %), *G'* and *G"* deviated from terminal behavior ($G' \propto \omega^2$, $G'' \propto \omega$).[87] Numerical data for *G'* and *G"* at ω = 0.01 rad/s, and the low frequency slopes are shown in Table 4.7. At 0.05 vol %, *G'* (ω = 0.01 rad/s) was 11 ± 1 Pa for CG200, CG300 and SG65i; these values were over three times higher than that of SG65. At 0.095 vol % and above, the values for CG200 were lower than those for CG300 and SG65i but still significantly higher than those for SG65. There was a marked increase in increase in *G'* between 0.050 and 0.095 ± 0.005 vol % for all four SWNT. The Cole-Cole plots in Figure 4.9 further highlight that these concentrations had markedly different microstructures, while there were less pronounced microstructural differences between higher concentrations.

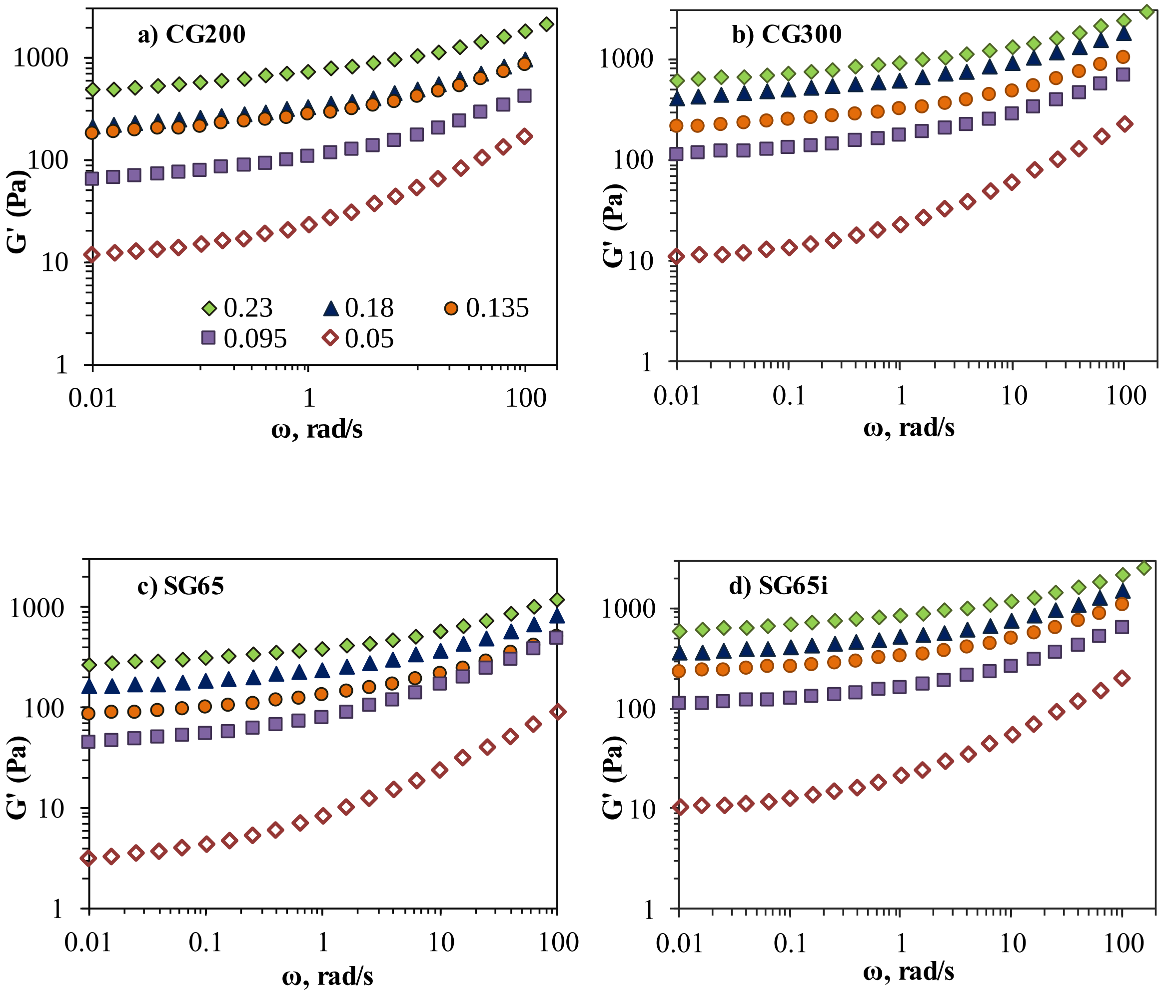

Figure 4.7 Oscillatory shear rheology on SWNT-UPR displaying variation of *G'* with angular frequency different SWNT concentrations (Error < 12 %). Symbol key: (◊) 0.05 (±0.005), (■) 0.095 (±0.005), (●) 0.14 (± 0.005), (▲) 0.18 (± 0.01) and (♦) 0.23 (± 0.02) vol %.

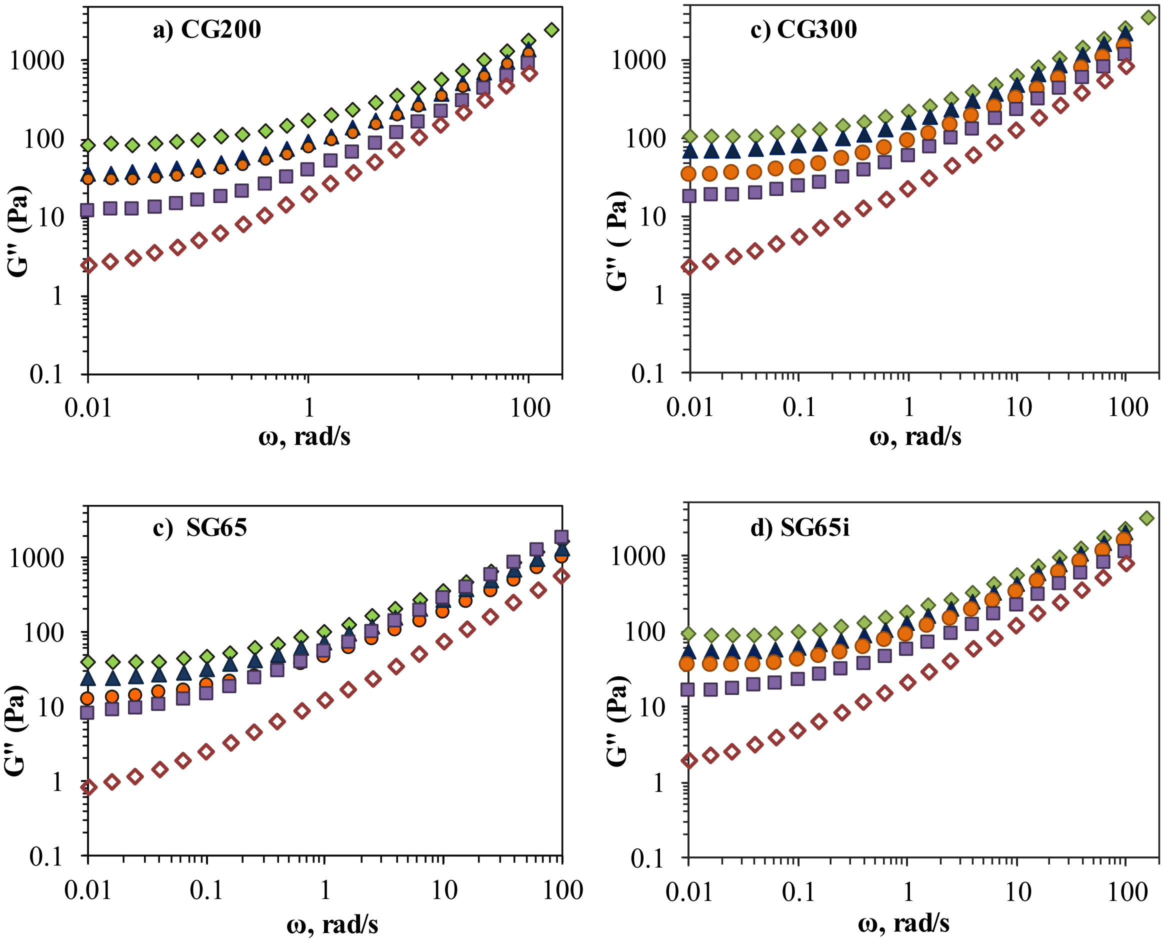

Figure 4.8 Oscillatory shear rheology on SWNT-UPR displaying variation of *G"* with angular frequency different SWNT concentrations. (a) CG200, (b) CG300, (c) SG65, (d) SG65i. Symbol keys: (◊) 0.05, (■)0.095 (±0.005), (●) 0.14 (± 0.005), (▲)0.18 (± 0.01) and (♦) 0.23 (± 0.02) vol %. Error bar: < 12 %

Table 4.7 Low frequency ($\omega = 0.01\text{s}^{-1}$) storage *G'* and loss *G"* modulus.

CG200				**CG300**			
Vol %	Slope G'	Slope G"	G' (Pa)	Vol %	Slope G'	Slope G"	G' (Pa)
0.05	0.10	0.30	12.0	0.05	0.09	0.40	11.0
0.09	0.09	0.10	65.0	0.10	0.07	0.10	114
0.13	0.08	0.08	180	0.14	0.07	0.10	212
0.17	0.08	0.09	212	0.17	0.07	0.07	416
0.22	0.08	0.08	485	0.20	0.07	0.06	617

SG65				**SG65i**			
Vol %	Slope G'	Slope G"	G' (Pa)	Vol %	Slope G'	Slope G"	G' (Pa)
0.05	0.10	0.50	3.00	0.05	0.08	0.40	10.0
0.01	0.09	0.30	45.0	0.10	0.06	0.10	110
0.14	0.07	0.20	86.0	0.14	0.06	0.07	234
0.19	0.07	0.10	161	0.17	0.07	0.06	355
0.25	0.06	0.08	270	0.21	0.06	0.06	597

As described by Kayatin and Davis, and and Chen et al.,[20,154] mastercurves for viscoelastic properties were constructed by scaling the moduli by the corresponding values at the crossover point. Above ω_c the properties are dominated by the viscous UPR, and below ω_c they are dominated by the SWNT network. Figure 4.10 displays mastercurves following the above approach for our SWNT-UPR disperisons. The striking collapse indicates that all viscoelastic moduli have a similar functional form and the magnitudes are a function of cluster size increasing with concentration.[154] Trappe and Weitz established a similar scaling methodology base on using the low frequency moduli instead of crossover values.[155] This method is best suited for concentrations above percolation. As shown in Figure 4.11, this method gives less striking collapse due to inaccuracies in measuring *G'* as $\omega \to 0$ for low concentrations. The values of shift factors for the two types of mastercurves are shown in Table 4.8.

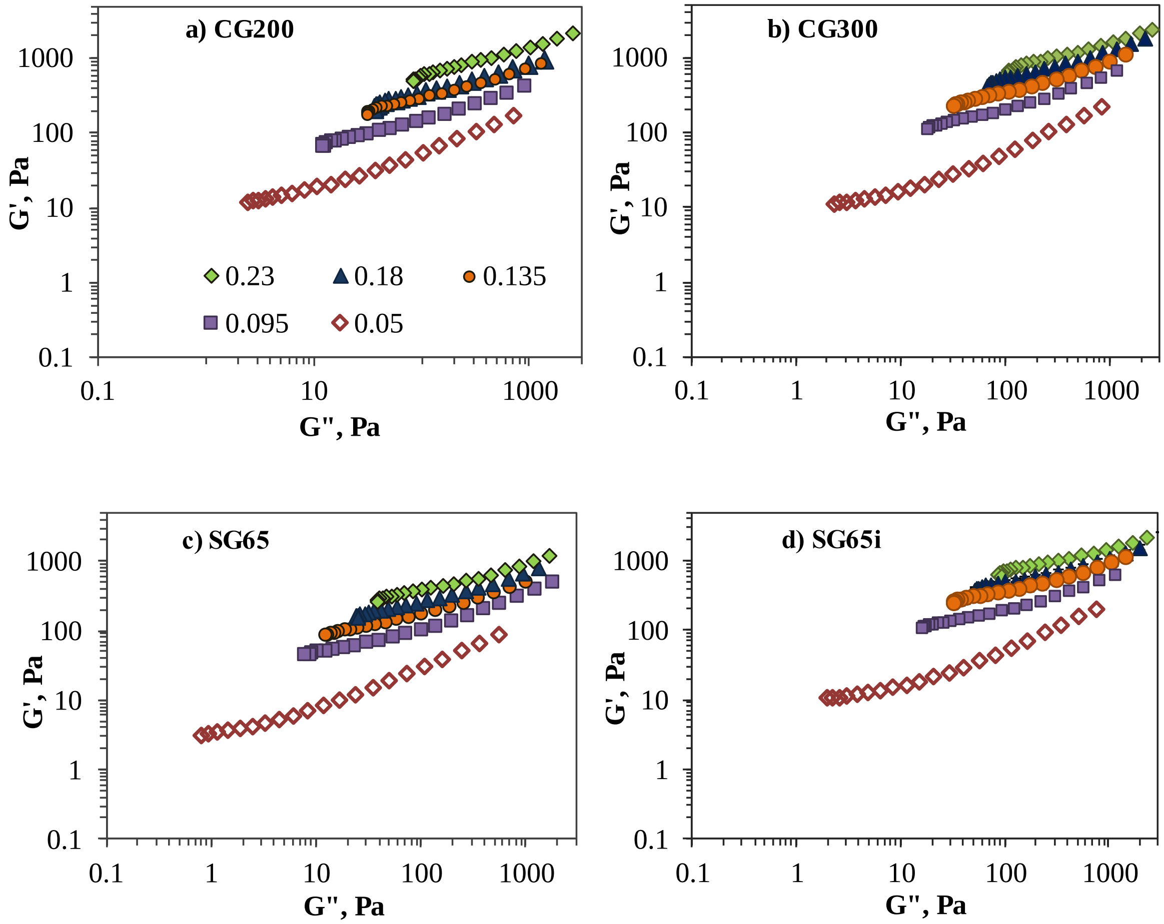

Figure 4.9 Cole-Cole plot of *G'* versus *G"* variation with angular frequency at different SWNT concentrations. Symbol key: (◊) 0.05 (±0.005), (■) 0.095 (±0.005), (●) 0.14 (± 0.005), (▲) 0.18 (± 0.01) and (♦) 0.23 (± 0.02) vol %. (◊) 0.05, (■) 0.09. Error: < 12 %

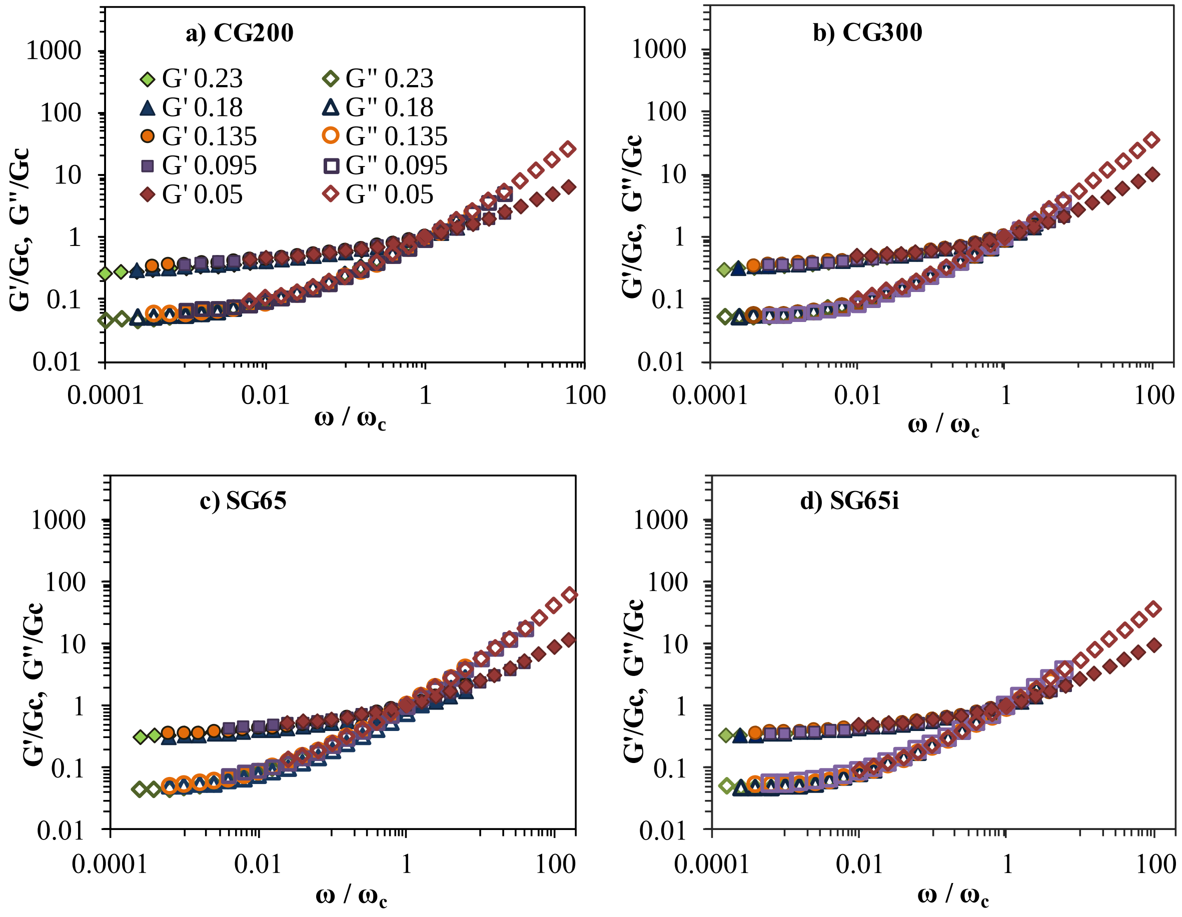

Figure 4.10 Master curves for SWNT-UPR dispersions superimposed using G_c and ω_c as shift factors. (a) CG200, (b) CG300, (c) SG65, (d) SG65i. Symbol key: scaled G'- (♦) 0.05 (±0.005), (■) 0.095 (±0.005), (●) 0.14 (± 0.005), (▲) 0.18 (± 0.01), (♦) 0.23 (± 0.02) vol %; scale G''- (◊) 0.05, (□) 0.095 (±0.005), (○) 0.14 (± 0.005), (Δ) 0.18 (± 0.01), (◊) 0.23 (± 0.02) vol %. Error: < 12 %

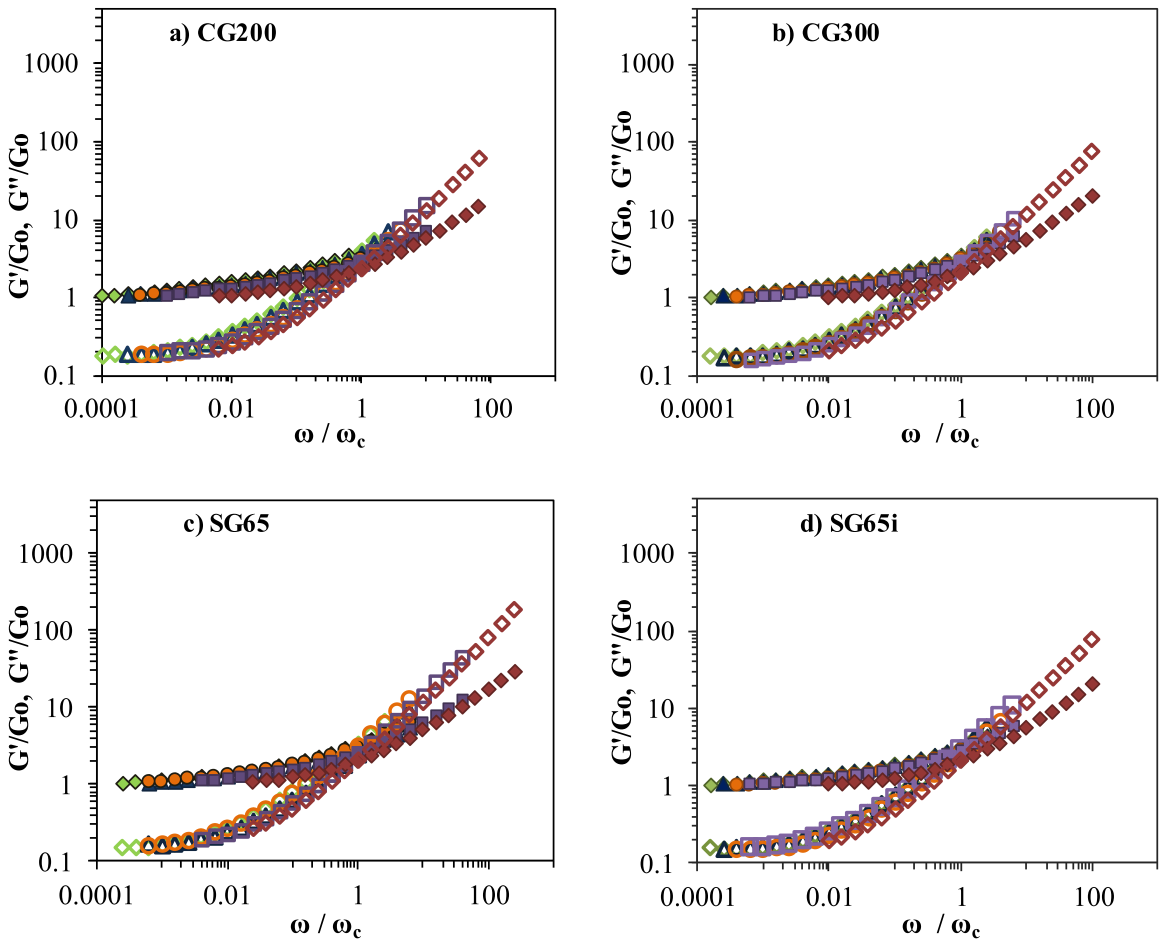

Figure 4.11 Master curves for SWNT-UPR systems. (a) CG200, (b) CG300, (c) SG65, (d) SG65i superimposed parameters by *G'ₒ* and *ω꜀*. Symbols: scaled i- (♦) 0.05, (■) 0.095 (±0.005), (●) 0.14 (± 0.005), (▲) 0.18 (± 0.01), (♦) 0.23 (± 0.02) vol %; scaled *G"*- (◊) 0.05, (□) 0.095 (±0.005), (○) 0.14 (± 0.005), (∆) 0.18 (± 0.01), (◊) 0.23 (± 0.02) vol %.

Table 4.8 Shift factors for construction of the four master curves

CG200				CG300			
vol %	ω_c (rad/s)	G'_o (Pa) (Fig 4.11)	G'_c (Pa) (Fig 4.10)	vol %	ω_c (rad/s)	G'_o (Pa) (Fig 4.11)	G'_c (Pa) (Fig 4.10)
0.05	1.58	11.93	27.02	0.05	1	11	23.4
0.09	10	64.79	177.5	0.1	15.8	110	332
0.13	25.1	179.82	531.6	0.14	25.1	205	629
0.17	39.8	212.06	711.6	0.17	39.8	400	1313
0.22	99.8	484.74	1838.26	0.2	63	600	2080

SG65				SG65i			
vol %	ω_c (rad/s)	G'_o (Pa) (Fig 4.11)	G'_c (Pa) (Fig 4.10)	vol %	ω_c (rad/s)	G'_o (Pa) (Fig 4.11)	G'_c (Pa) (Fig 4.10)
0.05	0.251	5.326	3	0.05	1	10	21.1
0.1	2.51	103.05	40	0.1	15.8	105	307
0.15	10	217.58	80	0.14	25.1	230	643
0.19	15.8	421.6	150	0.17	39.8	340	1081
0.25	25.1	738.51	260	0.21	63	580	1835

4.4 Percolation and Network Characteristics

There are several established methods for estimating the critical concentration for rheological percolation ϕ_c; the results from several methods are typically compared to provide the most accurate value for ϕ_c. The simplest method is inspection of the G’ versus frequency plots. Both an order of magnitude increase and a plateau in *G’* versus ω are often used to provide a first approximation for ϕ_c, based on these criteria inspection of Figure 4.7 suggests that $\phi_c \approx 0.1$ vol % for all four SWNT. Pogodina and Winter and Romasanta et al., used plots *tanδ* versus ω to identify the formation of a percolated network.[156,157] With increasing concentration, G’ increases at a faster rate than G” resulting in $\tan\delta = G''/G' < 1$. Upon network formation, low frequency *tanδ* plateau emerges.[157]

Figure 4.12 shows a clear low frequency (0.01 - 0.1 rad/s) *tanδ* plateau exists for CG200, CG300 and SG65i at ~ 0.1 vol %, but a plateau was less evident for SG65. The plateau behavior suggests ϕ_c is approximately 0.1 vol %, but slightly higher for SG65.

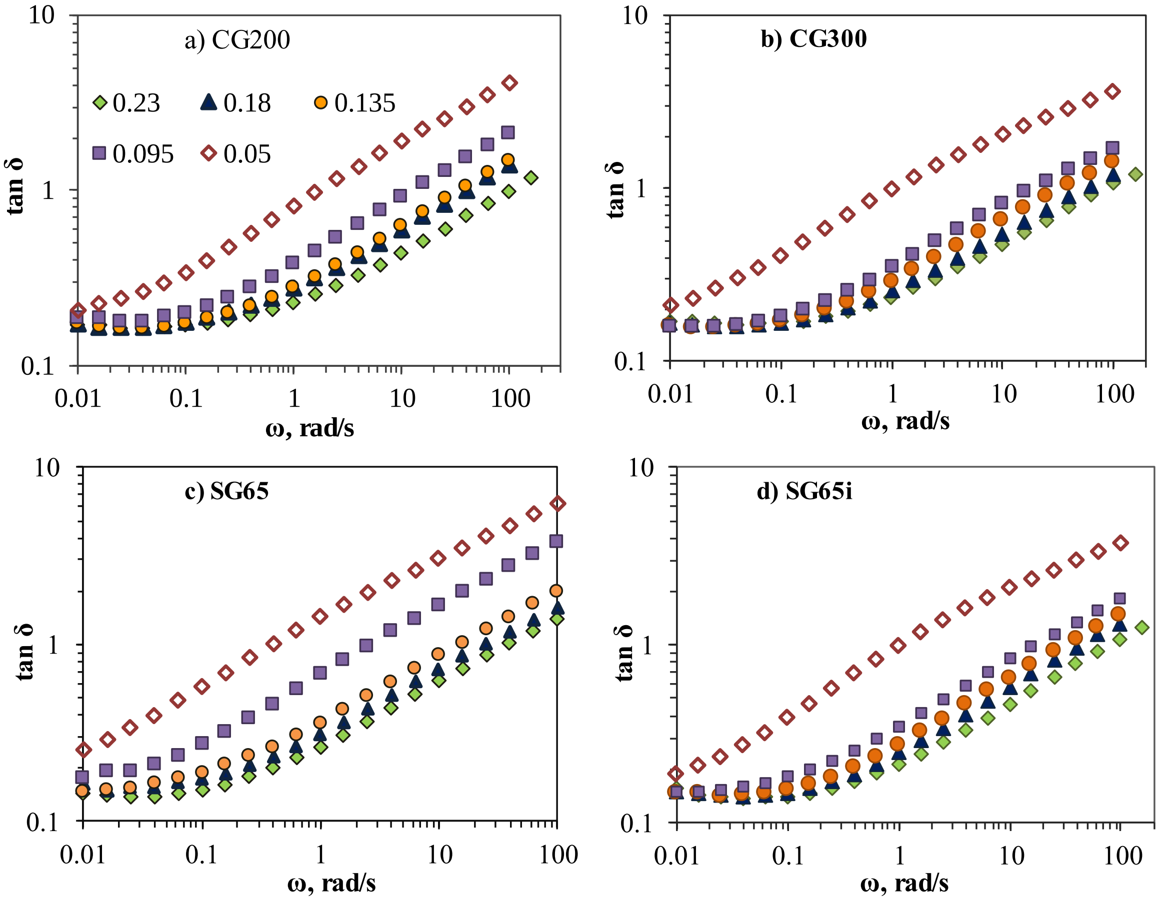

Figure 4.12 Damping factor *tanδ* as a function of angular frequency (a) CG200, (b) CG300, (c) SG65, (d) SG65i; (◊) 0.050 (±0.005),, (■) 0.095 (±0.005), (●) 0.14 (± 0.005), (▲) 0.18 (± 0.01) and (♦) 0.23 (± 0.02) vol %. Error bars < 12 %

A similar result was obtained by estimating percolation based on the divergence of the complex modulus G^* versus complex viscosity η^* based on the method described by Mitchell et al. and others.[16,20,147] The x-intercepts of the linear regions of the plots of G^* vs ϕ (Figure 4.13 a - d) resulted in ϕ_c values of 0.082 ($R^2 = 0.92$), 0.086 ($R^2 = 0.95$), 0.082 ($R^2 = 0.98$) and 0.082 ($R^2 = 0.97$) vol % for CG200, CG300, SG65, and SG65i, respectively.

Percolation was also estimated by the frequently used method of fitting the power law relation $G_o' \propto (\phi - \phi_c)^{\beta}$ by adjusting ϕ_c values in the percolation range to maximize the R^2 value (Figure 4.13 e, f). This resulted in slightly lower estimates of ϕ_c : 0.060 vol % for CG200 and 0.065 vol % for the other SWNT types. Comparison of the results shows that $0.06 \leq \phi_c \leq 0.10$. This result is consistent with $\phi_c \approx R/L$ which suggests many SWNT are dispersed as individuals as was the case for HiPCo SWNT.[20] Somewhat surprisingly, neither the differences in chirality (and therefore diameter distribution) or the significant differences in the amount of non-SWNT carbon impurities had a discernable effect on percolation.

In addition to being one of the most common methods for determining ϕ_c, the relation $G'_o \propto (\phi - \phi_c)^{\beta}$ also provides qualitative information about dispersion microstructure. The magnitude of β defines the network response to stress-induced deformations. In simulation work on percolated elastic networks, Arbabi and Sahimi categorized elastic networks that undergo attraction induced flocculation and found β ~ 2.10 is indicative of particle bonds that are resistant to stretching but free to rotate and β ~ 3.75 is indicative of networks where both bond stretching and rotation were resisted.[158] Surve et al extended this to polymer nanocomposites and found β ~ 1.88 when network formation is assisted by polymer bridging and there are significant polymer-nanoparticle interactions.[109] Filippone et al compared several nanoparticle-polymer systems, and concluded that higher values of β result from a higher degree of nanoparticle-nanoparticle interactions in comparison to nanoparticle-polymer interactions. In other words, lower values of β indicate better nanoparticle-polymer interaction.[108] Similar conclusions were proposed by Surve et al in their comparison of several polymer-filler systems.[109] Based on the range of values ϕ_c for the SWNT-UPR systems in this research, $1.15 < \beta < 1.27$; this compares to the previously reported result of $\beta = 1.55$ for purified HiPco SWNT-UPR.[20] The purified HiPco SWNT have a very broad chirality and diameter distribution but no appreciable non-SWNT carbon. These results may suggest better nanomaterial-polymer interaction in the case of the SouthWest Nanotechnology SWNTs. For SWNT-PMMA melts, Du et al found an even lower value of $\beta = 0.70$ (0.92 when converted to volume percent by Filippone and de Luna).[108,159] Together these findings show that even though nanotubes are strongly attracted to each other, a range of SWNT-polymer attractions can be achieved even in the absence of intentional functionalization.

Nonetheless, the similar values of β obtained for the SWNT indicate a similar type of attraction and network structure. Making the proportionality an equality ($G'_o = A\,(\phi - \phi_c)^{\beta}$) and calculating the proportionality constant enables comparison of the relative nanotube-nanotube attraction in each system. As shown by Prasad et al in their study of model colloid systems, higher values of A indicate greater interparticle attraction.[160] From Figure 4.13 (e, f), the A values for CG200, CG300, SG65 and SG65i were 3300, 6470, 1780 and 5920, respectively; these differences in attraction results in the differences in viscoelastic properties. It is hypothesized that the presence of higher non-SWNT carbon lowered the total attractive potential in the SG65 (and to a lesser extent in CG200) by non-SWNT carbon having lower interparticle attractions with each other and by mitigating SWNT-SWNT attraction by disrupting SWNT packing.

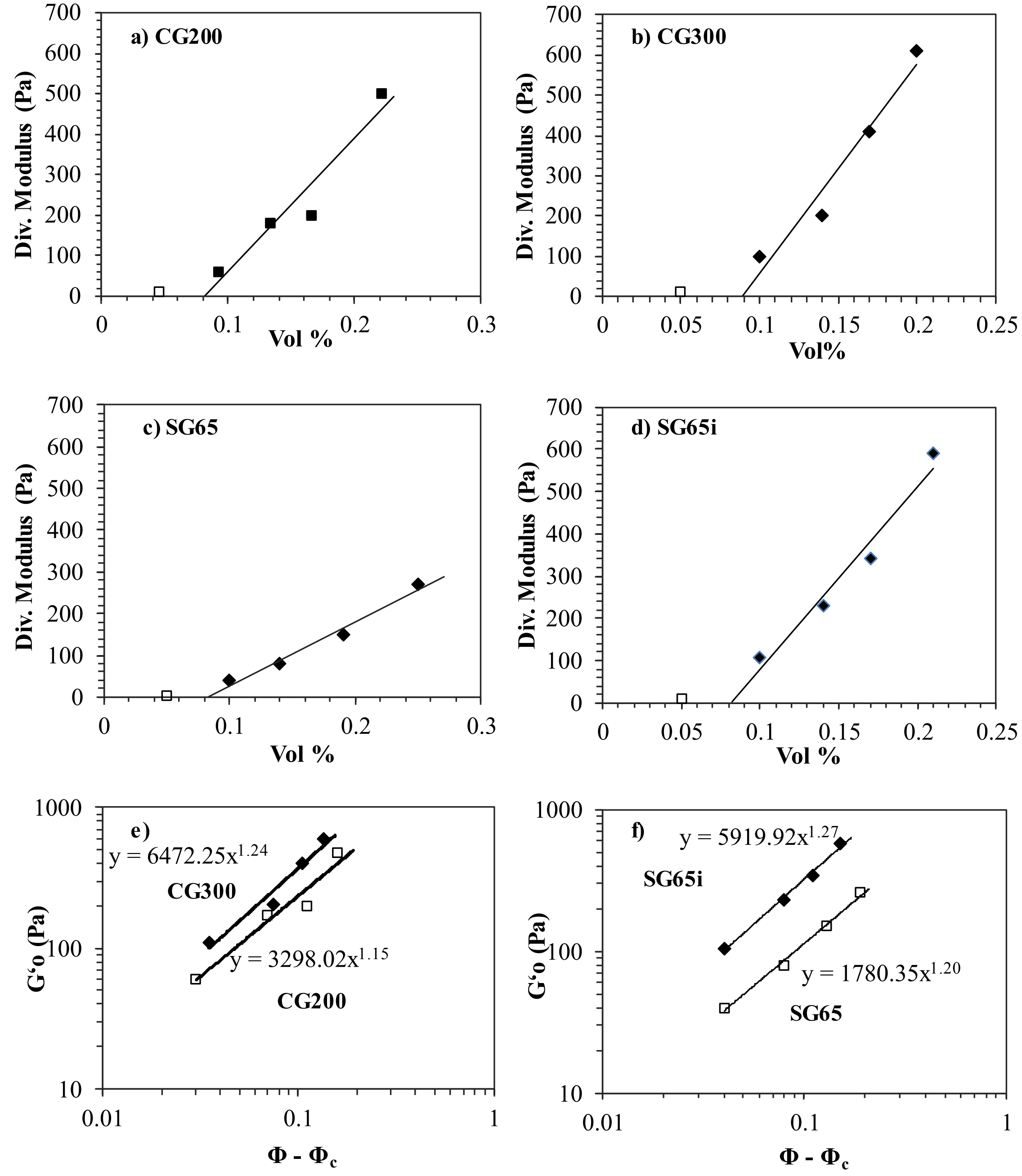

Figure 4.13 Divergence modulus vs concentration for (a) CG200, (b) CG300, (c) SG65 and (d) SG65i; Scaling relation $G'_o \propto (\phi - \phi_c)^{\beta}$ for (e) CG200 and CG300, (f) SG65 and SG65i. (from the figure $y = G'_o$ and $x = \phi - \phi_c$).

Following the work of Khalkhal et al, and Urena-Benavidas et al for MWNT-epoxy and MWNT-UPR,[147,152] the fractal dimensions comprising the network were calculated from scaling relations of low frequency plateau modulus and critical strain using methods developed by Shih et al and Wu and Morbidelli.[161,162] The equations for the scaling relations are the following:

$$G' \propto \phi^{\frac{B}{d-d_f}} \tag{4.1}$$

$$\gamma_c \propto \phi^{\frac{d-B-1}{d-d_f}} \tag{4.2}$$

where d_f is the fractal dimension and d is the system dimensionality.[147,152] The value of d_f can be calculated by equating the exponents of the two scaling relations. According to Wu and Morbidelli, $B = (d - 2) + (2 + x)(1 - \alpha)$, where $1 \leq x \leq 1.3$ is the backbone fractal dimension, $d = 3$ for a three dimensional network, and α ranges from 0 to 1 and defines the inter-floc and intra-floc strength.[152,162] For $\alpha = 0$, the inter-floc links are stronger intra-floc links, while for $\alpha = 1$ the intra-floc strength dominates.[162] For rigid aggregates, the interaction potential of particle is non-central and $m = 1/B$ and is estimated as being between 0.23 and 0.29.[152] For soft aggregates (or flocs) the interaction is central and depends on the distance between particle centers, and the internal structure does not respond elastically to small deformations. In this case, m is approximately 0.4 to 0.5.[112] It should be noted that while this method can provide a wealth of information about dispersion microstructure, the results are strongly dependent on the choice of the critical strain γ_c. Underestimating γ_c can lead to non-physical negative values of the fractal dimension d_f. Direct quantitative comparisons should only be done for systems where the same criteria were used to determine γ_c. In this work, γ_c represents the strain at which G'

decreased by 2% during the amplitude sweep; the corresponding results are shown in Table 4.9.

Table 4.9 Fractal properties for the four SWNT types

SWNT type	$B/(d-d_f)$	$(d-B-1)/(d-d_f)$	d_f	B	m	α
CG200	2.26	-1.060	1.33	3.77	0.26	0.08 - 0.16
CG300	2.48	-0.948	1.69	3.25	0.31	0.25 - 0.32
SG65	2.18	-0.702	1.65	2.94	0.34	0.35 - 0.42
SG65i	2.28	-0.956	1.48	3.27	0.29	0.24 - 0.31

Fractal dimensions of $1.7 < d_f < 1.8$ have been associated with fast aggregating systems while $2.0 < d_f < 2.2$ have been associated with slower aggregating flocs.[147] The d_f values observed for the SWNT types indicate faster aggregating systems; this was also observed for HiPCo SWNT-UPR and MWNT-UPR.[20,147] Intuitively, both the presence of non-SWNT carbon and diameter distribution would be expected to affect d_f. Impurities could both slow aggregation and disrupt uniform packing, similarly a more uniform diameter distribution might facilitate faster, tighter packing. However, the similarity of d_f for CG300 and SG65 suggest other factors such as the total amount of solids and size or impurities may be involved in microstructure formation. Similarly, CG300 and SG65 had the highest values of *m* indicating that they had the softest flocs; the *m* values for CG200 and SG65i were in the range considered characteristic of rigid flocs. For all the SWNT the values *m* were consistent with both inter- and intra- floc links contributing toward elasticity. Similar values were observed for SWNT (HiPCO)-UPR.[20,147] For CG200, intrafloc links were more dominant than for the other SWNT grades.

A final way to probe microstructural differences is through the relaxation dynamics. The shape of the G' versus ω curve and the crossover point ω_c where $G' = G'' = G_c$ are a reflection of the systems' relaxation modes.[159,163,164] Frequencies above the crossover frequency ω_c, probe the short-range dynamics of small length scales comparable to entanglement length. The microstructure of solid particles restrains polymer chain long range mobility and overall system shows slow relaxation. Therefore, below ω_c longer range dynamics are probed and $G' > G''$ due to the elastic behavior of the nanomaterial microstructure. With increasing concentration, the solid microstructure becomes more compact leading to which leads to a flattening on *G'* curve resulting from longer time scale relaxation. All SWNT-UPR dispersions showed a decrease in *G'* slope and increase in ω_c with increasing concentration. CG200, CG300 and SG65i consistently displayed higher ω_c ($tan\delta$ = 1) compared to SG65-UPR at similar SWNT concentration (Figure 4.12 and Table 4.10). This means the microstructure of CG200, CG300 and SG65i induces nanotube dominated relaxation dynamics at a lower concentration than SG65. This further supports differences in the microstructural physical interactions due to non-SWNT content. While there were differences between SG65 and other SWNTs in approaching solid dominated relaxation mode, none of the SWNT systems showed a second relaxation mode of the solid network at the lower limit of frequency as observed in the case of SWNT-PDMS dispersion characterized by Marceau et al.[163] Hassanabadi et al showed that CNT composite showed higher elasticity and slower relaxation dynamics than nanoclay in ethylene vinyl acetate; this was the result of a stronger network formed by higher inter-nanotube attraction and a higher degree of confinement of polymer by CNT network.[165] Similar premises can be drawn for the high purity SWNTs in UPR for the superior solid like behavior in comparison to SG65. We propose that the network strength can also be quantified based on the gel stiffness S using the $G'(\omega) = S\Gamma(1-n)\cos\frac{n\pi}{2}\omega^n$ relation developed by Mours and

Winter.[166] While *S* provides similar information as *G'(ω)*, characterizing dispersions in terms of a single stiffness parameter is more intuitive. The stiffness parameter has been used for comparing chemically cross-linked gels and physical gels of rod-like virus particle suspensions.[166-168] We are proposing this parameter could also be used to characterize stiffness of systems in the vicinity of percolation. Based on the stiffness factor values shown in Table 4.10, the robustness of network is similar for CG300 and SG65i and decrease with increasing non-SWNT carbon content and highlights how the higher attractive forces in the high purity dispersions affect viscoelasticity.

Table 4.10 Crossover frequencies and stiffness factors.

CG200			**CG300**		
Vol %	ω_c (rad/s)	S	Vol %	ω_c (rad/s)	S
0.09	10.0	94	0.10	15.8	150
0.13	25.1	250	0.14	25.1	280
0.17	39.8	290	0.17	39.8	550
0.22	99.8	670	0.20	63.0	820

SG65			**SG65i**		
Vol %	ω_c (rad/s)	S	Vol %	ω_c (rad/s)	S
0.10	2.51	65	0.10	15.8	140
0.14	10.0	110	0.14	25.1	295
0.19	15.8	210	0.17	39.8	474
0.25	25.1	340	0.21	63.0	760

4.5 Conclusion

It has long been recognized that differences between SWNT products and even batch to batch variation may cause differences in dispersion state and final composite properties. However, it has only recently been possible to systematically compare the effects of chirality distribution and purity. This work shows that in the case of dispersion in UPR, the presence of non-SWNT carbon has a much greater effect on viscoelasticity and microstructure than the differences in chirality distribution between current commercial grades. It also provides a framework for comprehensive comparison of dispersions in terms of measured rheological properties, percolation threshold, nanomaterial-polymer interaction, flocculation kinetics, fractal dimensions, floc linkage strength, relaxation dynamics, and stiffness. The methodologies used in this portion of the research should be broadly applicable to understanding if chirality distribution affects the microstructure of dispersions in melts, other thermosets, and polymer solutions. The methodologies should also be broadly applicable to other dispersions exhibiting colloidal rod behavior including, but not limited to, future commercial nanotube grades. While on the one hand, there are ongoing efforts to produce even higher quality SWNT with narrower chirality distributions and higher purities, a growing number of researchers are exploring production of lower cost nanotubes from waste carbon sources. Therefore, tools for systematically comparing dispersion properties will be of increasing importance.

CHAPTER 5 EFFECT OF CNT TYPE AND FUNCTIONALIZATION ON VISCOELASTIC, CURING KINETICS AND CURED COMPOSITE PROPERTIES

The focus of this portion of the research was to understand the effect of carbon nanotube type and carbon nanotube functionalization on cured composite properties. More specifically, this investigation was focused on how CNT dispersion state, prior to curing unsaturated polyester resin, varied with nanotube type and functionalization. The dispersion state and viscoelastic behavior characterization was followed by a curing behavior study using curing rheology and differential scanning calorimetry (DSC).

The lowest concentration at which a dispersed filler material in polymer matrix forms a bulk network is described as the rheological percolation concentration. At percolation, network formation results in a significant increase in viscoelastic properties and electrical conductivity, so percolation is desired for achieving better mechanical and electrical properties. Adding nanofillers above the percolation concentration can lead to unwanted aggregation resulting deterioration of mechanical properties and increases the cost of composite preparation. Thus, it is important to determine the percolation concentration and understand how CNT type and functionalization affects dispersion state and viscoelastic properties at percolation. However, network based dispersion relaxation dynamics, the origin of network based elastic behavior, and network-polymer interactions based on CNT type and functionalization have received limited investigation. Finally, it is essential to understand curing behavior at percolation since processing of cured composites requires knowledge of gelation time and the kinetics of curing process. Thus, the attributes of the

CNT-UPR dispersions on the curing process were investigated by DSC and curing rheology. Curing of CNT-UPR composites have been investigated less than epoxy systems, and to the author's knowledge this is the first curing kinetics study of CNT-UPR.

The initial qualitative comparisons of CNT dispersions in UPR were made by referring to optical microscopy images. Figure 5.1 shows dispersion images of CNT-UPR with varying CNT type, concentration and surface functionalization. With increasing CNT concentration, the dark areas of dispersed CNT increases and interstitial white areas of resin decrease. For MWNT dispersions, there were no visible aggregates while for SWNT dispersions aggregates, which increased with increase in concentration, were readily visible. At 0.20 vol % SWNT concentration, CG200 and CG200SAN dispersions showed similar aggregation. An optically better dispersion state, with lower aggregation and size, was observed for 0.20 vol % CG200PS and 0.20 vol % Tuball. The Tuball dispersion showed the least amount of aggregation.

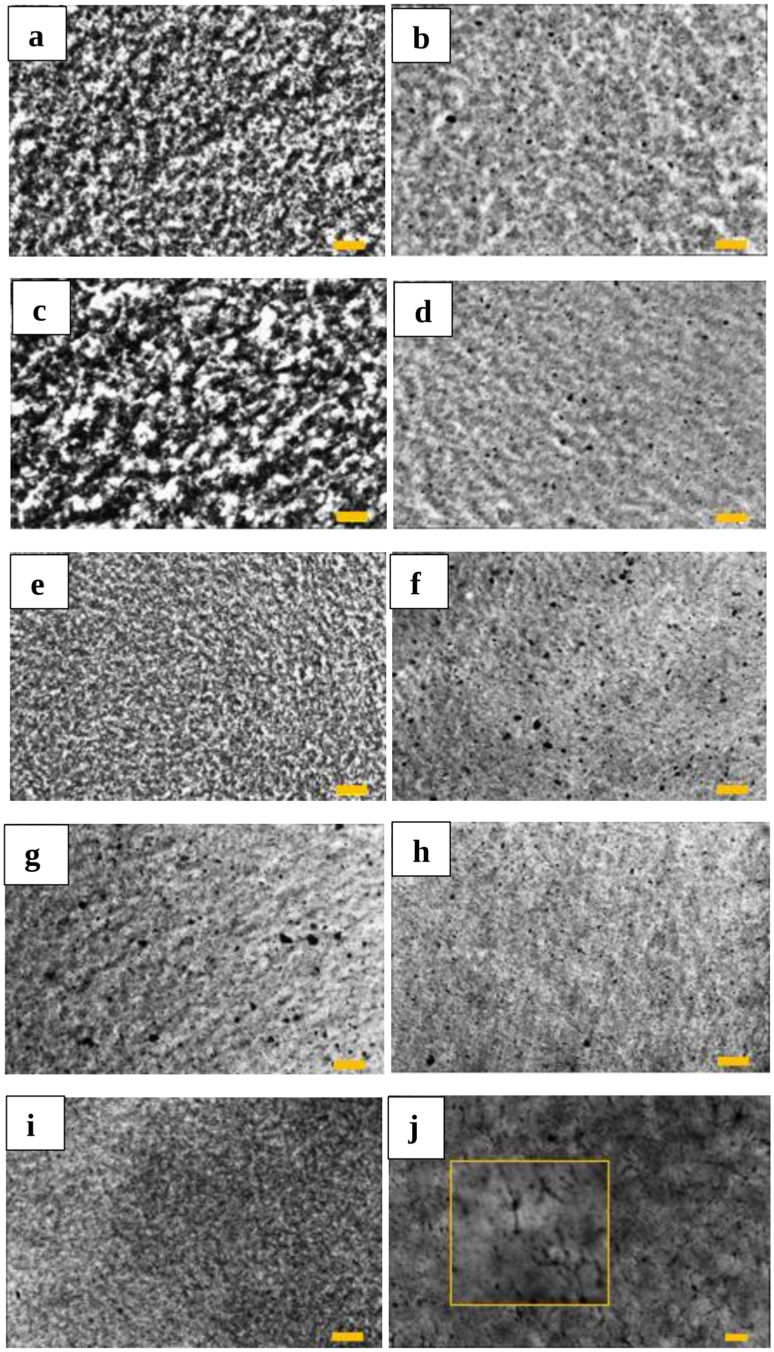

Figure 5.1 Optical microscope images of CNT-UPR dispersions under 20X objective and stitched over an area of 2.53 mm x 1.68 mm; Scale bar 200 μm. (a) 0.10 vol% MWNT (b) 0.10 vol% CG200 (c) 0.15 vol% MWNT (d) 0.15 vol% CG200 (e) 0.20 vol% MWNT (f) 0.20 vol% CG200 (g) 0.20 vol% CG200SAN (h) 0.20 vol% CG200PS (i) 0.20 vol% Tuball; (j) 0.20 vol% Tuball (40X stitched over an area of 0.96 x 0.64 mm, scale bar 50 μm; inset shows fiber type structures)

5.1 Viscoelastic Behavior of CNT-UPR

In order to quantitatively understand the dispersion state of CNT-UPR systems, the dispersions were probed by oscillatory rheology in the linear viscoelastic regime followed by steady shear rheology of flow behavior under ramping shear. Figure 5.2 shows the behavior of the dispersions under oscillatory shear at fixed frequency and increasing amplitude. The linear viscoelastic limit was determined by the critical strain γ_c at which plateau *G'* deviates by 5%. For unfunctionalized CG200 and MWNT, the linear viscoelastic strain limit decreased with increasing concentration. At 0.15 vol %, *G'* was greater than *G"* for CG200 in the linear viscoelastic regime, while for MWNT-UPR *G'* was lower than *G"* even at 0.20 vol %. Among the 0.20 vol % CNT dispersions, the lowest *G'* was observed for the MWNT dispersion, and MWNT had a higher γ_c than the SWNT systems. The CG200 dispersions had similar critical strain values which varied from 1.2 to 1.5 %. The 0.20 vol % Tuball dispersion exhibited the lowest critical strain, which was approximately ~ 4 times lower than CG200 dispersions. For the 0.20 vol % CG200 dispersions, the observed trend in *G'* was CG200 > CG200PS > CG200SAN and the trend for *G"* was CG200PS > CG200 > CG200SAN. The 0.20 vol % CG200PS dispersion had higher *G"* than *G'* over the linear regime, while *G'* was greater than *G"* for both 0.20 vol % CG200 and CG200SAN dispersions. The 0.20 vol % Tuball dispersion demostrated the greatest increase in the *G'* and *G"*, which is consistent with the better dispersibility observed by optical microscopy. The differences in viscoelastic behavior can be accounted for by the complex interplay between dispersibility and microstructure for the SWNT systems at similar volume fraction of true SWNT content. The storage modulus and critical strain values for the CNT dispersions are displayed in Table 5.1.

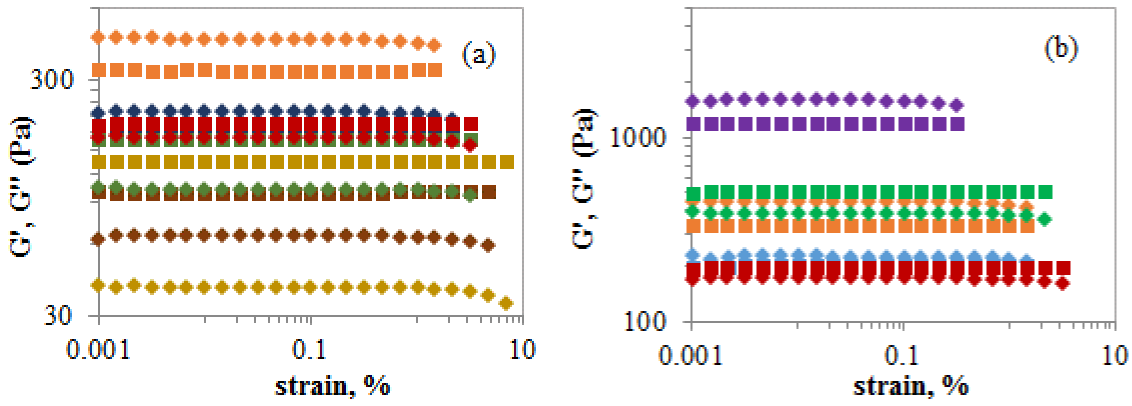

Figure 5.2 Oscillatory amplitude on CNT-UPR dispersions. (a) CG200: 0.20 vol% (♦, ■) 0.15 vol% (♦, ■), and 0.10 vol% (♦, ■); MWNT: 0.20 vol% (♦, ■), 0.15 vol% (♦, ■), and 0.10 vol% (♦, ■). (b) 0.20 vol% : Tuball (♦, ■), CG200 (♦, ■), CG200PS(♦, ■) , CG200SAN(♦, ■) and MWNT(♦, ■). G’(♦), G”(■).

Table 5.1 Linear viscoelastic regime amplitude sweep properties of CNT-UPR dispersions

Vol %	Sample	G' (Pa)	Critical Strain (%)
0.20	Tuball	1600	0.28
0.20	CG200	450	1.2
0.20	CG200PS	390	1.5
0.20	CG200SAN	230	1.3
0.20	MWNT	170	2.6
0.15	CG200	220	1.7
0.10	CG200	100	2.8
0.15	MWNT	65	3.3
0.10	MWNT	40	3.6

Following the determination of linear viscoelastic regime, the dispersions were subjected to an oscillatory frequency sweep at an amplitude below γ_c. The constant strain oscillatory frequency dependency of *G’*, *G”*, and *tanδ* of the unfunctionalized CG200 and MWNT dispersions at different concentrations are shown in Figure 5.3. Dispersions with increasing concentration of CG200 and MWNT showed increased moduli with concentration. The increase in *G'* with concentration was more prominent since *G'* mainly originates from the presence of CNT. The dependency of *G'* and *G"* at low frequency for CNT-UPR deviated from the terminal behavior ($G' \sim \omega^2, G'' \sim \omega$)[87] observed for polymeric systems even at the lowest concentration of 0.10 vol %.[87] The low frequency dependency of *G'* for MWNT decreased from $\omega^{0.19}$ to $\omega^{0.05}$ with an increase in concentration from 0.10 vol % to 0.20 vol %, while for a similar concentration increase in CG200 frequency exponent changed from $\omega^{0.095}$ to $\omega^{0.08}$. Moreover, for 10 rad/s to 100 rad/s, the *G'* frequency dependency with increasing concentration of CG200 decreased from $\omega^{0.45}$ to $\omega^{0.32}$, which was lower than the MWNT dispersions at same concentrations, $\omega^{0.62}$ to $\omega^{0.42}$. Similarly, the slope trend for G" at low and high frequencies showed lower power law exponents for CG200 than MWNT. Table 5.2 shows the high and low frequency slope dependence of moduli for all CNT-UPR dispersions. The formation of bulk network at percolation results in a rapid rise in elasticity and retards relaxation dynamics. The trends in *G'* slope, rise in *G'* values and $tan\delta$ approaching plateau at low frequency for SWNT dispersion indicate inception of percolation at $\phi_c \sim 0.15$ vol %, while for MWNT it was $0.15 < \phi_c < 0.20$ vol %. These criteria have also been applied to determine percolation determination in other studies.[14,20,156,165,168,169] Based on the estimated percolation concentration for CG200 and MWNT, 0.20 vol % should be near ϕ_c for the CNT dispersions. Therefore, 0.20 vol % was chosen as the basis for comparison.

Table 5.2 Frequency dependency of G’ and G” for CNT-UPR dispersions. Low ω (0.01 to 0.1 rad/s); High ω (6 to 100 rad/s)

Vol %	Sample	Slope G' low ω	Slope G' high ω	Slope G" low ω	Slope G" high ω
0.20	Tuball	0.13	0.33	0.11	0.66
0.20	CG200	0.08	0.32	0.11	0.69
0.20	CG200PS	0.09	0.43	0.21	0.77
0.20	CG200SAN	0.07	0.36	0.13	0.72
0.20	MWNT	0.05	0.42	0.18	0.74
0.15	CG200	0.08	0.33	0.12	0.69
0.10	CG200	0.10	0.45	0.27	0.81
0.15	MWNT	0.07	0.48	0.27	0.78
0.10	MWNT	0.19	0.62	0.53	0.87

The effect of CNT type and SWNT functionalization on viscoelastic properties have been compared in Figure 5.4 for 0.20 vol % concentration. The Tuball dispersion exhibited higher *G’* and *G”* over the entire frequency range compared to the other dispersions. The general trend in *G’* magnitude was: Tuball > CG200 > CG200PS > CG200SAN > MWNT; this trend is discussed later in this section. The moduli behavior for CG200PS showed interesting trends. The *G’* for CG200PS was similar to that of CG200 in the high frequency region (25 - 100 rad/s), but CG200PS had a lower G’ than CG200 at low frequency. *G”* for CG200PS was higher than the CG200 and CG200SAN dispersions between 0.6 to 100 rad/s. The CG200SAN and MWNT dispersions showed overlap of *G”* in the frequency range 6 – 100 rad/s. The *G’* showed near frequency independent behavior in the low frequency region (0.1 - 0.01 rad/s) for all dispersions as shown in Table 5.2. The high frequency power law dependence was similar for Tuball, CG200 and CG200SAN: $\omega^{0.33}$, $\omega^{0.32}$ and $\omega^{0.36}$, respectively. It was higher for CG200PS and MWNT, $\omega^{0.43}$ and $\omega^{0.42}$ respectively. High frequency power law dependence of $\omega^{0.50}$ is associated with Rouse type or short motion based relaxation behavior.[99,165,170] Comparing the power law dependences of the 0.20 vol % CNT dispersions to 0.10 vol % MWNT dispersion, shows that the short range dynamics were affected by the 0.20 vol % concentration. The effect was greatest for 0.20 vol % CG200, CG200SAN and Tuball, and less pronounced for CG200PS and MWNT. The crossover frequencies of the five dispersions at 0.20 vol % were also significantly different as shown in Table 5.3.

It is expected that with an increase in elasticity the crossover point ω_c will shift to higher frequencies, making solid-like behavior to persist to higher frequencies (shorter time scale).[19,20,88] For the dispersions in the percolation regime (0.20 vol%), Tuball and CG200 displayed the fastest approach to nanotube network controlled relaxation dynamics with crossover occurring at 26 and 22 rad/s respectively, followed by CG200SAN (12 rad/s), MWNT (7.5 rad/s) and CG200PS (5.0 rad/s). Interestingly, CG200PS had a higher G’ than CG200SAN and MWNT, but exhibited a lower frequency (longer time scale) transition to solid-like relaxation.

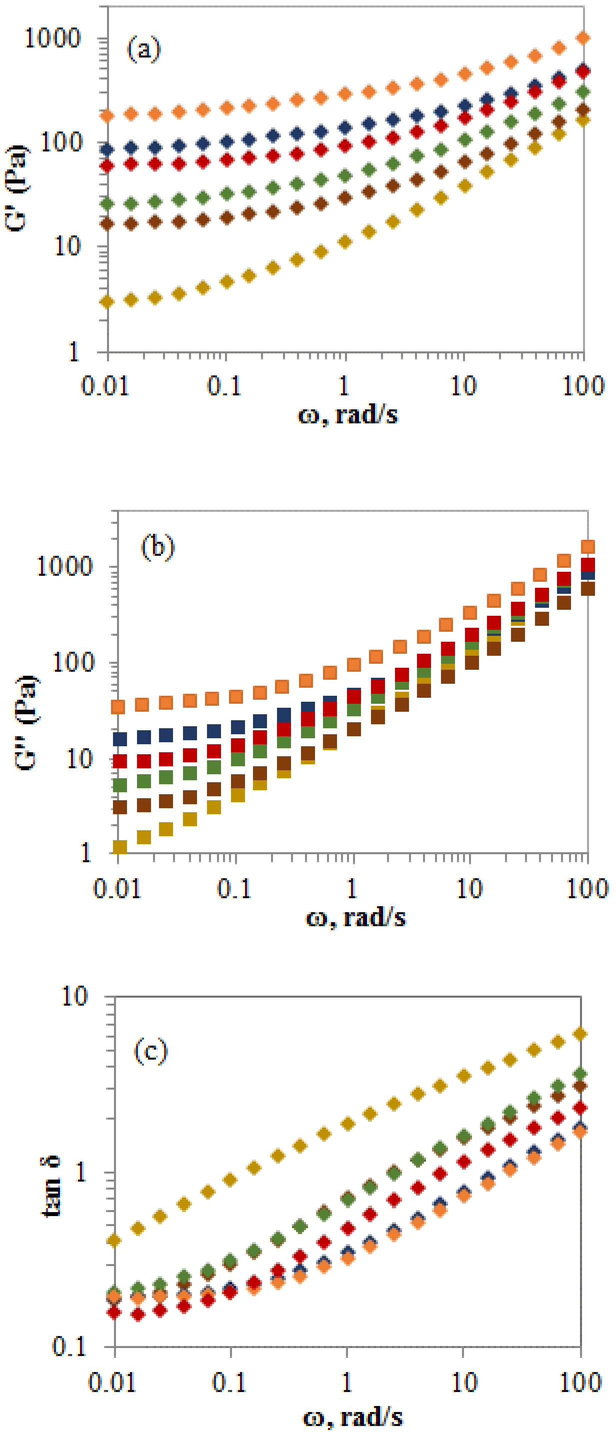

Figure 5.3 Frequency dependent oscillatory behavior of unfunctionalized SWNT (CG200) and MWNT. (a) G', (b) G" and (c) tanδ. CG200: 0.20 vol % (♦, ■) 0.15 vol % (♦, ■), and 0.10 vol % (♦, ■); MWNT: 0.20 vol % (♦, ■), 0.15 vol % (♦, ■), and 0.10 vol % (♦, ■). G'(♦), G"(■).

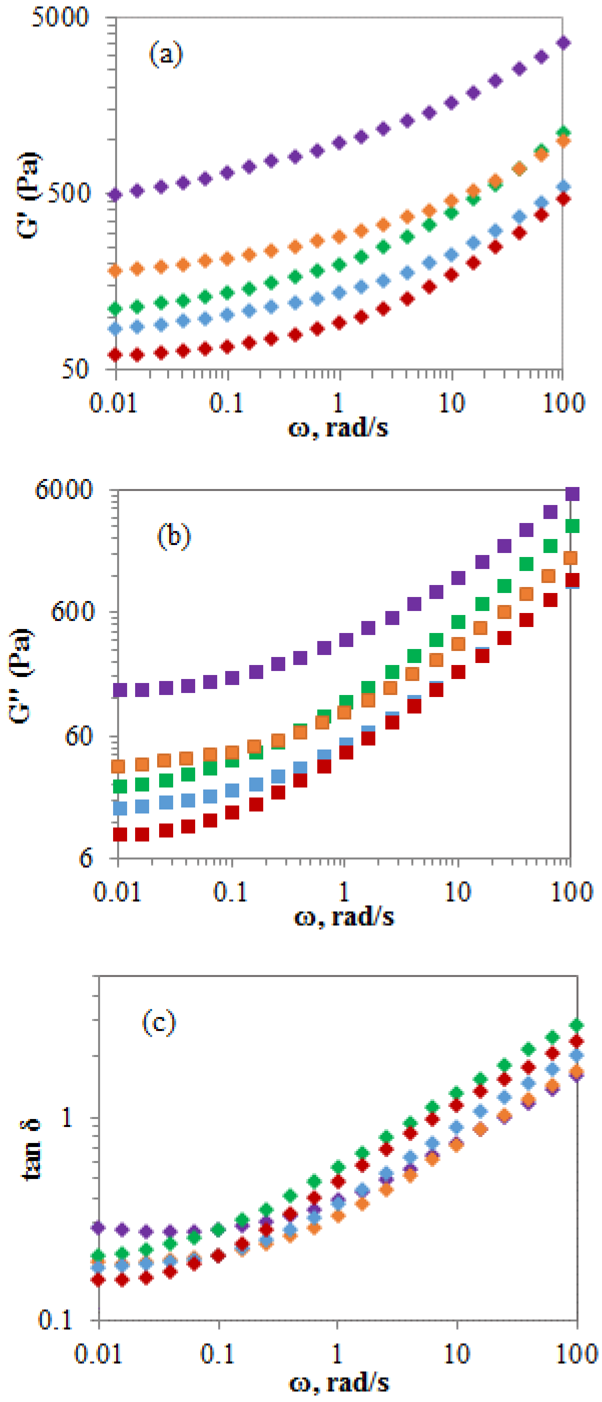

Figure 5.4 Frequency dependent oscillatory behavior of SWNT (CG200) and MWNT at 0.20 vol%. (a) G’, (b) G” and (c) tanδ. Tuball (♦, ■), CG200(♦, ■), CG200PS (♦, ■), CG200SAN (♦, ■) and MWNT(♦, ■). G’(♦), G”(■).

Table 5.3 Oscillatory rheology properties for 0.20 vol % CNT-UPR dispersions

Sample	ω_c (rad/s)	G_c (Pa)	G' (0.01 rad/s) (Pa)	tanδ (0.01 rad/s)
Tuball	26	2190	489	0.30
CG200	22	509	180	0.20
CG200PS	5.0	316	112	0.20
CG200SAN	13	246	86.9	0.18
MWNT	7.5	155	60.5	0.16

The dispersion state and microstructure development is directly related to nanofiller concentration, nanofiller-nanofiller and nanofiller-polymer interactions. Elastic behavior and relaxation dynamics are influenced by several factors affecting microstructure which include extent of nanofiller-polymer interface formation, nanofiller-polymer bridging of network, nanofiller based cluster network confining polymer mobility and nanofiller induced stress bearing mechanism which results from the nanofiller network dynamics.[164] Surface modification of nanotubes to achieve better dispersion state have sometimes shown an increase and sometimes shown a decrease in the elastic behavior. Zhang et al.[169] and Mitchell et al.[16] showed improved miscibility with carbon nanotube functionalization and significant enhancement of elastic moduli.[16,169] In other studies by White et al. and Urena-Benavides et al. the dispersions improved with functionalization, however the elastic moduli were lower than pristine carbon nanotubes.[19,97] The authors suggested suppression in CNT cluster formation by the presence of functional groups which reduced CNT attraction and thereby cluster network derived elastic behavior.[19,97] Similar points of view on clustering of nanoparticles enhancing elastic behavior have been proposed by other authors.[103,171,172] The differences in elastic and relaxation behavior observed in this research may be due to variabilities in the microstructure originating from nanotube-nanotube and nanotube polymer interactions. The pristine 0.20 vol % CG200 dispersion showed higher aggregation which is a reflection of increased nanotube-nanotube attraction which led to a greater extent of clustering or aggregation in the network. This resulted in the higher elastic moduli in the frequency sweep and a faster transition to network dominated relaxation (high crossover frequency) in comparison to the MWNT or other CG200 dispersions. At same concentration, CG200SAN showed similar aggregation which means non-covalent adsorption of SAN did not improve interaction with polymer matrix and thus dispersibility. The 0.20 vol % CG200SAN had a lower G' and crossover frequency, which could be an indication of weaker cluster formation due to adsorption of SAN on SWNT, decreasing nanotube-nanotube direct contact while increasing probability of SAN bridged network. Polymer bridged networking has been previously discussed by Pryamitsyn and Ganesan,[104] and Surve et al.[109] The higher aggregation observed for CG200 and CG200SAN supports the nanotube-nanotube clustering based evolution of elastic behavior. The least elastic behavior displayed by 0.20 vol % MWNT could be attributed to wall defects and lower degree of intertube attraction as suggested by Urena-Benavides et al.[19] At 0.20 vol % CNT, the oscillatory frequency sweeps showed CG200PS had higher G' and G'' than CG200SAN and MWNT, higher high frequency G'' than CG200, and a lower ω_c than MWNT and CG200 dispersions. CG200PS also had better dispersion than CG200 and CG200SAN optically. Based on the frequency sweep results and optical dispersion state, it could be assumed that the polystyrene oligomer chains covalently attached to SWNT in CG200PS could induce better interfacial interaction with aromatic groups UPR than longer polymer chains of SAN. Also with better UPR matrix interface and interaction, CG200PS is expected to have greater hindrance on polymer mobility, and this effect was evidenced from increased *G”* for CG200PS in the high frequency regime than MWNT, CG200SAN and CG200 dispersions, and greater *G’* than MWNT and CG200SAN. The CG200PS had lower nanotube-nanotube clustering due to presence of functional groups which led to lower ω_c than CG200, CG200SAN and MWNT. In case of Tuball SWNT, the dispersibility was much better than CG200PS, which led to much greater elastic and viscous moduli enhancement. From the higher magnification inset image of Tuball dispersion in Figure 5.1, fine fiber-like structures are observed which could be non-SWNT carbon or fibrous aggregates of SWNT; the Tuball used in this study had an initial fibrous morphology. Aggregate morphology can also influence viscoelastic behavior and fibrous aggregates could provide better interfacial contact with polymer than compact aggregates. Despite the higher *G’* and *G”* exhibited by Tuball, the ω_c was at a similar frequency for Tuball (26 rad/s) and CG200 (22 rad/s). This supports that the transition to solid-like behavior or nanotube dominated response is directly related to nanotube-nanotube aggregation and slows down on with the extent of polymer interfaced networking.

The effect of steady shear on the viscosity of 0.20 vol % CNT-UPR dispersions are shown in Figure 5.5. All dispersions exhibited shear thinning behavior (Figure 5.5 (a)) and the dispersion viscosities showed the following order: Tuball > CG200PS > CG200 > CG200SAN > MWNT. A notable feature from the flow curves has been enhancement in higher shear viscosities of the Tuball and CG200PS dispersions which may be related to the better dispersibility and polymer interaction observed for Tuball and CG200PS. The viscosity versus shear stress plots in Figure 5.5 (b) showed significant drop in viscosity at approximately constant stress for MWNT, CG200PS and Tuball at low shear stresses. In contrast, the CG200 and CG200SAN dispersions exhibited more shear stress dependent viscosity at low shear stress.

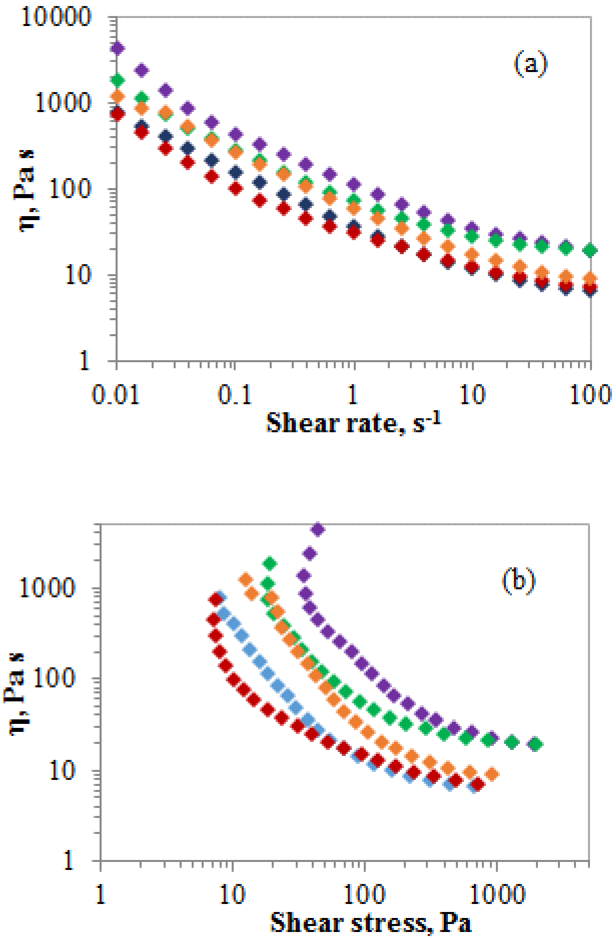

Figure 5.5 Steady shear rheology behavior of 0.2 vol% CNT-UPR dispersions. (a) Viscosity versus shear rate, (b) Viscosity versus shear stress. CG200 (♦, ■), CG200PS (♦, ■), CG200SAN (♦, ■), MWNT (♦, ■) and Pol31830 (♦, ■).

5.2 Curing Rheology of CNT-UPR

The change in viscoelastic behavior of 0.2 vol % CNT-UPR dispersions during curing are shown in Figure 5.6. A summary of curing rheology properties of CNT-UPR dispersions are displayed in Table 5.4. The *tanδ* plots in Figure 5.7 (a) display minima points which shift to longer times with incorporation of CNT. The G' and G'' plots in Figure 5.6 (b) display the increase in moduli during curing. The time at which the $tan\delta$ minima occurs is taken as the gel point time (t_{gel}). As shown in Figure 5.6 and Table 5.4, the gel point varied with CNT type and functionalization. An increase in gelation time was also observed for the incorporation of carbon nanofibers in UPR.[125] In the curing process, gelation involves the formation of chemical crosslinking in the bulk polymer, and gelation process is influenced by the presence of nanofiller and their dispersion state. The gelation times for SWNT dispersions were higher than both MWNT and neat UPR. The Tuball and CG200 dispersions had similar average gelation times considering the range of variability. The impact of different CNTs can be better understood from the elastic modulus developed at gelation (G'_{gel}). The Tuball dispersion had the greatest initial elastic modulus (G'_{co}) also exhibited the greatest G'_{gel}. Unfunctionalized CG200 had the greatest G'_{gel} among the CG200 dispersions. MWNT had a lower G'_{gel} than the SWNT dispersions but G'_{gel} was still much higher than neat UPR. The G'_{gel} for UPR evolved only from the covalent crosslinking from styrene and polyester chains and the increase in G'_{gel} was ~ 5 x 10^5 times of G'_{co}. Comparing the gelation elastic modulus of UPR with CNT-UPR, the extent of reinforcement by the nanotube network at gelation can be predicted. The higher G'_{gel} observed for Tuball is representative of increased elastic contribution of the Tuball nanotube physical network to the chemical crosslinked network at gelation; this further supports improved interfacial adhesion with the polymer matrix. Lower values of G'_{gel} can be interpreted as indicative of a weaker contribution of physical nanotube network at gelation. The gel point conversion (β_{gel}) was calculated by the following equation: $\beta_{gel} = \left(\left(G'_{gel} - G'_{co}\right)/\left(G'_{inf} - G'_{co}\right)\right)\times 100\%$, where G'_{co} is the elastic moduli at the start of curing and G'_{inf} is the elastic modulus at the end of curing. The β_{gel} shown in Table 5.4 decreased in the following order: Tuball > CG200 > CG200PS > CG200SAN > MWNT > UPR. Increased gelation conversions also showed a decrease in G'_{inf} values which can be interpreted as curing inhibition in the later stages. By comparing the G'_{gel} and G'_{inf} values of neat UPR and CNT-UPR, it could be suggested that though the presence of CNT network and increased $G'_{gel,}$ the presence of the CNT network decreased the extent of resin crosslinking. However, MWNT/PDMS crosslinking investigated by Romsanta et al. showed higher G'_{inf} than the neat polymer which was attributed to MWNT aggregates participating as physical entanglements.[90] Curing inhibition in carbon nanotube dispersed systems can occur from radical scavenging activity of nanotubes and physical barrier to polymer chain mobility and crosslinking.[173-175] Tuball and CG200PS having a higher G'_{inf} than CG200 could be due to lower aggregation observed in these systems which resulted in less polymer entrapment and a lower effect on the later stages of curing. In contrast, the higher G'_{inf} for CG200SAN could be associated with bulk SAN groups participating in the later stages of curing as physical crosslink sites.

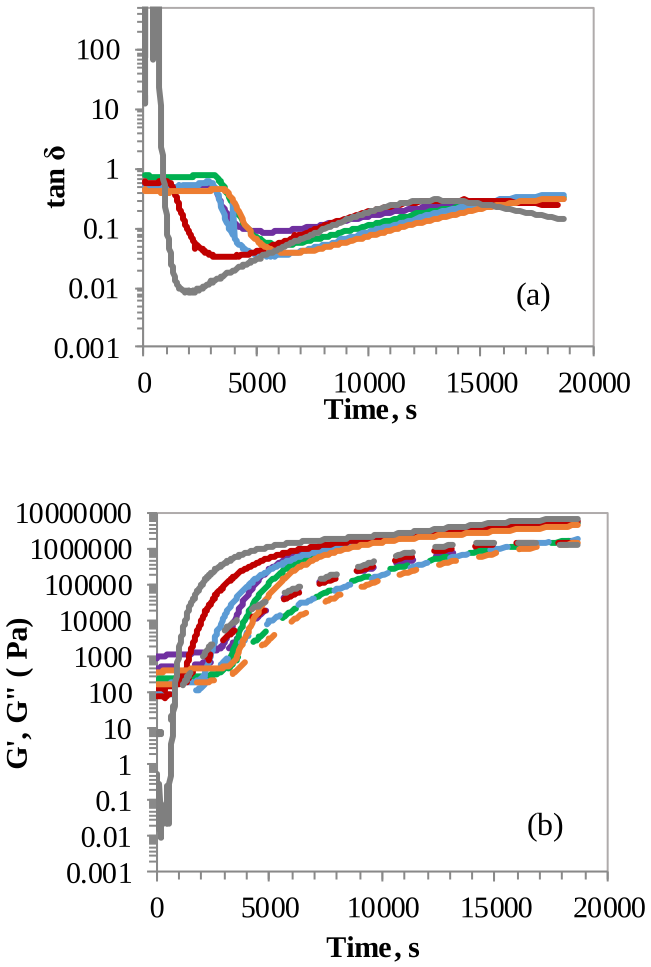

Figure 5.6 Variation of curing rheology viscoelastic properties with time of 0.2 vol% CNT-UPR. (a) tanδ, (b) G’, G”. Tuball (—), CG200 (—), CG200PS (—), CG200SAN (—), MWNT (—) and UPR (—). G’(—), G”(– –).

Table 5.4 Viscoelastic properties of curing rheology of 0.20 vol % CNT-UPR and neat UPR

Sample	G'$_{co}$ (Pa)	Avg. t$_{gel}$ (min)	G' gel (x 10^6 Pa)	(XG'$_{co}$)	β_{gel} (%)	G' $_{inf}$ (x 10^6 Pa)
Tuball	983	88 (±30)	0.28	280	5.2	5.36
CG200	357	104 (±10)	0.22	620	4.5	4.84
CG200PS	232	90 (±7.0)	0.18	800	3.5	5.26
CG200SAN	162	88 (±26)	0.18	1100	3.0	6.08
MWNT	132	57 (±6.0)	0.15	1100	2.2	6.71
UPR	0.16	32 (±6.0)	0.08	500000	1.0	7.43

5.3 Curing Kinetics Study by Differential Scanning Calorimetry

Results from the isothermal curing DSC studies 0.20 vol% CNT-UPR dispersions at 25°C are shown in Figure 5.7 and Table 5.5. The gelation time, degree of conversion and isothermal heat evolution were similar for MWNT and neat UPR. This indicates that MWNT incorporation had a negligible effect on the curing process. A number of studies have shown acceleration of curing in the presence of pristine and functionalized CNT. This has been attributed to functional group participation, degree of dispersibility and the superior thermal properties of CNTs. In case of the SWNT-UPR, a significant increase in peak heart evolution or gelation time was observed. The SWNT dispersions also exhibited lower total heat evolution (Q_{iso}) and lower conversions than MWNT or neat UPR for the isothermal curing. Among the SWNT dispersions, the Tuball exhibited lower gelation time and higher isothermal conversion while CG200PS displayed higher gelation time and lower isothermal conversion.

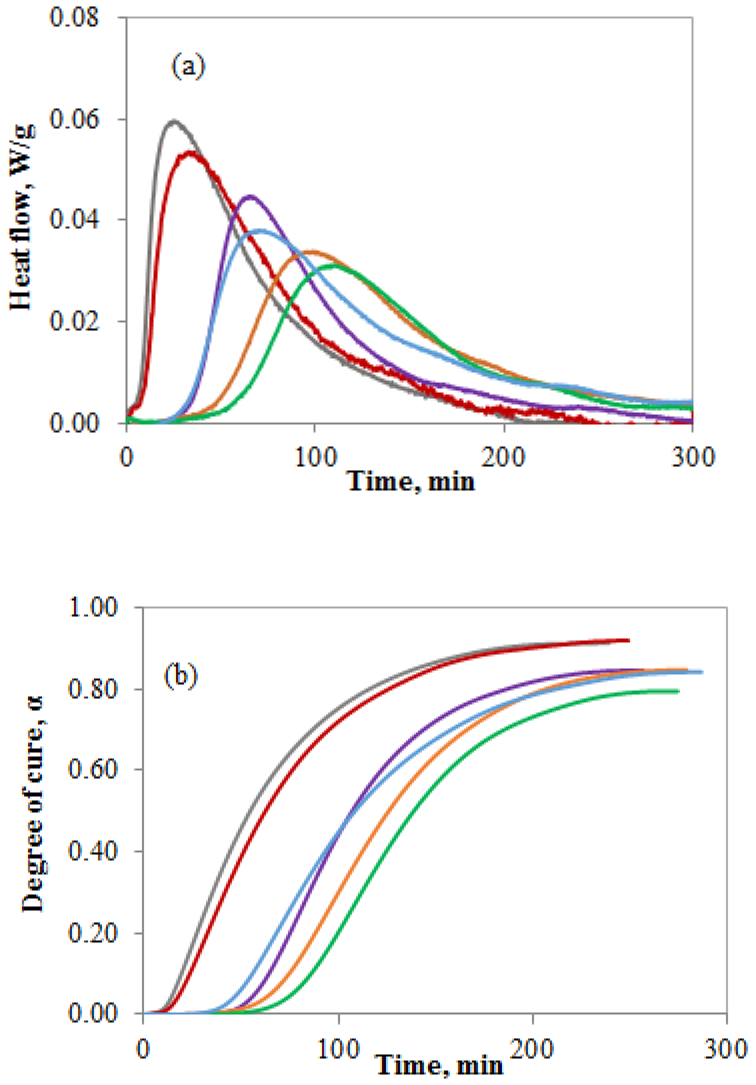

Figure 5.7 (a) Differential scanning calorimetry heat flow curve for isothermal curing at 25°C. (b) Isothermal conversion at 25˚C. Tuball (—), CG200 (—), CG200PS (—), CG200SAN (—), MWNT (—) and UPR (—).

Table 5.5 Conversion, gel times and isothermal heat evolution calculate from DSC at 25°C for 0.20 vol % CNT-UPR and neat UPR.

Sample	Conversion	Gel time, t_{gel} (min)	Isothermal total heat, Q_{iso} (J/g)
Tuball	87(±2.1)	67 (±15)	183 (±12)
CG200	83 (±1.4)	94 (±8.0)	188 (±9.0)
CG200PS	80 (±1.5)	108 (±16)	178 (±11)
CG200SAN	85 (±1.0)	73(±6.0)	217 (±6.0)
MWNT	91 (±0.7)	36 (±3.0)	255 (±5.0)
UPR	91 (±1.3)	31 (±7.0)	252 (±4.0)

Further insights on curing characteristics were obtained from the curing kinetics model fitting. The isothermal curing kinetics behavior of CNT-UPR was fitted to autocatalytic and diffusion limited models as shown in Figure 5.7. The model parameters are given in Table 5.6 and 5.7 respectively. The autocatalytic model generally displayed a better fit to the rate of conversion ($d\alpha/dt$) versus conversion (α) plots. The rate constant (k) obtained from the autocatalytical model showed similar values for CNT-UPR and neat UPR except for CG200SAN, where k was lower, and for Tuball where k was higher. The m-value representing the order of initiation stage was generally higher for CNT-UPR compared to neat UPR. Similarly, the n-values defining the order of the propagation reaction were comparable (except for CG200). The overall order ($m + n$) obtained using autocatalytical model was in the range 2.3 – 2.5. Previously, in the work by Abdalla et al.[176] an increase in the autocatalytic model m and n order parameters of functionalized MWNT-epoxy was observed. However, the opposite behavior (decrease in m and n) was observed for CNT filled rubber crosslinking by Sui et al[177]. In case of diffusion limited model fit, the rate constants were similar for MWNT-UPR and neat UPR. Lower rate constants were observed for SWNT dispersions except for Tuball-UPR which displayed a higher rate constant than neat UPR. The *k* values for the diffusion limited model were lower than the corresponding *k* values obtained from the autocatalytic model. The *m*-order parameter for the diffusion model had higher values for Tuball, CG200 and CG200PS than neat UPR. In contrast, the *n*-order was similar for neat UPR and MWNT-UPR but was significantly lower for SWNT dispersions. The overall order observed from diffusion model was 1.1 – 1.7. The diffusion limited model used for carbon nanofibers in UPR showed lower rate constants with incorporation of nanofibers and had an overall order of ~ 2.[125] Despite the autocatalytic model showing the better fit, the diffusion model is more representative of the complexities arising from the dispersion state and microstructure of nanotubes. This can be observed from the expected lowering of the reaction rate and inhibition at the propagation stage (lower *n*-values) and supports the observed values of gel time, isothermal heat evolved and degree of conversion. An interesting observation from the kinetic model fitting was the greater rate constant and greater *m*-value for Tuball even Tuball had a longer gelation time than neat UPR. This could be due to better conduction of evolved heat by Tuball SWNT across the polymer matrix after the initial start of curing.

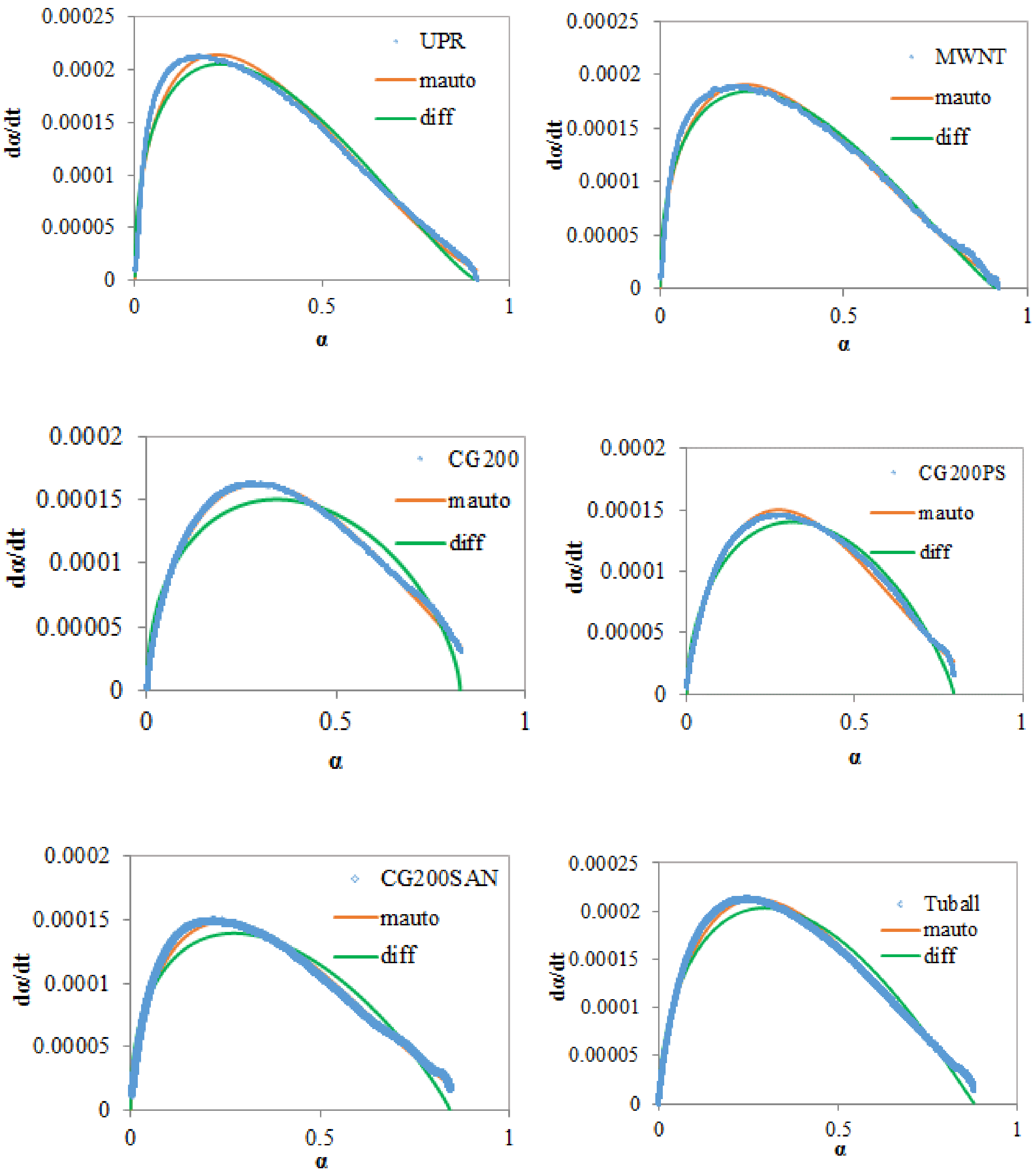

Figure 5. 8 Kinetic model fits on isothermal (25°C) experimental data for different samples. Modified autocatalytic model (mauto) and diffusion limited model (diff).

Table 5.6 Kinetic parameters for modified autocatalytic model for 0.20 vol % CNT-UPR and neat UPR: ${d\alpha}/{dt} = k\alpha^m(1-\alpha)^n$

Sample	k (x 10^{-4})	m	n
Tuball	8.8 (±1.1)	0.66(±0.03)	1.80 (±0.13)
CG200	6.1 (±0.36)	0.67 (±0.04)	1.55 (±0.1)
CG200PS	6.7 (±0.87)	0.72 (±0.05)	1.89 (±0.16)
CG200SAN	4.9 (±0.36)	0.55 (±0.02)	1.75 (±0.06)
MWNT	6.4(±0.33)	0.51 (±0.02)	1.72 (±0.07)
UPR	6.6(±0.55)	0.50 (±0.01)	1.76 (±0.1)

Table 5.7 Kinetic parameters for diffusion limited model for 0.20 vol % CNT-UPR and neat UPR: ${d\alpha}/{dt} = k\alpha^m(\alpha_{max}-\alpha)^n$

Sample	k (x 10^{-4})	m	n
Tuball	6.9 (±1.2)	0.53 (±0.01)	1.04 (±0.03)
CG200	3.9 (±0.38)	0.47 (±0.06)	0.67 (±0.13)
CG200PS	4.2 (±0.86)	0.51 (±0.03)	0.77 (±0.18)
CG200SAN	3.8 (±0.20)	0.42 (±0.01)	0.93 (±0.04)
MWNT	5.7 (±0.33)	0.44 (±0.02)	1.23 (±0.04)
UPR	5.8 (±0.34)	0.43 (±0.01)	1.25 (±0.01)

Comparing the rheology and DSC curing studies shows that, the trends observed with the DSC study in terms of gelation time, Q_{iso} and conversion were not observed in the curing rheology study. In terms of gelation times, UPR showed the same gelation time by the method while all other 0.20 vol % dispersions with the exception of CG200PS had lower gelation times as measured by DSC. The trend in average gelation time in increasing order for the dispersions were UPR < MWNT < Tuball < CG200SAN < CG200 < CG200PS for DSC and UPR < MWNT < CG200SAN, Tuball < CG200PS < CG200 for curing rheology. The variability in gelation times were generally similar for DSC and curing rheology. However, the Tuball and CG200PS for DSC and Tuball and CG200SAN for curing rheology had variations larger than other samples. These variabilities could result from experimental variations in processing the curing mixture (mixing the curing mixture, addition of reagents, loading time, etc).

5.4 Raman on Cured Composites

Carbon nanotubes exhibit unique Raman spectra. These features include the *G* band representing tangential vibrations of sp^2 hybridized C=C bond, *D*-band for tangential vibration defect sites (sp^3 hybridization, impurities, vacancies and loss of regularity), double scattering process denoted by *G'** band, and radial breathing modes only observed for SWNT and DWNT.[178] Raman scattering shifts have been associated with carbon nanotube surface modification, interaction with constituents in dispersed media, orientation, and external strain.[179,180] For carbon nanotubes dispersed in a polymer matrix, the polymer phase intercalating among CNT small bundles exerts pressure and compressive strain on the nanotubes which is reflected as peak shifts in the radial breathing modes, *G* band and *G'** band. A better dispersion state of nanotubes and enhanced polymer-nanotube interface can be detected by higher strain transfer resulting in a higher peak shift. A comparison of *G'** peak shifts of CNT and CNT-UPR cured composites are shown in Figure 5.9. The *G'** peak shifts are shown in Table 5.8 for two different laser irradiation 514 nm (primarily sensitive to metallic nanotubes) and 785 nm (primariliy sensitive to semiconducting nanotubes). Tuball SWNT exhibited the greatest *G'** shift for both lasers in the cured product, 5.9 cm^{-1} and 6.5 cm^{-1} for 514 nm and 785 nm lasers respectively. This further supports better dispersion state of Tuball with higher shifts imposed by higher degree of polymer interfacing. CG200 SWNT showed a noticeable shift of 4.5 cm^{-1} with the 785 nm laser while *G'** peak shift using 514 nm was not significant (~ 1 cm^{-1}). This observation could mean preferentially better dispersion of semiconducting nanotubes for CG200 in the pristine form. A similar behavior was exhibited by CG200SAN which displayed higher shift under 785 laser (2.9 cm^{-1}) than for 514 nm (1.6 cm^{-1}). In contrast, covalently functionalized CG200PS exhibited a *G'** shift of 3.5 cm^{-1} under 514 nm irradiation but no significant shift under 785 nm irradiation. Metallic nanotubes are more susceptible to Billups functionalization than semiconducting nanotubes so in funtionalized metallic tubes may have a preferentially better dispersion state and interaction with polymer matrix. Similar results were also seen for the CG200PS. For MWNT-UPR, no discernable peak was observed with 514 nm laser and peak could not be determined under 785 nm laser as it was broad and had low signal to noise ratio.

Table 5.8 Raman Peak shifts of *G'** under 514 nm and 785 nm lasers

Sample	G'* (514)	G'* (785)	Composite	G'* (514)	G'* (785)
CG200	2672.6 (± 1.6)	2584.3 (± 1.0)	CG200	2673.7 (± 0.3)	2588.8 (± 0.4)
CG200PS	2667.5 (± 1.6)	2585.0 (± 0.4)	CG200PS	2671.0 (± 0.3)	2585.1 (± 0.7)
CG200SAN	2669.3 (± 0.5)	2583.8 (± 1.1)	CG200SAN	2670.9 (± 0.6)	2586.7 (± 0.4)
Tuball	2678.8 (± 1.2)	2580.0 (± 0.8)	Tuball	2684.7 (± 1.5)	2586.5 (± 0.3)

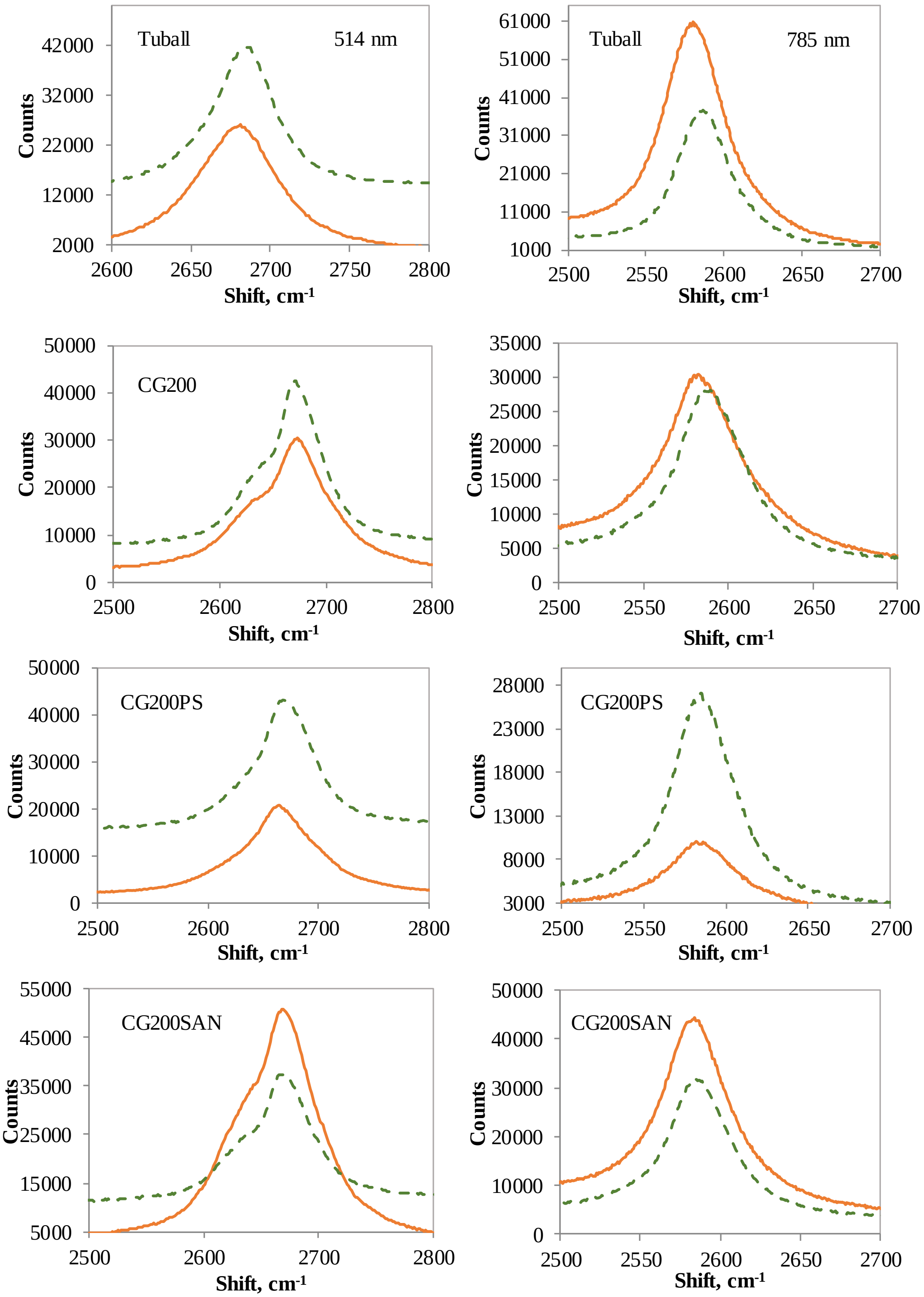

Figure 5.9 Raman band G'* shift comparison between CNT and cured CNT-UPR under 514 nm (left column) and 785 nm laser (right column). CNT (—), CNT-UPR cured composite (– –)

5.5 Conclusions

In this portion of the research, the viscoelastic properties and curing behavior of CNT-UPR dispersions at 0.20 vol % in the vicinity of percolation for different CNT types and functionalizations were investigated. Understanding percolation viscoelastic properties as well as curing kinetics is essential in optimizing composite properties. Tuball SWNT displayed a better dispersion state based on optical microscopy and the greatest viscoelastic moduli. It was found that with increase in viscoelasticity at similar CNT concentration (0.20 vol %) the curing process was hindered. This was based on the increase in gelation time, conversion and terminal elastic modulus of curing (G'_{inf}). Despite Tuball showing the greatest elastic behavior, it showed higher G'_{inf}, conversion, and similar or lower gelation time than CG200 and CG200PS. Interestingly, Tuball displayed a higher rate constant than UPR for DSC curing kinetics model fitting. Raman on cured composites also had showed Tuball had a better strain transfer to the polymer matrix. Although covalent functionalization of CG200 with styrene (CG200PS) showed improvement in dispersion state and MWNT showed similar conversion, gelation time and better G'_{inf} to that of neat UPR, Tuball's increased viscoelastic property and better interfacial adhesion to UPR matrix promises better composite properties. This investigation also delineated understanding of improved dispersion state by incorporation of lower priced carbon nanotubes and carbon nanotubes functionalized with polystyrene in UPR.

CHAPTER 6 CONCLUSIONS

This research used rheology to quantitatively understand dispersion state of commercial carbon nanotubes and surface modified nanotubes dispersed in UPR. The rheological characterization included concentration dependent viscoelasticity changes and determination of percolation onset. The study on viscoelastic properties above percolation was used to determine percolated network properties such as fractal characteristics and relative nanotube-nanotube versus nanotube-polymer interactions. By rheologically examining percolation network properties of four commercial SWNT products with controlled chirality and purity, the relative impact of chirality and impurity was clarified. It was shown that impurities had the dominant role in affecting microstructure in the dispersion. The impurities in the commercial SWNT resulted in the lowering of elastic behavior despite all SWNT products having similar affinity for the polymer matrix. Previous studies have focused on nanotube-nanotube attraction suppressing was discussed by intentional functionalization and improving affinity toward parent polymer matrices. However, the role of impurities in mitigating attraction among the nanotubes and affecting dispersion state has received limited attention. The results of this research will influence commercial carbon nanotube selection for composite preparation as commercial nanotubes are available at different prices, purities and chiralities.

Comparison of MWNT, CG200 SWNT, Tuball SWNT, and surface modified (covalent versus noncovalent) CG200SWNT showed that differing microstructure morphology, relative nanotube-nanotube and nanotube-polymer interaction leads to the origin of elastic behavior in percolated dispersions. Cluster units of nanotubes forming the percolated network with better polymer interfaces had the greatest enhancement in elastic behavior in comparison to cluster units with more cluster-cluster aggregation and weaker polymer interface. Curing rheology and DSC kinetics studies also showed higher gelation elastic moduli and higher rate constants for the unfunctionalized SWNT product (Tuball). It could be argued that the Tuball's high impurity content and fibrous morphology enabled it to disperse better than CG200 and functionalized CG200 in UPR. This suggests it may be possible to avoid expensive and time consuming functionalization schemes through careful selection of commercial nanotube products.

In this research, it was a challenge to make traditional dog bone or rectangular composite specimen with CNT concentration ~ 0.10 vol % and above, since the dispersions were highly viscous and thus difficult to process. This challenge was overcome by extruding curing mixtures inside cylindrical Teflon channel and curing the mixture inside. The cylindrical cured samples were subjected to tensile testing but there was a lack of consistency in the tensile testing as the cylindrical samples failed at the grips. The cured samples slipped at a lower grip pressure, while using a higher grip pressure resulted in deformation of the sample which led to the sample breaking inside the grip. So a challenge remains to develop an effective tensile test protocol for these soft cylindrical samples. Based on the results of the curing behavior observed by DSC and rheology, incorporation of carbon nanotubes, despite increasing the elastic and viscous modulus of the dispersion, inhibited curing which may deteriorate cured composite properties. Preliminary studies with DMA did not show improvement in the mechanical properties of the cured composites. Thus, additional work is required on optimizing the initial CNT-UPR viscoelasticity of the dispersion and the effects of CNT on curing is needed to produce easily processed composites that have better mechanical properties.

Overall, this work highlights the importance of nanotube selection for composite preparation as recent commercial product development are aimed at controlled chirality, purity and lower production cost of nanotubes. This work also demonstrated a comprehensive rheological characterization methodology which can be applied to assess several aspects of dispersion state of CNT-polymer systems in developing CNT-polymer composites. This work also provides a detailed framework for comparing the dispersion and properties of other cylindrical nanomaterial composites.

References

(1) Battisti, A.; Skordos, A. A.; Partridge, I. K.: Monitoring dispersion of carbon nanotubes in a thermosetting polyester resin. *Composites Science and Technology* **2009**, *69*, 1516-1520.

(2) Battisti, A.; Skordos, A. A.; Partridge, I. K.: Percolation threshold of carbon nanotubes filled unsaturated polyesters. *Composites Science and Technology* **2010**, *70*, 633-637.

(3) Seyhan, A. T.; Gojny, F. H.; Tanoğlu, M.; Schulte, K.: Critical aspects related to processing of carbon nanotube/unsaturated thermoset polyester nanocomposites. *European Polymer Journal* **2007**, *43*, 374-379.

(4) Seyhan, A. T.; Gojny, F. H.; Tanoğlu, M.; Schulte, K.: Rheological and dynamic-mechanical behavior of carbon nanotube/vinyl ester–polyester suspensions and their nanocomposites. *European Polymer Journal* **2007**, *43*, 2836-2847.

(5) Unsaturated Polyester Resin Market to Expand at CAGR of 7.5%, to Reach US$10.48 Billion by 2019. *Transparency Market Research*, 2016.

(6) North America Unsaturated Polyester Resin Market By Type, By Application, By Geography- Analysis & Forecast to 2020 PR Newswire, 2016.

(7) Berber, S.; Kwon, Y.-K.; Tománek, D.: Unusually high thermal conductivity of carbon nanotubes. *Physica Review Letters* **2000**, *84*.

(8) Dekker, C.: Carbon nanotubes as molecular quantum wires. *Physics Today* **1999**, *52*, 22-30.

(9) Salvetat, J.-P.; Bonard, J.-M.; Thomson, N. H.; Kulik, A. J.; Forró, L.; Benoit, W.; Zuppiroli, L.: Mechanical properties of carbon nanotubes. *Applied Physics A* **1999**, *69*.

(10) Wei, B. Q.; Vajtai, R.; Ajayan, P. M.: Reliability and current carrying capacity of carbon nanotubes. *Applied Physics Letters* **2001**, *79*.

(11) Li, N.; Huang, Y.; Du, F.; He, X.; Lin, X.; Gao, H.; Ma, Y.; Li, F.; Chen, Y.; Eklund, P. C.: Electromagnetic interference (emi) shielding of single-walled carbon nanotube epoxy composites. *Nano Letters* **2006**, *6*, 1141-1145.

(12) Sandler, J.; Shaffer, M.; Prasse, T.; Bauhofer, W.; Schulte, K.; Windle, A.: Development of a dispersion process for carbon nanotubes in an epoxy matrix and the resulting electrical properties. *Polymer* **1999**, *40*, 5967-5971.

(13) Girifalco, L. A.; Hodak, M.; Lee, R. S.: Carbon nanotubes, buckyballs, ropes, and a universal graphitic potential. *Physical Review B* **2000**, *62*, 13104-13110.

(14) Du, F.; Scogna, R. C.; Zhou, W.; Brand, S.; Fischer, J. E.; Winey, K. I.: Nanotube networks in polymer nanocomposites: rheology and electrical conductivity. *Macromolecules* **2004**, *37*, 9048-9055.

(15) Gojny, F. H.; Schulte, K.: Functionalisation effect on the thermo-mechanical behaviour of multi-wall carbon nanotube/epoxy-composites. *Composites Science and Technology* **2004**, *64*, 2303-2308.

(16) Mitchell, C. A.; Bahr, J. L.; Arepalli, S.; Tour, J. M.; Krishnamoorti, R.: Dispersion of functionalized carbon nanotubes in polystyrene. *Macromolecules* **2002**, *35*, 8825-8830.

(17) Thostenson, E. T.; Chou, T.-W.: Processing-structure-multi-functional property relationship in carbon nanotube/epoxy composites. *Carbon* **2006**, *44*, 3022-3029.

(18) Tang, W.; Santare, M. H.; Advani, S. G.: Melt processing and mechanical property characterization of multi-walled carbon nanotube/high density polyethylene (MWNT/HDPE) composite films. *Carbon* **2003**, *41*, 2779-2785.

(19) Ureña-Benavides, E. E.; Kayatin, M. J.; Davis, V. A.: Dispersion and rheology of multiwalled carbon nanotubes in unsaturated polyester resin. *Macromolecules* **2013**, *46*, 1642-1650.

(20) Kayatin, M. J.; Davis, V. A.: Viscoelasticity and shear stability of single-walled carbon nanotube/unsaturated polyester resin dispersions. *Macromolecules* **2009**, *42*, 6624-6632.

(21) Iijima, S.: Helical microtubules of graphitic carbon. *Nature* **1991**, *354*, 56-58.

(22) Bethune, D.; Klang, C.; De Vries, M.; Gorman, G.; Savoy, R.; Vazquez, J.; Beyers, R.: Cobalt-catalysed growth of carbon nanotubes with single-atomic-layer walls. *Nature* **1993**, *365*, 605 - 607.

(23) Iijima, S.; Ichihashi, T.: Single-shell carbon nanotubes of 1-nm diameter. *Nature* **1993**, *363*, 603 - 605.

(24) Reibold, M.; Paufler, P.; Levin, A.; Kochmann, W.; Pätzke, N.; Meyer, D.: Materials: Carbon nanotubes in an ancient Damascus sabre. *Nature* **2006**, *444*, 286-286.

(25) Baughman, R. H.; Cui, C.; Zakhidov, A. A.; Iqbal, Z.; Barisci, J. N.; Spinks, G. M.; Wallace, G. G.; Mazzoldi, A.; Rossi, D. D.; Rinzler, A. G.; Jaschinski, O.; Roth, S.; Kertesz, M.: Carbon Nanotube Actuators. *Science* **1999**, *284*.

(26) Besteman, K.; Lee, J.-O.; Wiertz, F. G. M.; Heering, H. A.; Dekker, C.: Enzyme-coated carbon nanotubes as single-molecule biosensors. *Nano Letters* **2003**, *3*.

(27) Kam, N. W. S.; O’Connell, M.; Wisdom, J. A.; Dai, H.: Carbon nanotubes as multifunctional biological transporters and near-infrared agents for selective cancer cell destruction. *Proceedings of the National Academy of Sciences* **2005**, *122*.

(28) Reddy, A. L. M.; Shaijumon, M. M.; Gowda, S. R.; Ajayan, P. M.: Coaxial mno2/carbon nanotube array electrodes for high-performance lithium batteries. *Nano Letters* **2009**, *9*.

(29) Rowell, M. W.; Topinka, M. A.; McGeheea, M. D.; Prall, H.-J.; Dennler, G.; Sariciftci, N. S.; Hu, L.; Gruner, G.: Organic solar cells with carbon nanotube network electrodes. *Applied Physics Letters* **2006**, *88*.

(30) Tans, S. J.; Verschueren, A. R. M.; Dekker, C.: Room-temperature transistor based on a single carbon nanotube. *Nature* **1998**, *393*.

(31) Gojny, F.; Wichmann, M.; Köpke, U.; Fiedler, B.; Schulte, K.: Carbon nanotube-reinforced epoxy-composites: enhanced stiffness and fracture toughness at low nanotube content. *Composites Science and Technology* **2004**, *64*, 2363-2371.

(32) De Volder, M. F.; Tawfick, S. H.; Baughman, R. H.; Hart, A. J.: Carbon nanotubes: present and future commercial applications. *Science* **2013**, *339*, 535-539.

(33) Thayer, A. M.: Carbon nanotubes by the metric ton. *Chemical & Engineering News* **2007**, *85*, 29-35.

(34) Ajayan, P. M.; Zhou, O. Z.: Applications of carbon nanotubes. In *Carbon Nanotubes*; Dresselhaus, M. S., Dresselhaus, G., Avouri, P., Eds.; Springer Berlin Heidelberg, 2001; pp 391-425.

(35) Baughman, R. H.; Zakhidov, A. A.; de Heer, W. A.: Carbon nanotubes--the route toward applications. *Science* **2002**, *297*.

(36) Calvert, P.: A recipe for strength. *Nature* **1999**, *399*.

(37) Saito, R.; Dresselhaus, G.; Dresselhaus, M. S.: *Physical Properties of Carbon Nanotubes*; Imperial College Press, 1998.

(38) Wildo¨er, J. W. G.; Venema, L. C.; Rinzler, A. G.; Smalley, R. E.; Dekker, C.: Electronic structure of atomically resolved carbon nanotubes. *Nature* **1998**, *391*.

(39) Hersam, M. C.: Progress towards monodisperse single-walled carbon nanotubes. *Nature Nanotechnology* **2008**, *3*, 387-394.

(40) Terrones, M.: Science and technology of the twenty-first century: synthesis, properties, and applications of carbon nanotubes. *Annual Review of Materials Research* **2003**, *33*, 419-501.

(41) Ouyang, M.; Huang, J.-L.; Lieber, C. M.: Fundamental electronic properties and applications of single-walled carbon nanotubes. *Accounts of Chemical Research* **2002**, *35*, 1018-1025.

(42) Dresselhaus, M. S.; Dresselhaus, G.; Hofmann, M.: The big picture of Raman scattering in carbon nanotubes. *Vibrational Spectroscopy* **2007**, *45*, 71–81.

(43) Dresselhaus, M. S.; Dresselhaus, G.; Jorio, A.; Filho, A. G. S.; Pimenta, M. A.; Saito, R.: Single nanotube raman spectroscopy. *Accounts of Chemical Research* **2002**, *35*.

(44) Krishnan, A.; Dujardin, E.; Ebbesen, T. W.; Yianilos, P. N.; Treacy, M. M. J.: Young’s modulus of single-walled nanotubes. *Physical Review B* **1998**, *58*.

(45) Li, F.; Cheng, H. M.; Bai, S.; Su, G.; Dresselhaus, M. S.: Tensile strength of single-walled carbon nanotubes directly measured from their macroscopic ropes. *Applied Physics Letters* **2000**, *77*.

(46) Treacy, M. M. J.; Ebbesen, T. W.; Gibson, J. M.: Exceptionally high Young's modulus observed for individual carbon nanotubes. *Nature* **1996**, *381*, 678 - 680.

(47) Yu, M.-F.; Lourie, O.; Dyer, M. J.; Moloni, K.; Kelly, T. F.; Ruoff, R. S.: Strength and breaking mechanism of multiwalled carbon nanotubes under tensile load. *Science* **2000**, *287*.

(48) Lu, J. P.: Elastic properties of carbon nanotubes and nanoropes. *Physica Review Letters* **1997**, *79*.

(49) Li, C.; Chou, T.-W.: A structural mechanics approach for the analysis of carbon nanotubes. *International Journal of Solids and Structures* **2003**, *40*.

(50) Yao, Z.; Kane, C. L.; Dekker, C.: High-Field Electrical Transport in Single-Wall Carbon Nanotubes. *Physica Review Letters* **2000**, *84*.

(51) Hone, J.; Llaguno, M. C.; Nemes, N. M.; Johnson, A. T.; Fischer, J. E.; Walters, D. A.; Casavant, M. J.; Schmidt, J.; Smalley, R. E.: Electrical and thermal transport properties of magnetically aligned single wall carbon nanotube films. *Applied Physics Letters* **2000**, *77*.

(52) Farhat, S.; Chapelle, M. L. d. L.; Loiseau, A.; Scott, C. D.; Lefrant, S.: Diameter control of single-walled carbon nanotubes using argon–helium mixture gases. *Journal of Chemical Physics* **2001**, *115*.

(53) J. Njuguna, K. P.: Polymer nanocomposites for aerospace applications: fabrication. *Advanced Engineering Materials* **2004**, *6*, 193–203.

(54) Mann, D.: Synthesis of carbon nanotubes. In *Carbon Nanotubes Properties and Applications*; O’Connell, M. J., Ed.; Taylor & Francis Group, LLC, 2006.

(55) Waldorff, E. I.; Waas, A. M.; Friedmann, P. P.; Keidar, M.: Characterization of carbon nanotubes produced by arc discharge: Effect of the background pressure. *Journal of Applied Physics* **2004**, *95*.

(56) Journet, C.; Maser, W. K.; Bernier, P.; Loiseau, A.; Chapelle, M. L. l.; Lefrant, S.; Deniard, P.; Fischerk, R. L. J. E.: Large-scale production of single-walled carbon nanotubes by the electric-arc technique. *Nature* **1997**, *388*.

(57) Guo, T.; Nikolaev, P.; Thess, A.; Colbert, D. T.; Smalley, R. E.: Catalytic growth of single-walled nanotubes by laser vaporization. *Chemical Physics Letters* **1995**, *243*, 49–54.

(58) Thess, A.; Lee, R.; Nikolaev, P.; Dai, H.; Petit, P.; Robert, J.; Xu, C.; Lee, Y. H.; Kim, S. G.; Rinzler, A. G.; Colbert, D. T.; Scuseria, G. E.; Tomanek, D.; Fischer, J. E.; E.Smalley, R.: Crystalline ropes of metallic carbon nanotubes. *Science* **1996**, *273*, 483-487.

(59) Dai, H.; Rinzler, A. G.; Nikolaev, P.; Thess, A.; Colbert, D. T.; Smalley, R. E.: Single-wall nanotubes produced by metal-catalyzed disproportionation of carbon monoxide. *Chemical Physics Letters* **1996**, *260*, 471-475.

(60) Li, W. Z.; Xie, S. S.; Qian, L. X.; Chang, B. H.; Zou, B. S.; Zhou, W. Y.; Zhao, R. A.; Wang, G.: Large-scale synthesis of aligned carbon nanotubes. *Science* **1996**, *274*, 1701-1703.

(61) Ren, Z. F.; Huang, Z. P.; Xu, J. W.; Wang, J. H.; P. Bush; Siegal, M. P.; Provencio, P. N.: Synthesis of large arrays of well-aligned carbon nanotubes on glass. *Science* **1998**, *282*, 1105-1107.

(62) Nikolaev, P.; Bronikowski, M. J.; Bradley, R. K.; Rohmund, F.; Colbert, D. T.; Smith, K. A.; Smalley, R. E.: Gas-phase catalytic growth of single-walled carbon nanotubes from carbon monoxide. *Chemical Physics Letters* **1999**, *313*, 91–97.

(63) Bronikowski, M. J.; Willis, P. A.; Colbert, D. T.; Smith, K. A.; E.Smalley, R.: Gas-phase production of carbon single-walled nanotubes from carbon monoxide via the HiPco process: A parametric study. *Journal of Vacuum Science and Technology A: Vacuum, Surfaces, and Films* **2001**, *19*.

(64) Bower, C.; Zhu, W.; Jin, S.; Zhou, O.: Plasma-induced alignment of carbon nanotubes. *Applied Physics Letters* **2000**, *77*, 830- 832.

(65) Wal, R. L. V.; Ticich, T. M.; Curtis, V. E.: Diffusion flame synthesis of single-walled carbon nanotubes. *Chemical Physics Letters* **2000**, *323*.

(66) Resasco, D. E.; Alvarez, W. E.; Pompeo, F.; Balzano, L.; Herrera, J. E.; Kitiyanan, B.; Borgna, A.: A scalable process for production of single-walled carbon nanotubes (swnts) by catalytic disproportionation of co on a solid catalyst. *Journal of Nanoparticle Research* **2004**, *4*.

(67) Hirsch, A.: Functionalization of single-walled carbon nanotubes. *Angewandte Chemie International Edition* **2002**, *41*, 1853-1859.

(68) Shaffer, M. S. P.; Fan, X.; Windle, A. H.: Dispersion and packing of carbon nanotubes. *Carbon* **1998**, *36*.

(69) Hilding, J.; Grulke, E. A.; Zhang, Z. G.; Lockwood, F.: Dispersion of carbon nanotubes in liquids. *Journal Of Dispersion Science And Technology* **2003**, *24*.

(70) Davis, V. A.; Ericson, L. M.; Parra-Vasquez, A. N. G.; Fan, H.; Wang, Y.; Prieto, V.; Longoria, J. A.; Ramesh, S.; Saini, R. K.; Kittrell, C.: Phase behavior and rheology of SWNTs in superacids. *Macromolecules* **2004**, *37*, 154-160.

(71) Davis, V. A.; Parra-Vasquez, A. N. G.; Green, M. J.; Rai, P. K.; Behabtu, N.; Prieto, V.; Booker, R. D.; Schmidt, J.; Kesselman, E.; Zhou, W.: True solutions of single-walled carbon nanotubes for assembly into macroscopic materials. *Nature Nanotechnology* **2009**, *4*, 830-834.

(72) Fiedler, B.; Gojny, F. H.; Malte H.G. Wichmann; Nolte, M. C. M.; Schulte, K.: Fundamental aspects of nano-reinforced composites. *Composites Science and Technology* **2006**, *66*, 3115–3125.

(73) Ma, P.-C.; Siddiqui, N. A.; Marom, G.; Kim, J.-K.: Dispersion and functionalization of carbon nanotubes for polymer-based nanocomposites: a review. *Composites Part A: Applied Science and Manufacturing* **2010**, *41*, 1345-1367.

(74) O'Connell, M. J.; Bachilo, S. M.; Huffman, C. B.; Moore, V. C.; Strano, M. S.; Haroz, E. H.; Rialon, K. L.; Boul, P. J.; Noon, W. H.; Kittrell, C.; Ma, J.; Hauge, R. H.; Weisman, R. B.; Smalley, R. E.: Band gap fluorescence from individual single-walled carbon nanotubes. *Science* **2002**, *297*, 593-596.

(75) Moore, V. C.; Strano, M. S.; Haroz, E. H.; Hauge, R. H.; Smalley, R. E.; Schmidt, J.; Talmon, Y.: Individually suspended single-walled carbon nanotubes in various surfactants. *Nano Letters* **2003**, *3*, 1379-1382.

(76) Nepal, D.; Geckeler, K. E.: Proteins and carbon nanotubes: close encounter in water. *Small* **2007**, *3*, 1259-1265.

(77) Zheng, M.; Jagota, A.; Semke, E. D.; Diner, B. A.; McLean, R. S.; Lustig, S. R.; Richardson, R. E.; Tassi, N. G.: DNA-assisted dispersion and separation of carbon nanotubes. *Nature Materials* **2003**, *2*, 338-342.

(78) O'Connell, M. J.; Boul, P.; Ericson, L. M.; Huffman, C.; Wang, Y.; Haroz, E.; Kuper, C.; Tour, J.; Ausman, K. D.; Smalley, R. E.: Reversible water-solubilization of single-walled carbon nanotubes by polymer wrapping. *Chemical Physics Letters* **2001**, *342*, 265-271.

(79) Nakashima, N.; Tomonari, Y.; Murakami, H.: Water-soluble single-walled carbon nanotubes via noncovalent sidewall-functionalization with a pyrene-carrying ammonium ion. *Chemistry Letters* **2002**, *31*, 638-639.

(80) Sun, Y.-P.; Fu, K.; Lin, Y.; Huang, W.: Functionalized carbon nanotubes: properties and applications. *Accounts of Chemical Research* **2002**, *35*, 1096-1104.

(81) Balasubramanian, K.; Burghard, M.: Chemically functionalized carbon nanotubes. *Small* **2005**, *1*, 180-192.

(82) Niyogi, S.; Hamon, M.; Hu, H.; Zhao, B.; Bhowmik, P.; Sen, R.; Itkis, M.; Haddon, R.: Chemistry of single-walled carbon nanotubes. *Accounts of Chemical Research* **2002**, *35*, 1105-1113.

(83) Banerjee, S.; Hemraj-Benny, T.; Wong, S. S.: Covalent surface chemistry of single-walled carbon nanotubes. *Advanced Materials* **2005**, *17*, 17-29.

(84) Liang, F.; Sadana, A. K.; Peera, A.; Chattopadhyay, J.; Gu, Z.; Hauge, R. H.; Billups, W.: A convenient route to functionalized carbon nanotubes. *Nano Letters* **2004**, *4*, 1257-1260.

(85) Mickelson, E.; Chiang, I.; Zimmerman, J.; Boul, P.; Lozano, J.; Liu, J.; Smalley, R.; Hauge, R.; Margrave, J.: Solvation of fluorinated single-wall carbon nanotubes in alcohol solvents. *The Journal of Physical Chemistry B* **1999**, *103*, 4318-4322.

(86) Bahr, J. L.; Tour, J. M.: Highly functionalized carbon nanotubes using in situ generated diazonium compounds. *Chemistry of Materials* **2001**, *13*, 3823-3824.

(87) Macosko, C. W.; Larson, R. G.: Rheology: principles, measurements, and applications. **1994**.

(88) Chen, D. T. N.; Chen, K.; Hough, L. A.; Islam, M. F.; Yodh, A. G.: Rheology of carbon nanotube networks during gelation. *Macromolecules* **2010**, *43*, 2048-2053.

(89) Huang, Y. Y.; Ahir, S. V.; Terentjev, E. M.: Dispersion rheology of carbon nanotubes in a polymer matrix. *Physical Review B* **2006**, *73*, 125422.

(90) Romasanta, L. J.; Lopez-Manchado, M. A.; Verdejo, R.: The role of carbon nanotubes in both physical and chemical liquid–solid transition of polydimethylsiloxane. *European Polymer Journal* **2013**, *49*, 1373-1380.

(91) Khalkhal, F.; Carreau, P. J.; Ausias, G.: Effect of flow history on linear viscoelastic properties and the evolution of the structure of multiwalled carbon nanotube suspensions in an epoxy. *Journal of Rheology* **2011**, *55*, 153-175.

(92) Manley, S.; Davidovitch, B.; Davies, N. R.; Cipelletti, L.; Bailey, A. E.; Christianson, R. J.; Gasser, U.; Prasad, V.; Segre, P. N.; Doherty, M. P.; Sankaran, S.; Jankovsky, A. L.; Shiley, B.; Bowen, J.; Eggers, J.; Kurta, C.; Lorik, T.; Weitz, D. A.: Time-dependent strength of colloidal gels. *Physical Review Letters* **2005**, *95*, 048302.

(93) Moreira, L.; Fulchiron, R.; Seytre, G.; Dubois, P.; Cassagnau, P.: Aggregation of carbon nanotubes in semidilute suspension. *Macromolecules* **2010**, *43*, 1467-1472.

(94) Rahatekar, S. S.; Koziol, K. K.; Kline, S. R.; Hobbie, E. K.; Gilman, J. W.; Windle, A. H.: Length-dependent mechanics of carbon-nanotube networks. *Advanced Materials* **2009**, *21*, 874-878.

(95) Fan, Z.; Advani, S. G.: Rheology of multiwall carbon nanotube suspensions. *Journal of Rheology* **2007**, *51*, 585-604.

(96) Pötschke, P.; Fornes, T. D.; Paul, D. R.: Rheological behavior of multiwalled carbon nanotube/polycarbonate composites. *Polymer* **2002**, *43*, 3247-3255.

(97) White, K. L.; Li, P.; Sumi, Y.; Sue, H.-J.: Rheology of disentangled multiwalled carbon nanotubes dispersed in uncured epoxy fluid. *The Journal of Physical Chemistry B* **2014**, *118*, 362-371.

(98) Menzer, K.; Krause, B.; Boldt, R.; Kretzschmar, B.; Weidisch, R.; Pötschke, P.: Percolation behaviour of multiwalled carbon nanotubes of altered length and primary agglomerate morphology in melt mixed isotactic polypropylene-based composites. *Composites Science and Technology* **2011**, *71*, 1936-1943.

(99) Doi, M.; Edwards, S. F.: *The Theory of Polymer Dynamics*; Oxford university press, 1988; Vol. 73.

(100) Larson, R. G.: *The Structure and Rheology of Complex Fluids*; Oxford University Press New York, 1999; Vol. 150.

(101) Snijkers, F.; Cho, H. Y.; Nese, A.; Matyjaszewski, K.; Pyckhout-Hintzen, W.; Vlassopoulos, D.: Effects of Core Microstructure on Structure and Dynamics of Star Polymer Melts: From Polymeric to Colloidal Response. *Macromolecules* **2014**, *47*, 5347-5356.

(102) Chen, X.; Larson, R. G.: Effect of Branch Point Position on the Linear Rheology of Asymmetric Star Polymers. *Macromolecules* **2008**, *41*, 6871-6872.

(103) Bartholome, C.; Beyou, E.; Bourgeat-Lami, E.; Cassagnau, P.; Chaumont, P.; David, L.; Zydowicz, N.: Viscoelastic properties and morphological characterization of silica/polystyrene nanocomposites synthesized by nitroxide-mediated polymerization. *Polymer* **2005**, *46*, 9965-9973.

(104) Pryamitsyn, V.; Ganesan, V.: Origins of Linear Viscoelastic Behavior of Polymer−Nanoparticle Composites. *Macromolecules* **2006**, *39*, 844-856.

(105) Chatterjee, T.; Krishnamoorti, R.: Dynamic consequences of the fractal network of nanotube-poly(ethylene oxide) nanocomposites. *Physical Review E* **2007**, *75*, 050403.

(106) Khalkhal, F.; Carreau, P. J.: Scaling behavior of the elastic properties of non-dilute MWCNT–epoxy suspensions. *Rheologica Acta* **2011**, *50*, 717-728.

(107) Trappe, V.; Weitz, D. A.: Scaling of the Viscoelasticity of Weakly Attractive Particles. *Physical Review Letters* **2000**, *85*, 449-452.

(108) Filippone, G.; Salzano de Luna, M.: A Unifying Approach for the Linear Viscoelasticity of Polymer Nanocomposites. *Macromolecules* **2012**, *45*, 8853-8860.

(109) Surve, M.; Pryamitsyn, V.; Ganesan, V.: Universality in Structure and Elasticity of Polymer-Nanoparticle Gels. *Physical Review Letters* **2006**, *96*, 177805.

(110) Sahimi, M.; Arbabi, S.: Mechanics of disordered solids. II. Percolation on elastic networks with bond-bending forces. *Physical Review B* **1993**, *47*, 703-712.

(111) Shih, W.-H.; Shih, W. Y.; Kim, S.-I.; Liu, J.; Aksay, I. A.: Scaling behavior of the elastic properties of colloidal gels. *Physical Review A* **1990**, *42*, 4772-4779.

(112) Potanin, A. A.: On the Computer Simulation of the Deformation and Breakup of Colloidal Aggregates in Shear Flow. *Journal of Colloid and Interface Science* **1993**, *157*, 399-410.

(113) Zaske, O. C.; Goodman, S.: Unsaturated Polyester and Vinyl Ester Resins. In *Handbook Of Thermoset Plastics*; Goodman, S. H., Ed.; Noyes Publications: New Jersey 1998.

(114) Paul, D. R.; Barlow, J. W.; Keskkula, H.: In *Encyclopedia of Polymer Science And Engineering*: Wiley, New York, 1986.

(115) Penczek, P.; Czub, P.; Pielichowski, J.: Unsaturated polyester resins: chemistry and technology. In *Crosslinking in Materials Science*; Springer, 2005; pp 1-95.

(116) Forsdyke, K. L.; Starr, T. F. *Thermoset Resins*, Rapra Technology Limited, 2002.

(117) Yang, Y.; Lee, L. J.: Microstructure formation in the cure of unsaturated polyester resins. *Polymer* **1988**, *29*, 1793-1800.

(118) Pascault, J.-P.; Sautereau, H.; Verdu, J.; Williams, R. J. J.: *Thermosetting Polymers*; Marcel Dekker, Inc.: New York, 2002.

(119) Sanchez, E.; Zavaglia, C.; Felisberti, M.: Unsaturated polyester resins: influence of the styrene concentration on the miscibility and mechanical properties. *Polymer* **2000**, *41*, 765-769.

(120) Janković, B.: The kinetic analysis of isothermal curing reaction of an unsaturated polyester resin: Estimation of the density distribution function of the apparent activation energy. *Chemical Engineering Journal* **2010**, *162*, 331-340.

(121) Canamero-Martinez, P.; Fernandez-Garcia, M.; Fuente, J. L. d. l.: Rheological cure characterization of a polyfunctional epoxy acrylic resin. *Reactive and Functional Polymers* **2010**, *70*, 761-766.

(122) Lem, K.-W.; Han, C. D.: Chemorheology of thermosetting resins. II. Effect of particulates on the chemorheology and curing kinetics of unsaturated polyester resin. *Journal of Applied Polymer Science* **1983**, *28*, 3185-3206.

(123) Kamal, M. R.; Sourour, S.: Kinetics and thermal characterization of thermoset cure. *Polymer Engineering & Science* **1973**, *13*, 59-64.

(124) Kenny, J. M.; Trivisano, A.: Isothermal and dynamic reaction kinetics of high performance epoxy matrices. *Polymer Engineering & Science* **1991**, *31*, 1426-1433.

(125) Monti, M.; Puglia, D.; Natali, M.; Torre, L.; Kenny, J. M.: Effect of carbon nanofibers on the cure kinetics of unsaturated polyester resin: Thermal and chemorheological modelling. *Composites Science and Technology* **2011**, *71*, 1507-1516.

(126) Dimier, F.; Sbirrazzuoli, N.; Vergnes, B.; Vincent, M.: Curing kinetics and chemorheological analysis of polyurethane formation. *Polymer Engineering & Science* **2004**, *44*, 518-527.

(127) Chiou, B.-S.; Raghavan, S. R.; Khan, S. A.: Effect of colloidal fillers on the cross-linking of a uv-curable polymer: gel point rheology and the winter−chambon criterion. *Macromolecules* **2001**, *34*, 4526-4533.

(128) Winter, H. H.; Chambon, F.: Analysis of Linear Viscoelasticity of a Crosslinking Polymer at the Gel Point. *Journal of Rheology* **1986**, *30*, 367-382.

(129) White, R. P.: Time-temperature superpositioning of viscosity-time profiles of three high temperature epoxy resins. *Polymer Engineering & Science* **1974**, *14*, 50-57.

(130) Willard, P. E.: Prediction of diallyl phthalate molding performance from laboratory tests II. Comparison of mechanical spectrometer and brabender torque rheometer. *Polymer Engineering & Science* **1974**, *14*, 273-275.

(131) Vilas, J. L.; Laza, J. M.; Garay, M. T.; Rodríguez, M.; León, L. M.: Unsaturated polyester resins cure: kinetic, rheologic, and mechanical-dynamical analysis. I. Cure kinetics by DSC and TSR. *Journal of Applied Polymer Science* **2001**, *79*, 447-457.

(132) Holleman, A. F.; Wiberg, E.; Wiberg, N.: *Inorganic Chemistry*; Academic Press, New York 2001.

(133) Stupak, C. M.; Tuttle Jr, T.; Golden, S.: Optical absorption spectra of solvated electrons in mixtures of ammonia and methylamine. *The Journal of Physical Chemistry* **1984**, *88*, 3804-3810.

(134) Borondics, F.; Bokor, M.; Matus, P.; Tompa, K.; Pekker, S.; Jakab, E.: Reductive functionalization of carbon nanotubes. *Fullerenes, Nanotubes, And Carbon Nanostructures* **2005**, *13*, 375-382.

(135) Stephenson, J. J.; Sadana, A. K.; Higginbotham, A. L.; Tour, J. M.: Highly Functionalized and Soluble Multiwalled Carbon Nanotubes by Reductive Alkylation and Arylation: The Billups Reaction. *Chemistry of Materials* **2006**, *18*.

(136) Kayatin, M. J.: *Chemical Functionalization of Single-walled Carbon Nanotubes for Compatibilization with Unsaturated Polyester Resin*. Auburn University, 2012.

(137) Deng, S.; Brozena, A. H.; Zhang, Y.; Piao, Y.; Wang, Y.: Diameter-dependent, progressive alkylcarboxylation of single-walled carbon nanotubes. *Chemical Communications* **2011**, *47*, 758-760.

(138) Voiry, D.; Roubeau, O.; Pénicaud, A.: Stoichiometric control of single walled carbon nanotubes functionalization. *Journal of Materials Chemistry* **2010**, *20*, 4385-4391.

(139) Birch, A. J.; Hinde, A. L.; Radom, L.: A theoretical approach to the Birch reduction. Structures and stabilities of the radical anions of substituted benzenes. *Journal of the American Chemical Society* **1980**, *102*, 3370-3376.

(140) Buick, A.; Kemp, T. J.; Stone, T. J.: Electron spin resonance spectra of radical anions of styrene and related compounds. *The Journal of Physical Chemistry* **1970**, *74*, 3439-3444.

(141) Chattopadhyay, J.; Chakraborty, S.; Mukherjee, A.; Wang, R.; Engel, P. S.; Billups, W.: SET Mechanism in the Functionalization of Single-Walled Carbon Nanotubes. *The Journal of Physical Chemistry C* **2007**, *111*, 17928-17932.

(142) Lutz, J. F.; Matyjaszewski, K.: Nuclear magnetic resonance monitoring of chain-end functionality in the atom transfer radical polymerization of styrene. *Journal of Polymer Science Part A: Polymer Chemistry* **2005**, *43*, 897-910.

(143) Kayatin, M. J.; Davis, V. A.: In Situ polymerization functionalization of single-walled carbon nanotubes with polystyrene. *Journal of Polymer Science Part A: Polymer Chemistry* **2013**, *51*, 3716-3725.

(144) Jansen, R.; Wallis, P.: Manufacturing, characterization and use of single walled carbon nanotubes. *Material Matters* **2009**, *4*, 23-28.

(145) Nepal, D.; Balasubramanian, S.; Simonian, A. L.; Davis, V. A.: Strong antimicrobial coatings: single-walled carbon nanotubes armored with biopolymers. *Nano Letters* **2008**, *8*, 1896-1901.

(146) Ziegler, K. J.; Rauwald, U.; Gu, Z.; Liang, F.; Billups, W.; Hauge, R. H.; Smalley, R. E.: Statistically accurate length measurements of single-walled carbon nanotubes. *Journal of Nanoscience And Nanotechnology* **2007**, *7*, 2917-2921.

(147) Ureña-Benavides, E. E.; Kayatin, M. J.; Davis, V. A.: Dispersion and rheology of multiwalled carbon nanotubes in unsaturated polyester resin. *Macromolecules* **2013**, *46*, 1642-1650.

(148) Resasco, D.; Alvarez, W.; Pompeo, F.; Balzano, L.; Herrera, J.; Kitiyanan, B.; Borgna, A.: A scalable process for production of single-walled carbon nanotubes (SWNTs) by catalytic disproportionation of CO on a solid catalyst. *Journal of Nanoparticle Research* **2002**, *4*, 131-136.

(149) Chatterjee, T.; Krishnamoorti, R.: Dynamic consequences of the fractal network of nanotube-poly (ethylene oxide) nanocomposites. *Physical Review E* **2007**, *75*, 050403.

(150) Fan, Z.; Advani, S. G.: Rheology of multiwall carbon nanotube suspensions. *Journal of Rheology (1978-present)* **2007**, *51*, 585-604.

(151) Hobbie, E.; Fry, D.: Rheology of concentrated carbon nanotube suspensions. *The Journal of Chemical Physics* **2007**, *126*, 124907.

(152) Khalkhal, F.; Carreau, P. J.: Scaling behavior of the elastic properties of non-dilute MWCNT–epoxy suspensions. *Rheologica Acta* **2011**, *50*, 717-728.

(153) Kharchenko, S. B.; Douglas, J. F.; Obrzut, J.; Grulke, E. A.; Migler, K. B.: Flow-induced properties of nanotube-filled polymer materials. *Nature Materials* **2004**, *3*, 564-568.

(154) Chen, D.; Chen, K.; Hough, L.; Islam, M.; Yodh, A.: Rheology of carbon nanotube networks during gelation. *Macromolecules* **2010**, *43*, 2048-2053.

(155) Trappe, V.; Weitz, D.: Scaling of the viscoelasticity of weakly attractive particles. *Physical Review Letters* **2000**, *85*, 449.

(156) Pogodina, N. V.; Winter, H. H.: Polypropylene crystallization as a physical gelation process. *Macromolecules* **1998**, *31*, 8164-8172.

(157) Romasanta, L.; Lopez-Manchado, M.; Verdejo, R.: The role of carbon nanotubes in both physical and chemical liquid–solid transition of polydimethylsiloxane. *European Polymer Journal* **2013**, *49*, 1373-1380.

(158) Arbabi, S.; Sahimi, M.: Mechanics of disordered solids. I. Percolation on elastic networks with central forces. *Physical Review B* **1993**, *47*, 695.

(159) Du, F.; Scogna, R. C.; Zhou, W.; Brand, S.; Fischer, J. E.; Winey, K. I.: Nanotube networks in polymer nanocomposites: rheology and electrical conductivity. *Macromolecules* **2004**, *37*, 9048-9055.

(160) Prasad, V.; Trappe, V.; Dinsmore, A.; Segre, P.; Cipelletti, L.; Weitz, D.: Rideal Lecture Universal features of the fluid to solid transition for attractive colloidal particles. *Faraday Discussions* **2003**, *123*, 1-12.

(161) Shih, W.-H.; Shih, W. Y.; Kim, S.-I.; Liu, J.; Aksay, I. A.: Scaling behavior of the elastic properties of colloidal gels. *Physical Review A* **1990**, *42*, 4772.

(162) Wu, H.; Morbidelli, M.: A model relating structure of colloidal gels to their elastic properties. *Langmuir* **2001**, *17*, 1030-1036.

(163) Marceau, S.; Dubois, P.; Fulchiron, R.; Cassagnau, P.: Viscoelasticity of Brownian carbon nanotubes in PDMS semidilute regime. *Macromolecules* **2009**, *42*, 1433-1438.

(164) Pryamitsyn, V.; Ganesan, V.: Origins of linear viscoelastic behavior of polymer-nanoparticle composites. *Macromolecules* **2006**, *39*, 844-856.

(165) Hassanabadi, H. M.; Wilhelm, M.; Rodrigue, D.: A rheological criterion to determine the percolation threshold in polymer nano-composites. *Rheologica Acta* **2014**, 1-14.

(166) Mours, M.; Winter, H. H.: Relaxation patterns of nearly critical gels. *Macromolecules* **1996**, *29*, 7221-7229.

(167) Reddy, N. K.; Zhang, Z.; Lettinga, M. P.; Dhont, J. K.; Vermant, J.: Probing structure in colloidal gels of thermoreversible rodlike virus particles: Rheology and scattering. *Journal of Rheology (1978-present)* **2012**, *56*, 1153-1174.

(168) Sarvi, A.; Sundararaj, U.: Electrical permittivity and electrical conductivity of multiwall carbon nanotube-polyaniline (mwcnt-pani) core-shell nanofibers and mwcnt-pani/polystyrene composites. *Macromolecular Materials and Engineering* **2014**, *299*, 1013-1020.

(169) Zhang, Q.; Fang, F.; Zhao, X.; Li, Y.; Zhu, M.; Chen, D.: Use of dynamic rheological behavior to estimate the dispersion of carbon nanotubes in carbon nanotube/polymer composites. *The Journal of Physical Chemistry B* **2008**, *112*, 12606-12611.

(170) Roland, C.; Archer, L.; Mott, P.; Sanchez-Reyes, J.: Determining Rouse relaxation times from the dynamic modulus of entangled polymers. *Journal of Rheology* **2004**, *48*, 395-404.

(171) Raghavan, S. R.; Hou, J.; Baker, G. L.; Khan, S. A.: Colloidal Interactions between Particles with Tethered Nonpolar Chains Dispersed in Polar Media: Direct Correlation between Dynamic Rheology and Interaction Parameters. *Langmuir* **2000**, *16*, 1066-1077.

(172) Ranulfo, A.; Zhenan, B.; Gerald, G. F.: Oriented, polymer-stabilized carbon nanotube films: influence of dispersion rheology. *Nanotechnology* **2013**, *24*, 015709.

(173) Fenoglio, I.; Tomatis, M.; Lison, D.; Muller, J.; Fonseca, A.; Nagy, J. B.; Fubini, B.: Reactivity of carbon nanotubes: Free radical generation or scavenging activity? *Free Radical Biology and Medicine* **2006**, *40*, 1227-1233.

(174) Martínez, A.; Galano, A.: Free radical scavenging activity of ultrashort single-walled carbon nanotubes with different structures through electron transfer reactions. *The Journal of Physical Chemistry C* **2010**, *114*, 8184-8191.

(175) Putz, K. W.; Palmeri, M. J.; Cohn, R. B.; Andrews, R.; Brinson, L. C.: Effect of cross-link density on interphase creation in polymer nanocomposites. *Macromolecules* **2008**, *41*, 6752-6756.

(176) Abdalla, M.; Dean, D.; Robinson, P.; Nyairo, E.: Cure behavior of epoxy/MWCNT nanocomposites: The effect of nanotube surface modification. *Polymer* **2008**, *49*, 3310-3317.

(177) Sui, G.; Zhong, W.; Yang, X.; Yu, Y.: Curing kinetics and mechanical behavior of natural rubber reinforced with pretreated carbon nanotubes. *Materials Science and Engineering: A* **2008**, *485*, 524-531.

(178) Dresselhaus, M. S.; Dresselhaus, G.; Saito, R.; Jorio, A.: Raman spectroscopy of carbon nanotubes. *Physics Reports* **2005**, *409*, 47-99.

(179) Dresselhaus, M. S.; Jorio, A.; Hofmann, M.; Dresselhaus, G.; Saito, R.: Perspectives on carbon nanotubes and graphene raman spectroscopy. *Nano Letters* **2010**, *10*, 751-758.

(180) Zhao, Q.; Wagner, H. D.: Raman spectroscopy of carbon–nanotube–based composites. *Philosophical Transactions of the Royal Society of London A: Mathematical, Physical and Engineering Sciences* **2004**, *362*, 2407-2424.